UNIVERSITY OF OKLAHOMA

GRADUATE COLLEGE

INVESTIGATION OF SPATIAL AND FREQUENCY FILTERING ANTENNA FOR CONGESTED SPECTRAL SENSING

A THESIS

SUBMITTED TO THE GRADUATE FACULTY

in partial fulfillment of the requirements for the

Degree of

MASTER OF SCIENCE

By

MACKENZIE KELSOE
Norman, Oklahoma
2026

Downloaded from SHAREOK. Persistent Handle URL: https://hdl.handle.net/11244/342406

INVESTIGATION OF SPATIAL AND FREQUENCY FILTERING
ANTENNA FOR CONGESTED SPECTRAL SENSING

A THESIS APPROVED FOR THE
SCHOOL OF ELECTRICAL AND COMPUTER ENGINEERING

BY THE COMMITTEE CONSISTING OF

Dr. Jessica Ruyle, Chair

Dr. Hjalti Sigmarsson

Dr. Russell Kenney

© Copyright by MACKENZIE KELSOE 2026

All Rights Reserved.

Acknowledgments

I would like to express my sincerest appreciation to my advisor, Dr. Jessica Ruyle. She first introduced me to the idea of continuing my research to pursue a graduate degree. Without her guidance, I would have never known this was a possibility for me. Since then, Dr. Ruyle has guided me to not only be a better engineer but also to be a much better problem solver in everything I do. Without her mentorship, I would not be half the engineer I am today.

I would like to sincerely thank Dr. Hjalti Sigmarsson for his support and feedback as a member of my thesis committee, and for guiding me through endless fabrication hurdles. Additionally, I would like to thank Dr. Russell Kenney for his help in improving the quality of my thesis through constructive feedback.

It would be remiss not to extend my thanks to Rosalind Agasti, who spent many hours helping me understand filter design and filtenna synthesis. I would like to thank Clayton Blosser, who never hesitated to answer my endless questions as both an undergraduate and graduate researcher, and for his assistance in learning fabrication skills necessary to complete my prototypes. I would like to thank Adrian Bauer for his fabrication assistance and mentorship in conducting anechoic chamber measurements. I would like to extend my sincerest appreciation to our lab manager, Logan, who never failed to drop everything to assist me in the prototype process.

I would like to acknowledge the moral support and companionship of all my friends at the ARRC, including Clayton Blosser, Adrian Bauer, Andrew Eck, William VanHouten, Mariel Avalos, Rosalind Agasti, and Eric Wilson. I would also like to acknowledge my best

friend, Donya Kordestanchi, for supporting me through every challenge.

Finally, I would like to thank my dad, Chance Kelsoe, and my partner, Dax Jones, who stood with me and supported me at every turn on this journey. They were there to offer words of encouragement when things got hard and to celebrate with me through the victories.

Table of Contents

Acknowledgment **iv**

List of Figures **ix**

Abstract **xvii**

1 Introduction **1**

1.1 Motivation 1

1.2 Filtering Horn Antennas 3

1.3 Outline 5

2 Filter Design and Theory **7**

2.1 Coupled Resonator Filter Theory 7

2.2 Input External Coupling 10

2.3 Inter-Resonator Coupling 12

2.4 Output External Coupling 14

2.5 Time Domain Tuning 14

2.5.1 Tuning Resonators 15

2.5.2 Tuning Field Coupling 16

2.5.3 Notes on Time-Domain Tuning 17

2.6 Third Order Chebyshev Filter 18

2.7 Fifth Order Chebyshev Filter 21

2.8 Conclusion 23

3 Horn Design **24**

3.1 Conical Horn with Circular Waveguide 24

3.2 Corrugated Conical Horn with Circular 26

3.3 Pyramidal Horn with Square Waveguide Design 30

3.4 Iris-Fed Horns . . . 32
3.5 Conclusion . . . 41

4 Analyzing Q_{ext} of a horn for matching to filter 42
4.1 Q_{ext} of filter . . . 44
4.2 Extracting Q_{ext} of a Horn Antenna . . . 47
4.3 Matching Methods . . . 47
4.4 Method Comparisons . . . 51
4.5 Varying Horns . . . 60
4.6 Varying Filters . . . 63
4.7 Dual-Polarized Considerations . . . 66
4.8 Tuned Conical Horn Cascaded with the Third-Order Filter . . . 73
4.9 Conclusion . . . 78

5 Coupling Screw Mode Polarizer 80
5.1 45° Coupling Screw as Mode Polarizer . . . 81
5.2 Conclusion . . . 88

6 Fabrication and Measurements 89
6.1 SLA Printing - Dividing Structure . . . 90
6.2 SLA Printing - Printing, Cleaning, and Curing . . . 96
6.3 Electroless Plating . . . 97
6.4 Electroplating . . . 98
6.5 Finishing Structure . . . 103
6.6 Measurements . . . 104
6.7 Prototypes . . . 107
6.7.1 Prototype I . . . 107
6.7.2 Prototype II . . . 110
6.7.3 Prototype III . . . 113
6.7.4 Prototype IV . . . 114
6.8 Conclusion . . . 124

7 Conclusions and Future Work 125
7.1 Conclusion . . . 125
7.2 Scientific Contributions . . . 126

7.3 Future Work 126

List of Figures

1.1 Diagram of (a) a traditional receive system, and (b) a filtering horn receive system 2

2.1 Lowpass prototype for a third-order Chebyshev filter 9
2.2 Example of a third-order bandpass filter circuit diagram 9
2.3 Equivalent circuit for a singly-loaded I/O resonator 11
2.4 Method for the extraction of the Q_{ext} of a singly-terminated cavity resonator from (a) the phase response of the reflection coefficient, and (b) the group delay of the reflection response 12
2.5 Split-pole Technique for extracting coupling between resonators 13
2.6 Example of an ideal third-order Chebyshev filter with 4.14% fractional bandwidth FBW and 0.6 dB IL ripple in the (a)frequency domain, and (b) time domain 15
2.7 Example of the time domain (a) magnitude, and (b) group delay response where the resonator is tuned higher in frequency than ideal 16
2.8 Example of the time-domain (a) magnitude, and (b) group delay response where the resonator is tuned lower in frequency than ideal 17
2.9 Example of the time domain magnitude of a filter where the Q_{ext} is (a) over-coupled, and (b) under-coupled 18
2.10 An image of the third-order cavity-resonator filter 19
2.11 The filter response of the third-order filter 20
2.12 An image of the fifth-order cavity-resonator filter 21
2.13 The filter response of the fifth-order filter 22

3.1 Conical horn antenna fed with circular waveguide shown from an (a) isometric view, and (b) side view 25
3.2 The (a) S-Parameters, and (b) Z-Parameters of a conical horn antenna fed with a circular waveguide, excited by a single polarization 26

3.3 The realized gain of a conical horn antenna fed with a circular waveguide with a single polarization in (a) polar, and (b) Cartesian format with a maximum gain of 14.73 dB at boresight 27
3.4 Diagram of spatial filtering through reduced sidelobes where the yellow radiation pattern demonstrates a traditional horn and the red radiation pattern demonstrates a horn with spatial filtering 28
3.5 Comparison of the electric field distributions for a conical horn antenna compared to a corrugated horn antenna 28
3.6 Corrugated horn antenna fed with circular waveguide shown from an (a) isometric view, and (b) side view 29
3.7 The (a) S-Parameters, and (b) Z-Parameters of a corrugated conical horn antenna fed with a circular waveguide, excited by a single polarization . . . 29
3.8 The realized gain of a corrugated conical horn antenna fed with a circular waveguide with a single polarization in (a) polar plot, and (b) Cartesian format with a maximum gain of 13.23 dB at boresight 30
3.9 Comparison of the normalized realized gain of the conical horn compared to the normalized realized gain of the corrugated horn for sidelobe separation comparison 31
3.10 Pyramidal horn antenna fed with circular waveguide shown from an (a) isometric view, and (b) side view 31
3.11 The (a) S-Parameters, and (b) Z-Parameters of a pyramidal horn antenna fed with a square waveguide, excited by a single polarization 32
3.12 The realized gain of a pyramidal horn antenna fed with a square waveguide with a single polarization in (a) polar plot, and (b) Cartesian format with a maximum gain of 12.62 dB at boresight 33
3.13 Comparison of the realized gain of a dual-polarized waveguide-fed conical horn compared to the realized gain of a dual-polarized iris coupled cavity-fed conical horn for realized gain comparison 33
3.14 The (a) full conical horn fed by an iris coupled cavity, and (b) a close-up of the coaxial feed, cavity, and iris for the conical horn 34
3.15 Return loss of the conical horn fed by the iris-coupled cavity 35
3.16 The realized gain of the conical horn for the x-polarized feed in (a) polar and (b) Cartesian, and for the y-polarized feed in (c) polar and (d) Cartesian, with a maximum boresight gain of 14.57 dB 36

3.17 The (a) full corrugated conical horn fed by an iris coupled cavity, and (b) a close-up of the coaxial feed, cavity, and iris for the corrugated conical horn 37
3.18 Return loss of the corrugated conical horn fed by the iris-coupled cavity . . 37
3.19 The realized gain of the corrugated conical horn for the x-polarized feed in (a) polar and (b) Cartesian, and for the y-polarized feed in (c) polar and (d) Cartesian, with a maximum boresight gain of 13.04 dB 38
3.20 The (a) full pyramidal horn fed by an iris coupled cavity, and (b) a close-up of the coaxial feed, cavity, and iris for the pyramidal horn 39
3.21 Return loss of the pyramidal horn fed by the iris-coupled cavity 39
3.22 The realized gain of the pyramidal horn for the x-polarized feed in (a) polar and (b) cartesian and for the y-polarized feed in (c) polar and (d) Cartesian, with a maximum boresight gain of 12.44 dB 40

4.1 Circuit diagram of a horn acting as a complex load at the output of a third-order cavity resonator filter 43
4.2 Circuit diagram of a slot antenna acting as a resonant structure at the output of a third-order cavity resonator filter 43
4.3 (a) An example of the input impedance behavior expected for a slot antenna acting as a parallel resonator, and (b) the input impedance behavior of the conical horn antenna 43
4.4 The (a) full filter cascaded with the conical horn without a designed iris, and (b) a close-up of the feed between the filter and the conical horn 45
4.5 The (a) frequency-domain filter response, (b) time-domain group delay magnitude, and (c) time-domain magnitude of a dual-polarized, conical horn antenna directly attached to a third-order filter without matching or a specific iris 45
4.6 The (a) full view, and (b) the zoomed view of a conical horn antenna fed by an iris-coupled cavity. 48
4.7 Diagram of the filter Q_{ext} extraction 49
4.8 Group delay of initial coaxial probe feed 51
4.9 Diagram of the coaxial feed Q_{ext} extraction 52
4.10 Example of the mesh of a cavity filter 53

4.11 The (a) group delay magnitude, and (b) the magnitude of the time-domain response for the matching using Method 1.1 of a conical horn antenna to a third-order filter. 54
4.12 The (a) group delay magnitude, and (b) the magnitude of the time-domain response for the matching using Method 1.2 of a conical horn antenna to a third-order filter. 55
4.13 The (a) group delay magnitude, and (b) the magnitude of the time-domain response for the matching using Method 2.1 of a conical horn antenna to a third-order filter. 56
4.14 The (a) group delay magnitude, and (b) the magnitude of the time-domain response for the matching using Method 2.2 of a conical horn antenna to a third-order filter. 56
4.15 The (a) group delay magnitude, and (b) the magnitude of the time-domain response for the matching using Method 3.1 of a conical horn antenna to a third-order filter. 57
4.16 The (a) group delay magnitude, and (b) the magnitude of the time-domain response for the matching using Method 4.1 of a conical horn antenna to a third-order filter. 58
4.17 The (a) group delay magnitude, and (b) the magnitude of the time-domain response for the matching using Method 4.2 of a conical horn antenna to a third-order filter. 58
4.18 The (a) group delay magnitude, and (b) the magnitude of the time-domain response for the matching using Method 5.1 of a conical horn antenna to a third-order filter. 59
4.19 The (a) group delay magnitude, and (b) the magnitude of the time-domain response for the matching using Method 5.2 of a conical horn antenna to a third-order filter. 60
4.20 Final tuned third-order filter response simulated with a solution frequency of 6 GHz and set mesh length 61
4.21 The (a) conical horn coupled to the third-order filter with a cross-slot iris, (b) frequency-domain filter response, (c) time-domain group delay magnitude, and (d) time-domain magnitude of a dual-polarized, conical horn antenna directly attached to a third-order filter using a singly-polarized matching method 62

4.22 The (a) corrugated conical horn attached to the third-order filter with a cross-slot iris, (b) frequency-domain filter response, (c) time-domain group delay magnitude, and (d) time-domain magnitude of a dual-polarized, corrugated, conical horn antenna directly attached to a third-order filter using a singly-polarized matching method 64
4.23 The (a) pyramidal horn attached to the third-order filter with a cross-slot iris, (b) frequency-domain filter response, (c) time-domain group delay magnitude, and (d) time-domain magnitude of a dual-polarized, pyramidal horn antenna directly attached to a third-order filter using a singly-polarized matching method 65
4.24 The (a) conical horn attached to the fifth order filter with a cross-slot iris, (b) frequency-domain filter response, (c) time-domain group delay magnitude, and (d) time-domain magnitude of a dual-polarized, conical horn antenna directly attached to a third order filter using a singly-polarized matching method 67
4.25 The third-order filter (a) image with the ports labeled, and (b) the isolation between ports demonstrated by scattering parameters 68
4.26 The dual-fed (a) single cavity, and (b) cavity-fed iris-coupled horn 68
4.27 The (a) conical horn coupled to the third-order filter with a cross-slot iris, (b) frequency-domain filter response, (c) time-domain group delay magnitude, and (d) time-domain magnitude of a dual-polarized, conical horn antenna directly attached to a third-order filter using a dual-polarized matching method 70
4.28 The (a) corrugated horn coupled to the third-order filter with a cross-slot iris, (b) frequency-domain filter response, (c) time-domain group delay magnitude, and (d) time-domain magnitude of a dual-polarized, corrugated horn antenna directly attached to a third-order filter using a dual-polarized matching method 72
4.29 The (a) pyramidal horn coupled to the third-order filter with a cross-slot iris, (b) frequency-domain filter response, (c) time-domain group delay magnitude, and (d) time-domain magnitude of a dual-polarized, pyramidal horn antenna directly attached to a third-order filter using a dual-polarized matching method 74

4.30 The (a) conical horn coupled to the fifth-order filter with a cross-slot iris, (b) frequency-domain filter response, (c) time-domain group delay magnitude, and (d) time-domain magnitude of a dual-polarized, conical horn antenna directly attached to a fifth-order filter using a dual-polarized matching method 75
4.31 The (a) frequency response, (b) radiation patterns for the x-polarized feed, and (c) radiation patterns for the y-polarized feed are shown 76
4.32 The (a) tuned conical horn directly cascaded with the third-order filter, and (b) transmitted group delay for both x- and y-polarizations 77

5.1 Example of the implementation of modal coupling screws in a dual-mode cavity filter 81
5.2 The (a) top view, and (b) isometric view of the coaxial probe-fed waveguide with a coupling screw inserted at 45° 82
5.3 The (a) isometric view, and (b) side view of the magnetic fields in the coaxial probe-fed waveguide 82
5.4 Plot of phase difference across frequency as coupling screw length varies . 83
5.5 The (a) phase difference, and (b) magnitude of the orthogonal polarizations with a 90° phase difference in a coaxial probe-fed waveguide with a coupling screw inserted at 45° 84
5.6 The (a) phase difference, and (b) magnitude of the orthogonal polarizations with equal magnitudes in a coaxial probe-fed waveguide with a coupling screw inserted at 45° 84
5.7 Wave impedance plot versus frequency normalized by f_0 85
5.8 The (a) horn structure with coupling screw polarizer in square waveguide feed, and (b) the field distribution within the square waveguide feed 86
5.9 The LHCP and RHCP realized gain radiation pattern of an (a) circularly polarized horn antenna, and (b) elliptically polarized horn antenna 87
5.10 The axial ratio of an (a) circularly polarized horn antenna, and (b) elliptically polarized horn antenna 87

6.1 Electroplated horn sections 91
6.2 Electroplated filter half 91
6.3 An image of the cavity feed to a conical horn split straight through one feed 93
6.4 An image of the cavity feed to a conical horn split diagonally 93

6.5 The reflection coefficient of a cavity-fed horn with the cavity split (a) straight through one polarization, and (b) diagonally 94
6.6 Reflection coefficient for different flange gap sizes is plotted 95
6.7 Reflection coefficient for different flange gasket materials is shown and compared to the filter without a flange gap 95
6.8 Reflection coefficient for different surface roughnesses is shown 96
6.9 An image of the roughness of an SLA print before wet-sanding 97
6.10 An image of the electroless plating bath used to deposit the copper seed layer 99
6.11 An example image of a piece following the electroless plating process . . . 99
6.12 An example image of delamination of copper during the electroless plating process 100
6.13 An image of the electroplating rack and tank 101
6.14 Example images of the (a) outside of a resin print, and (b) inside of the piece after the first electroplating cycle 101
6.15 Example images of the silver paint application (a) using an airbrush, and (b) a paintbrush 102
6.16 Example images of the even copper plating after the final plating stage on (a) a quarter of the conical horn, and (b) half of the filter 102
6.17 An image of the coaxial probe inserted into half of the cavity structure . . . 104
6.18 An image of the application of conductive epoxy around the flange 105
6.19 An image of the two halves of the filter Prototype II bolted together using M2 pan head bolts, washers, and nuts 105
6.20 An image of the filter bolted to the conical horn 106
6.21 An image of the HUT mounted on the anechoic chamber pedestal 107
6.22 An image of the first filter prototype with the copper tape covered crack visible 108
6.23 Filter response of Prototype I 109
6.24 Simulated filter response with probe length shortened from tuned filter probe length 109
6.25 Image of the feed of the second prototype with (a) holes drilled for the bolts, and (b) the connector attached 110
6.26 An image of the gap in the flange due to print warping that has been filled with conductive epoxy 111
6.27 Measured frequency filter response for Prototype II compared to simulated . 112

6.28 Measured radiation patterns for Prototype II compared to simulated at 3.625 GHz for the (a) x-polarized, and (b) y-polarized feed 112
6.29 An image of the feed for Prototype III 113
6.30 Measured frequency filter response for Prototype III compared to simulated 115
6.31 Measured radiation patterns for Prototype III compared to simulated at 3.625 GHz for the (a) x-polarized, and (b) y-polarized feed 115
6.32 An image of the feed for Prototype IV 116
6.33 Measured frequency filter response for Prototype IV without conductive epoxy compared to simulated 117
6.34 The (a) group delay, and (b) magnitude of the time-domain response for Prototype IV without conductive epoxy compared to simulated 117
6.35 Measured radiation patterns for Prototype IV without conductive epoxy compared to simulated at 3.625 for the (a) x-polarized, and (b) y-polarized feed 118
6.36 Measured frequency filter response for Prototype IV with conductive epoxy compared to simulated 119
6.37 Measured radiation patterns for Prototype IV with conductive epoxy compared to simulated at 3.625 GHz for the (a) x-polarized vertically oriented, (b) x-polarized horizontally oriented, (c) y-polarized vertically oriented, and (d) y-polarized horizontally oriented 120
6.38 Measured radiation patterns for Prototype IV with conductive epoxy compared to simulated at 3.56 GHz with the (a) x-polarized vertically oriented, (b) x-polarized horizontally oriented, (c) y-polarized vertically oriented, and (d) y-polarized horizontally oriented 121
6.39 Measured radiation patterns for Prototype IV with conductive epoxy compared to simulated at 3.68 GHz with the (a) x-polarized vertically oriented, (b) x-polarized horizontally oriented, (c) y-polarized vertically oriented, and (d) y-polarized horizontally oriented 123

Abstract

A cascaded spatial-and-frequency-filtering horn antenna is designed to increase sensitivity for detecting small signals in a congested spectrum environment. Spatial filtering is performed using a corrugated conical horn antenna to achieve 39 dB of separation between the main beam and the peak sidelobe, and to obtain a circularly symmetric radiation pattern. Frequency filtering is accomplished by directly cascading the corrugated conical horn antenna with a bandpass cavity resonator filter. A design method for cascading horn antennas with cavity resonator filters is proposed and validated by matching a conical, corrugated, and pyramidal horn to a third-order cavity filter and also by matching a conical horn antenna to a fifth-order cavity filter. The design method eliminates the need for lengthy optometric tuning using a full-wave electromagnetic (EM) simulator. The conical horn coupled to the third-order filter is then fabricated using stereolithography (SLA) additive manufacturing and copper-plated. Measurements of the frequency filtering response and the radiation pattern of the conical filtering horn antenna are conducted in an anechoic chamber.

Chapter 1

Introduction

1.1 Motivation

Freeing up mid-band spectrum resources allows 5G operators to harness desirable frequencies. However, there are also high-priority incumbents that need to be reliably detected, such as naval-born radar signals along the coastline. Environmental sensing capability (ESC) sensors are used to detect signals transmitted by the naval-borne radar and to send a signal to surrounding transmitters operating in the CBRS band to cease transmission [1]. Current ESC sensors limit the transmission power of 5G operators in the Citizens Broadband Radio Service (CBRS) band [2] because they have to detect small signals within strong interference. Improving the sensitivity of these sensors through machine learning and proactive receiver antenna design will enable 5G operators to transmit at higher power without interfering with the reception of higher-priority signals [3]. This project focuses on the design of a receiver antenna that spatially and frequency filters to reduce interference with the reception of high-priority signals. This is accomplished by directly cascading a filter with a horn antenna to reduce loss in the receive chain and implementing corrugations in the horn antenna to reduce the sidelobes of the receive horn. By reducing sidelobes, the beam shape can be designed to generate positional nulls in gain at the locations of 5G towers [3].

Filters are necessary after the antenna in the receive (RX) chain for ESC sensors to detect

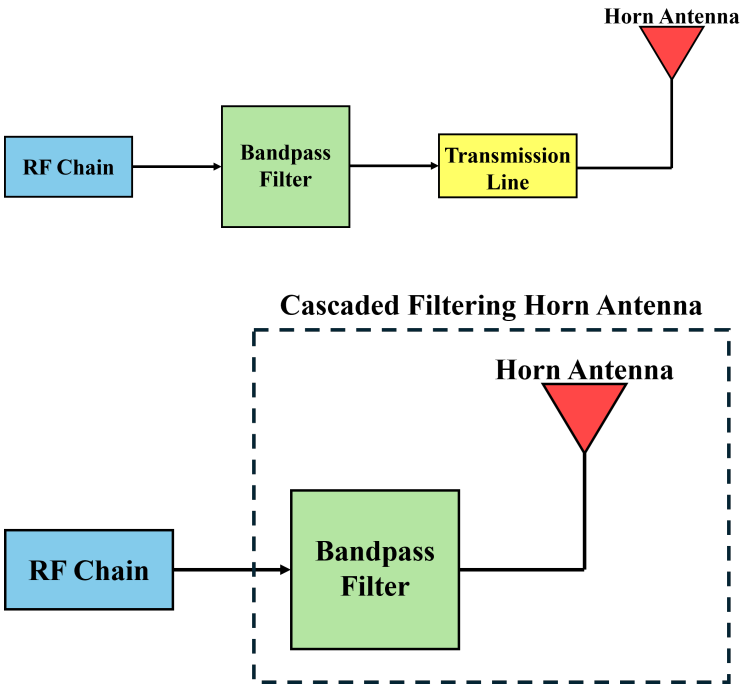

Figure 1.1: Diagram of (a) a traditional receive system, and (b) a filtering horn receive system

small-signal, high-priority incumbents and to attenuate high-power telecommunication signals transmitting in neighboring frequency bands. In traditional receiving systems, the filter is connected to the antenna via a transmission line, often a coaxial cable or a waveguide section [4]. However, this transmission line at the front of the receive chain reduces sensitivity by introducing loss and noise into the system [4]. By cascading the filter directly with the antenna or by designing the filter and antenna as a single unit, as shown in Fig. 1.1, these losses can be mitigated.

The work documented in this thesis introduces a matching method for the design of directly cascaded filtering horn antennas, eliminating the need for extensive parametric tuning of the filter/horn. For this cascaded filter/horn, the horn is not providing a filtering pole because the horn antenna operates with a wider bandwidth than the filter bandwidth and therefore does not contribute a resonance in the filter passband [5]. This will be covered in more detail in Chapter 4.

1.2 Filtering Horn Antennas

In order to design an iris-fed filtering horn, it is necessary to take into account the complex load presented by the iris and the horn. Typically, a filter is connected to a system impedance of 50Ω. However, the input impedances of the horn antennas investigated in this thesis, plotted in Chapter 3, are much higher than that. The filter then has an asymmetrically loaded structure with a 50Ω impedance feed and a different complex load.

Filtering horn antennas have been implemented in a number of ways in the literature. In [6], a nested horn antenna is directly cascaded with a fourth-order dual-mode spherical filter network for Ka-band and a filtering divider network for K-band. It was printed using stereolithography (SLA) additive manufacturing and copper-plated for precision and low cost. The author does not specify how the antennas were matched to the filters.

In [7], [8], and [9], metal posts were inserted within the horn taper to define cavities acting as resonators for the filter and all three filtering horn antennas were designed using optimization of the post-resonators in an electromagnetic software, which can be lengthy and computationally expensive. In [10], a horn was designed that utilizes filtering notches within the taper of a pyramidal horn antenna to achieve a filtering function without changing the radiation characteristics of the horn. Although the author of [10] uses an iris to define the Q_{ext} between the last cavity of the filter and the final taper to free space, no method for matching this value to the Q_{ext} of the filter was established. A horn similar to that in [10] was presented in [11]; however, the horn was a circularly polarized filtering conical horn antenna. The author of [12] first designed the filter, then flared the cavities and re-adjusted the couplings through tuning using space-mapping. Space mapping is a technique that reduces the computational load of EM optimization, but it does not eliminate the computational cost entirely [13].

Another common method for introducing a filtering response within the horn flare is

to insert a split-ring resonator between the waveguide feed and the horn flare. The authors of [14] utilized a dielectric slab with omega-shaped traces (omega particles) to achieve a narrow-band filtering response. Both papers [15] and [16] introduced split ring resonators in a horn feed to achieve a notch bandstop filter response. The authors of [15] demonstrated that two split ring resonators in the feed can be used to achieve a dual-band notched bandstop filter, while in [16] an electrically small split ring resonator was utilized. The authors of [17] used an electrically small cross slot resonator on a metallic screen to achieve circular polarization with a narrowband bandpass filter design. Frequency selective surfaces have also been implemented in both substrate integrated waveguide (SIW) and traditional horn antennas to create filtering horn antennas [18] [19] [20]. However, these methods do not allow for implementing specific filtering responses, such as Chebyshev responses, because they rely on inducing nulls at specific frequencies. This gives the designer no control over the filter's passband and stopband specifications.

Filtering horn antennas can also be implemented through the use of a gap waveguide structure as presented in [21] [22] [23], allowing for a fully metallic structure. More commonly, filtering horn antennas are designed in SIW to allow for flat layouts. These vary from gap waveguide structures in that a dielectric material is used within the via cavities. A variety of SIW filters cascaded with horns have been designed [24] [25] [26]. The author of [24] designed a horn cascaded directly from a trapezoidal cavity using slow-wave metal post loading to reduce H-plane sidelobe levels and matching stripes at the aperture of the horn. The authors of [25] presented a non-reciprocal SIW filtering horn using time-modulated capacitors. There have also been SIW filtering horn antennas designed with the filtering cavities applied within the taper of the SIW horn [27] [28] [29] [30] [12]. However, these quasi-planar structures of the gap waveguide and substrate integrated waveguides do not lend themselves to the design of dual-polarized horn antennas.

The filtering horns described above largely rely on optimization in electromagnetic

solvers such as Ansys HFSS to tune the filter after cascading the horn with the filter. The author of [29] introduced a design method focused on the design of an SIW filtering horn structure designed based on coupling matrices, but no detail is given as to how the coupling matrix is used to derive the physical parameters of the structure. To the best of the knowledge of this author, there has not been an in-depth procedure for extracting Q_{ext} of a dual-polarized horn antenna for matching to cavity filters. Filtenna design methods have been introduced for other antenna types that focus on the extraction of the Q_{ext} of the antenna to match the Q_{ext} needed for filter performance based on extracting the lossless radiation quality factor Q_{rad} from the structure using Z-parameters [31] [32] or by analyzing the radiator as an RLC resonator structure [33]. The authors of [34], [35], and [32] used Q_{rad} to match slot antennas to filters. However, these methods share the common feature of being designed to operate as resonant structures. Horn antennas do not exhibit resonant behavior at their operating frequency and are typically designed to maintain reactances near zero. Instead, they operate as a complex load at the filter's output port, which will be discussed in detail in Chapter 4.

1.3 Outline

This work demonstrates a design method for a dual-channel, equi-ripple Chebyshev cavity filter co-designed to be directly cascaded with a corrugated horn antenna, requiring minimal tuning.

In Chapter 2, the design theory of cavity resonator filters is discussed. The conventional filter synthesis techniques are then applied to the design of a third and fifth-order Chebyshev filters. Time-domain tuning will be discussed and applied to tune the filters designed in this work with ease.

Horn antenna design will be discussed in Chapter 3. The design of traditional conical,

corrugated conical, and pyramidal horn antennas will be discussed. Spatial filtering is established through the application of corrugations to a conical horn antenna. An iris-coupled cavity feed will then be developed and applied to feed the three horns to facilitate control of the Q_{ext} presented by the horn. Performance will be analyzed for all three horns for both feed types.

In Chapter 4, a method for calculating Q_{ext} is derived from the group delay of the iris-coupled horn antenna. Various permutations of this method are investigated and compared. The best method is then applied to match a conical, a corrugated conical, and a pyramidal horn to a third-order Chebyshev filter. Performance of the methods is analyzed in both the time and frequency domains. The proposed matching method is then tested by matching the conical horn to the fifth-order Chebyshev filter.

Chapter 5 details a brief investigation into the use of modal coupling screws to generate and radiate circular polarization from a horn fed by a cavity filter that is excited by a single coaxial probe feed.

Chapter 6 describes the fabrication and measurement process for the conical horn cascaded with the third-order filter. The structure is printed in sections using stereolithography (SLA) additive manufacturing, copper-plated, and measured in an anechoic chamber to analyze the filtering response and the radiation pattern.

Chapter 7 provides a brief summary of the completed thesis work and its scientific impact. Future work is proposed to improve the method for matching Q_{ext} between the horn and the filter.

Chapter 2

Filter Design and Theory

This chapter will cover the design of two coupled resonator filters using classic filter synthesis techniques. The time-domain tuning method is also presented to facilitate tuning of the final filter. These techniques will then be applied to the design of third- and fifth-order Chebyshev filters. Chebyshev filters were chosen as they give a high attenuation near-band at the expense of ripple in the passband [36].

2.1 Coupled Resonator Filter Theory

The initial step in the filter design method introduced in this work is the generation of a low-pass prototype ladder network [37, 36, 38]. An example of the third-order lowpass filter prototype is shown in Fig. 2.1. This consists of ideal inductors and capacitors, with their conductances determined by the g-coefficients for the specific filter type. An nth-order filter will have $n+1$ g-coefficients. The g-coefficients of Chebyshev filters are [39],

$$g_0 = 1, \tag{2.1}$$

$$g_1 = \frac{2}{\eta}\sin\frac{\pi}{2n}, \tag{2.2}$$

$$g_{r+1} = \frac{4\sin\frac{(2r-1)\pi}{2n}\sin\frac{(2r+1)\pi}{2n}}{g_r(\eta^2+\sin^2\frac{r\pi}{n})} \text{for } r = 1, 2, ..., n-1, \tag{2.3}$$

and

$$g_{n+1} = \begin{cases} 1 & \text{for } n \text{ odd} \\ \epsilon + \sqrt{1+\epsilon^2} & \text{for } n \text{ even and } S_{11}(0) \geq 0 \\ \frac{1}{\epsilon+\sqrt{1+\epsilon^2}} & \text{for } n \text{ even and } S_{11}(0) \leq 0 \end{cases} \tag{2.4}$$

where η is defined as

$$\eta = \sinh \frac{1}{n} \sinh^{-1} \frac{1}{\epsilon} \tag{2.5}$$

and the ripple factor, ϵ can be defined by passband ripple L_A or return loss ripple L_R in decibels (dB) as

$$\epsilon = \sqrt{10^{\frac{L_A}{10}} - 1} \tag{2.6}$$

or

$$\epsilon = \frac{1}{\sqrt{10^{\frac{L_R}{10}} - 1}}. \tag{2.7}$$

The ripple factor is not related to permittivity ϵ_r and ϵ_0.

The g-coefficients represent the conductances for the low-pass prototype with a cutoff frequency of 1 rad/s and an input impedance of 1 Ω. These values can then be scaled to low-pass, high-pass, band-pass, and bandstop filters with different cutoff frequencies, fractional bandwidths, and system impedance. The filters being designed for this work are band-pass filters operating in the CBRS band of 3.55-3.7 GHz. The circuit diagram for this bandpass filter is demonstrated in Fig. 2.2. Scaling factors can give specific resistances, capacitances, and inductances, which is great for approximating planar or lumped element components, where it is relatively easy to achieve specific reactances. However, it is much more challenging to match specific reactances using cavities and three-dimensional coupling mechanisms.

Dishal [38] proposed a method for the synthesis of direct-coupled resonator filters with mainline coupling that relates g-coefficients directly to coupling mechanics. In this method,

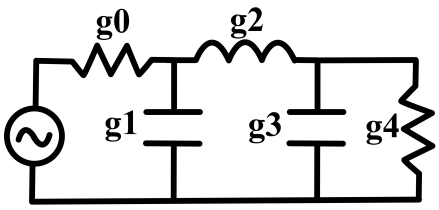

Figure 2.1: Lowpass prototype for a third-order Chebyshev filter

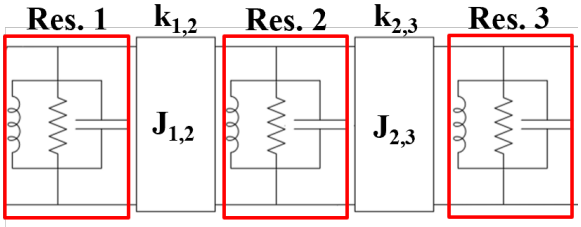

Figure 2.2: Example of a third-order bandpass filter circuit diagram

the factors for consideration are the resonant frequency, f_0, of each resonator, the coupling between the input port and the first cavity Q_{ext1}, the inter-resonator coupling between each of the resonators $k_{i,j}$, and the coupling between the output port and the final cavity Q_{ext2}. The filter is then analyzed as a series of resonators and coupling elements. These coupling quantities can be calculated directly from the g-coefficients as [37, 38, 40]

$$Q_{ext1} = \frac{g_0 g_1}{\Delta}, Q_{ext2} = \frac{g_N g_{(N+1)}}{\Delta}, k_{i,i+1} = \frac{\Delta}{\sqrt{g_i g_{i+1}}} \text{ for } i = 1 \text{ to } (N-1). \tag{2.8}$$

The coupling values can be related to the physical structures of cavity filters, enabling the design of non-planar filters. Using full-wave electromagnetic (EM) solvers, cavities and irises can be reasonably matched. This process will be detailed in the following sections.

2.2 Input External Coupling

The external quality factor, Q_{ext1}, of the input port of the first resonator is extracted using a singly-terminated resonator [41]. Q_{ext1} can be found from the phase response of the reflection coefficient or the group delay. To extract only the effects of the input port, it is important to simulate only the first cavity or ensure that the following cavities are shorted.

An equivalent circuit for a singly-loaded input/output (I/O) resonator can be seen in Fig. 2.3, where G is the external conductance attached to the lossless LC resonator [41]. The reflection coefficient (S11) at the excitation port of the resonator is

$$S_{11} = \frac{G - Y_{in}}{G + Y_{in}} = \frac{1 - Y_{in}/G}{1 + Y_{in}/G} \tag{2.9}$$

where Y_{in} is the input admittance of the resonator equal to

$$Y_{in} = j\omega C + \frac{1}{j\omega L} = j\omega_0 C(\frac{\omega}{\omega_0} - \frac{\omega_0}{\omega}) \tag{2.10}$$

and $\omega_0 = 1/\sqrt{LC}$ is the resonant frequency. In the vicinity of resonance, $\omega = \omega_0 + \Delta\omega$, Y_{in} can be simplified to

$$Y_{in} = j\omega_0 C \cdot \frac{2\Delta\omega}{\omega_0}. \tag{2.11}$$

By substituting Y_{in} and noting $Q_{ext} = \omega_0 C/G$, $S11$ becomes

$$S_{11} = \frac{1 - jQ_{ext} \cdot (2\Delta\omega/\omega_0)}{1 + jQ_{ext} \cdot (2\Delta\omega/\omega_0)}. \tag{2.12}$$

Under the assumption that the resonator is lossless, the magnitude of S_{11} is always equal to one because in the vicinity of resonance, the parallel resonator shown in Fig. 2.3 behaves like an open circuit [41]. The phase response of S_{11}, however, changes with frequency.

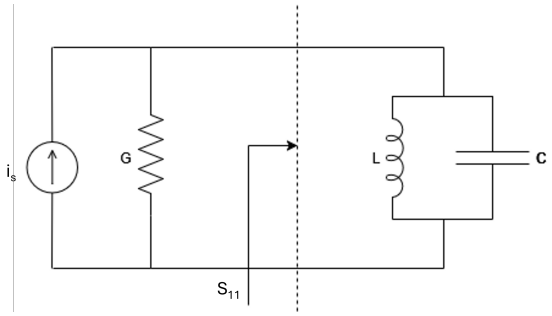

Figure 2.3: Equivalent circuit for a singly-loaded I/O resonator

When the phase is $\pm 90°$, the corresponding value of $\Delta\omega$ is

$$2Q_{ext}\frac{\Delta\omega\mp}{\omega_0} = \mp 1 \tag{2.13}$$

Therefore, the absolute bandwidth between the $\pm 90°$ points is $\Delta\omega_{\pm 90°} = \frac{\omega_0}{Q_{ext}}$. The external quality factor Q_{ext} can then be extracted as [41]

$$Q_{ext} = \frac{\omega_0}{\Delta\omega_{\pm 90°}} \tag{2.14}$$

where $\Delta\omega_{\pm 90°}$ is the difference in frequency between the $\pm 90°$ points ω_- and ω_+ shown in Fig. 2.4a.

Alternatively, Q_{ext1} can be extracted from simulation using the peak group delay of the reflection coefficient [41] because the group delay is the derivative of the phase of S_{11}. Therefore, the group delay peak magnitude represents the slope of the phase response at f_0. The peak can be seen in Fig. 2.4b. The relation is given by

$$Q_{ext1} = \frac{2\pi f_0 \tau_{S_{11}}(f_0)}{4}. \tag{2.15}$$

It is important to note that both methods rely on the group delay or $\pm 90°$ phase shift to be centered at the center frequency, f_0. The reference plane of the EM simulation may

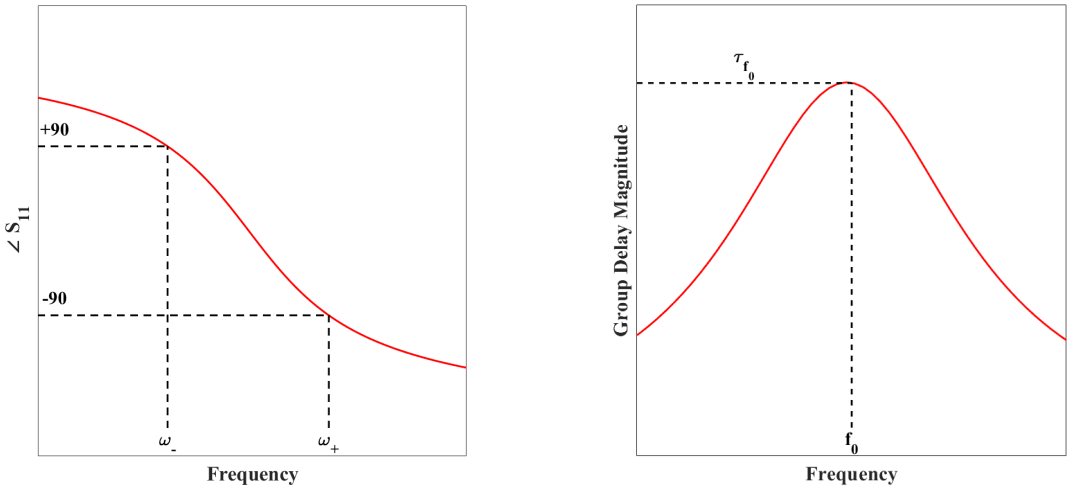

(a) **(b)**

Figure 2.4: Method for the extraction of the Q_{ext} of a singly-terminated cavity resonator from (a) the phase response of the reflection coefficient, and (b) the group delay of the reflection response

not always match that of the equivalent circuit in Fig. 2.3, which introduces an extra phase shift such that the phase of the simulated $S11$ does not equal zero at resonance [41]. In a traditional waveport simulation, this shift could be accounted for by de-embedding the simulation to center the response at resonance [33]. In the case of a coaxial probe, de-embedding is not possible because the waveport excitation is placed at the start of the probe, outside the cavity, to simulate the coaxial probe being fed through a transmission line. In this case, the cavity size is adjusted to keep the group delay centered at resonance.

2.3 Inter-Resonator Coupling

The coupling coefficient, k, is defined as the ratio of coupled to stored energy [37] [41]. The coupling coefficient is difficult to compute in closed form; however, EM solvers enable extraction of the coupling coefficient for specific geometries without lengthy calculations [41]. One commonly used method for extracting the inter-resonator coupling is the split-pole technique [37] [40] [41]. This technique consists of simulating two cavities coupled together

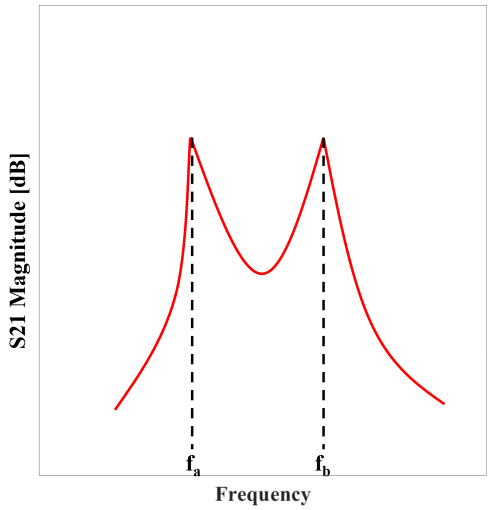

Figure 2.5: Split-pole Technique for extracting coupling between resonators

via the desired coupling mechanism, weakly coupled to the excitation source at both input and output ports. The splitting of the poles of the two resonators can then be seen in the transmission coefficient between the input and output ports, as demonstrated in Fig. 2.5. The expression for determining the coupling coefficient based on the frequencies, f_a and f_b, of the split peaks is given as [41],

$$k = \frac{f_b^2 - f_a^2}{f_b^2 + f_a^2}. \tag{2.16}$$

This method relies on the resonators to be lossless or to have relatively high unloaded quality factors (Q) to be able to observe the steep peaks of the natural resonant frequencies of the coupled cavities in the transmission response [37]. It is also necessary that the excitation structure is weakly coupled to be able to see the two distinct peaks in the S_{21} response.

2.4 Output External Coupling

A typical filter structure would be connected to lengths of transmission line exhibiting matching load impedances at either end, and the output external coupling is calculated using the same method as used for the input external coupling. This would typically be a 50Ω line, but does not have to be. Some filters are symmetric, meaning they have the same input and output coupling values.

In the case of a direct cascaded filter/antenna, the output port is not the same as the input port. The output port is replaced with an antenna. This necessitates a method to match the antenna to the filter's Q_{ext}. This has been done in a couple of ways for resonant antennas, as discussed in Chapter 1. However, the horn antenna discussed in this work does not have its own resonance. Therefore, a method is needed to determine and match the Q_{rad} of a horn antenna to the Q_{ext} expected by the filter. This work will present such a method, which will be detailed in Chapter 4.

2.5 Time Domain Tuning

The design method detailed above gives a starting point for meeting the filter specifications the designer needs, but it will not be exact because the couplings are all analyzed independently of each other, while in the full structure, each coupling will have a loading effect on the resonant frequencies of the cavities and the other couplings. The designer will need to fine-tune the filter to get the exact response needed. This can be a lengthy process to accomplish with frequency domain tuning alone, as it is hard to determine exactly which part of the overall filter needs adjustment. It leads to a process consisting largely of intuition. Joel Phillip Dunsmore proposed a method to analyze the filter response in the time domain to enable more efficient tuning [42]. By taking a windowed inverse Fourier transform of the filter's reflection response, it is possible to analyze the couplings and resonant frequencies

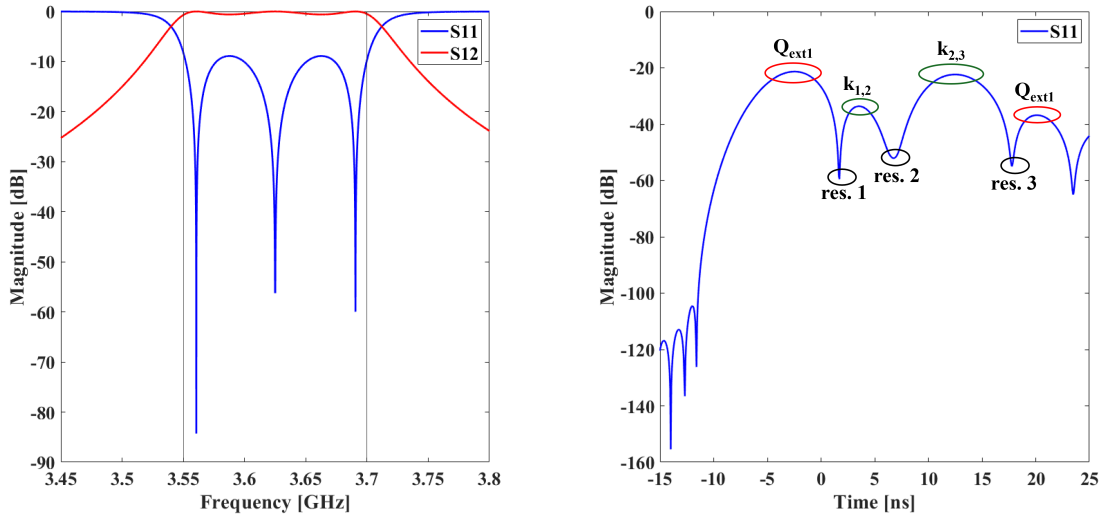

(a) **(b)**

Figure 2.6: Example of an ideal third-order Chebyshev filter with 4.14% fractional bandwidth FBW and 0.6 dB IL ripple in the (a)frequency domain, and (b) time domain

individually and consecutively. The humps in the magnitude of the reflection coefficient in the time domain represent the electromagnetic field interactions between the input and output ports and between the resonators, while each null corresponds to a resonance as illustrated in Fig. 2.6b [37]. In the frequency domain, it cannot be ascertained exactly which poles correspond to which couplings and which resonances. However, in the time domain, the couplings and resonances are represented consecutively. The ideal frequency response of the filter can be seen in Fig. 2.6a. The following sections detail how to use this method to tune a filter by comparing the ideal filter's time-domain response with that of the filter being tuned. This work does not detail the mathematical derivation of the method, which can be found in [42].

2.5.1 Tuning Resonators

The nulls in the time-domain response indicate the resonators' frequency tuning. A higher null depth indicates a better-tuned resonator. However, magnitude null depth does not

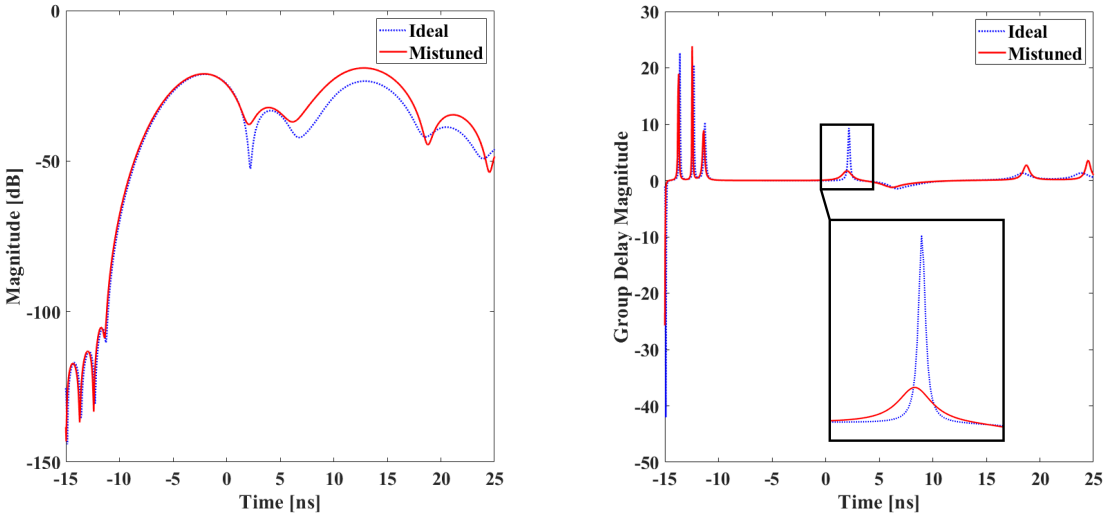

(a) **(b)**

Figure 2.7: Example of the time domain (a) magnitude, and (b) group delay response where the resonator is tuned higher in frequency than ideal

indicate whether the resonator is too high or too low in frequency. To obtain this information, it is necessary to examine the time-domain group-delay response. The ideal group delay response is plotted along with the group delay of the filter being tuned. The sharp peaks of the ideal response indicate well-tuned resonators. The size and location of the mistuned resonator peak relative to the ideal provide insight into the necessary tuning. If the peak of the mistuned cavity is lower than ideal and lies in the positive half of the group delay response, shown in Fig. 2.7, then the resonator is tuned to a higher frequency. When the mistuned resonator is lower in frequency, shown in Fig. 2.8, then the peak is negative, and the magnitude is lower than ideal [37].

2.5.2 Tuning Field Coupling

The field couplings are tuned in the time domain using the magnitude and null shift of the humps. The humps are consecutive, beginning with the input external coupling, followed by the cavity-to-cavity couplings, and then the output external coupling. If the null is shifted

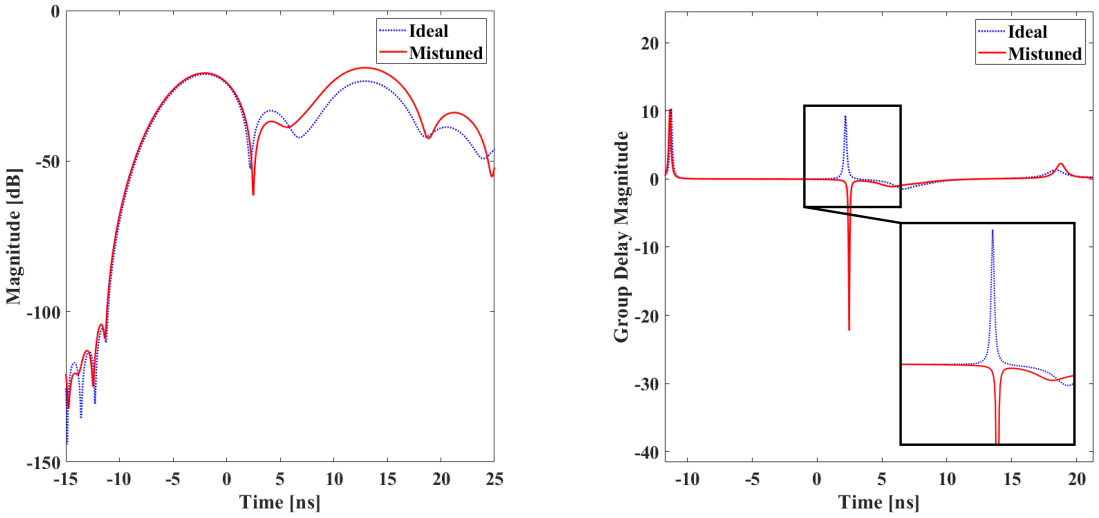

(a) **(b)**

Figure 2.8: Example of the time-domain (a) magnitude, and (b) group delay response where the resonator is tuned lower in frequency than ideal

forward and the hump overshoots the ideal response, the external coupling is too low and needs to be increased. If the null is shifted behind the ideal and the hump is lower than the ideal, then the coupling is too high and needs to be decreased [37]. Examples of this are shown in Fig. 2.9. This applies to both the external and internal coupling.

2.5.3 Notes on Time-Domain Tuning

Time-Domain tuning is a powerful tool for the tuning of resonator-based filters. The best practice is to tune consecutively, starting with the first external coupling and proceeding cavity by cavity, because the effects of mistuned irises and cavities following the resonance being tuned are small, whereas mistuned elements occurring before the resonance being tuned are not. That said, due to the slight loading effects as a resonator is tuned, it is often necessary to slightly retune the preceding resonator. Some success can also be found by focusing on tuning the resonances to maximize the depth of the nulls before tuning the couplings, especially when the time domain response is hard to read. When the resonances

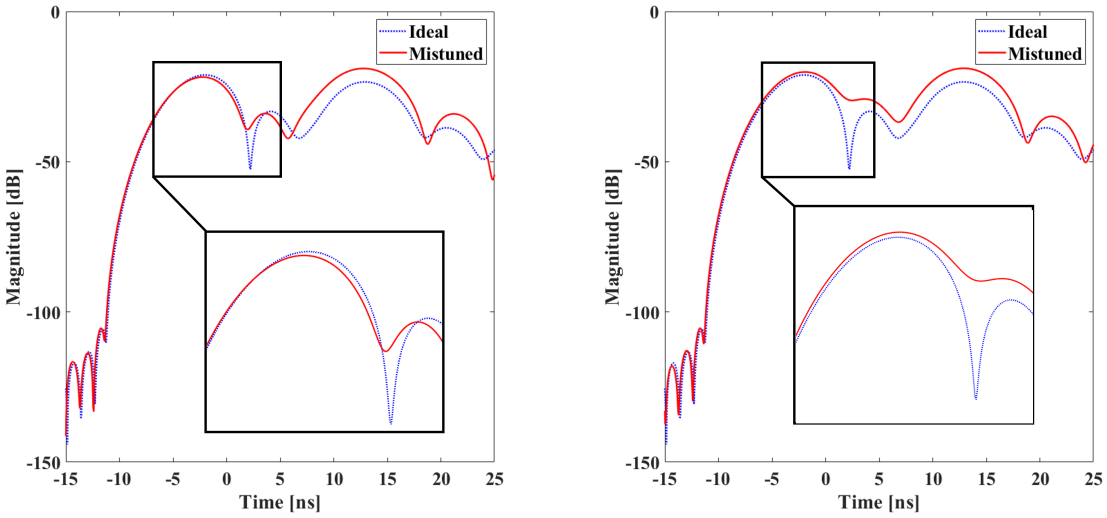

(a) **(b)**

Figure 2.9: Example of the time domain magnitude of a filter where the Q_{ext} is (a) over-coupled, and (b) under-coupled

are too far from the required center frequency, the nulls can disappear altogether, making tuning challenging.

Another important note is in the setting of the time window for the IDFT. The center frequency of the sweep must match the filter's center frequency. It is also important that the frequency sweep is sufficiently large to distinguish between filter sections, but if it is too large, tuning sensitivity is reduced. A good rule of thumb for the frequency sweep is to set it to 2 to 5 times the filter's bandwidth, BW. Finally, the start time should be set to $t = -(2/\pi BW)$, corresponding to the delay of one resonator and the stop time should be about 2 to 3 times the total filter delay, approximately $t = (2N + 1)/(\pi BW)$ where N is the number of resonators.

2.6 Third Order Chebyshev Filter

For this work, a third-order Chebyshev filter with a 0.6 dB insertion-loss ripple and a fractional bandwidth (FBW) of 4.14% was designed. These specifications were chosen to

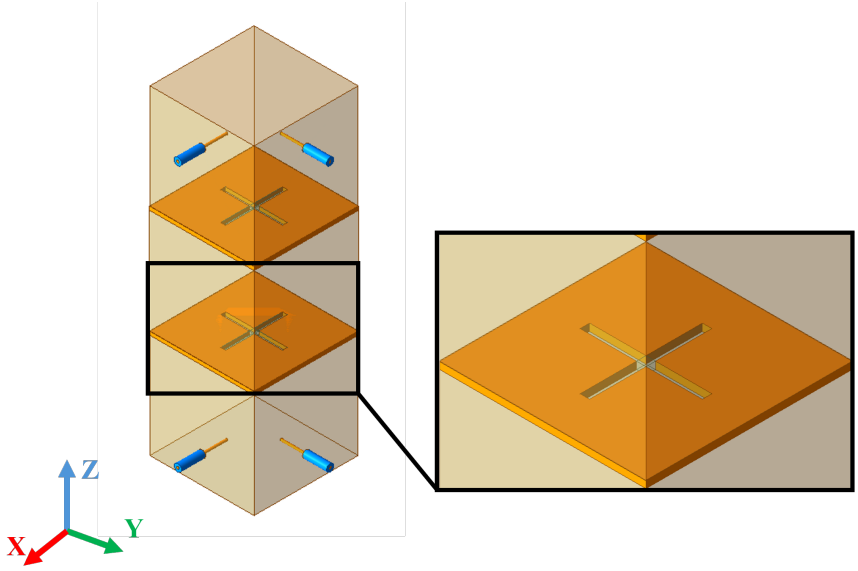

Figure 2.10: An image of the third-order cavity-resonator filter

balance a low passband ripple with strong out-of-band rejection. When the filter order is kept consistent, out-of-band rejection decreased as the filter ripple decreased. The fractional bandwidth encompasses the entire CBRS band. It was initially designed as a simple cavity resonator filter without accounting for the final cascaded-filtering antenna design, since the goal is to match the finished horn antenna to the finished filter with minimal post-cascade tuning. The filter was designed with cubic cavities to support dual-mode operation and cross slots to facilitate magnetic coupling in both x- and y-polarizations. The third-order filter structure can be seen in Fig. 2.10. Due to the symmetry of the cubic cavities and cross-slot magnetic coupling, the modes give identical filter responses with low cross-polarization coupling. The first and last cavities were fed using a dual-coaxial probe setup. It was desired to set the coaxial probe length so that Amphenol 132147 candlestick connector probes can be used without significant modification. The tuned filter response can be seen in Fig. 2.11. An average insertion loss ripple of 0.6 dB was achieved with a fractional bandwidth of 3.78%. The filter demonstrated 30 dB of attenuation at 3.45 GHz and 15 dB attenuation was seen at 3.8 GHz.

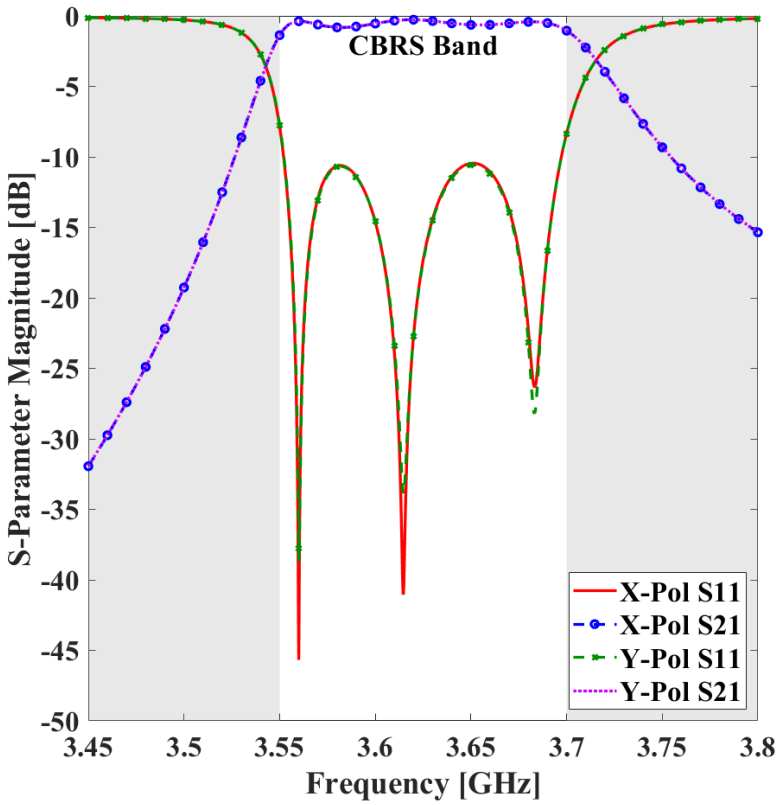

Figure 2.11: The filter response of the third-order filter

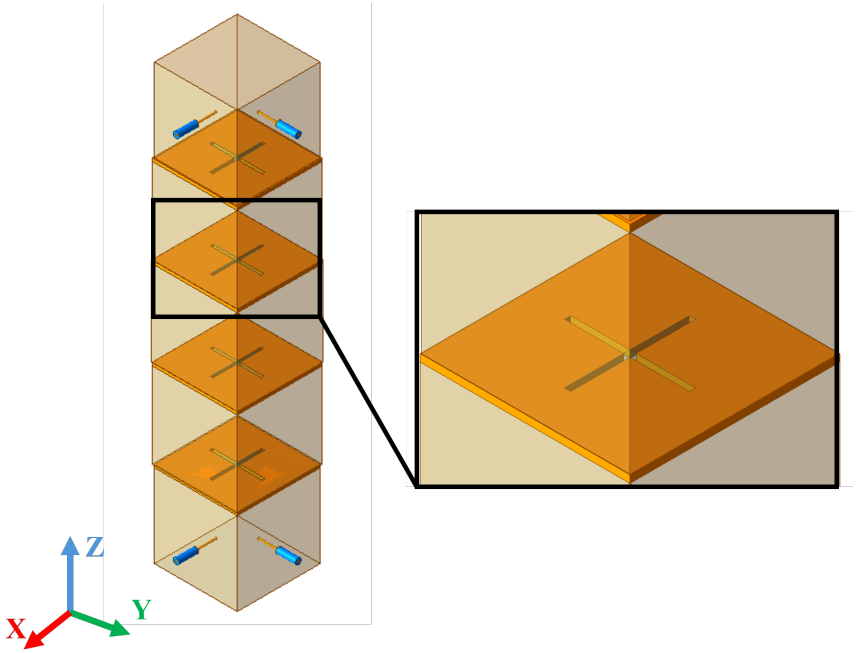

Figure 2.12: An image of the fifth-order cavity-resonator filter

2.7 Fifth Order Chebyshev Filter

A fifth-order Chebyshev filter with a 20 dB return-loss ripple and an FBW of 4.14% was also designed using the method detailed above. These filter specifications were chosen to increase the return-loss ripple, yielding a flatter passband. With higher orders, out-of-band rejection also increases. The filter topology is shown in Fig. 2.12, and the tuned filter response is shown in Fig. 2.13. An average insertion loss ripple of 19.3 dB was achieved with a fractional bandwidth of 4.01%. The fifth-order filter will be used to validate the matching method proposed in Chapter 4 across different filter orders.

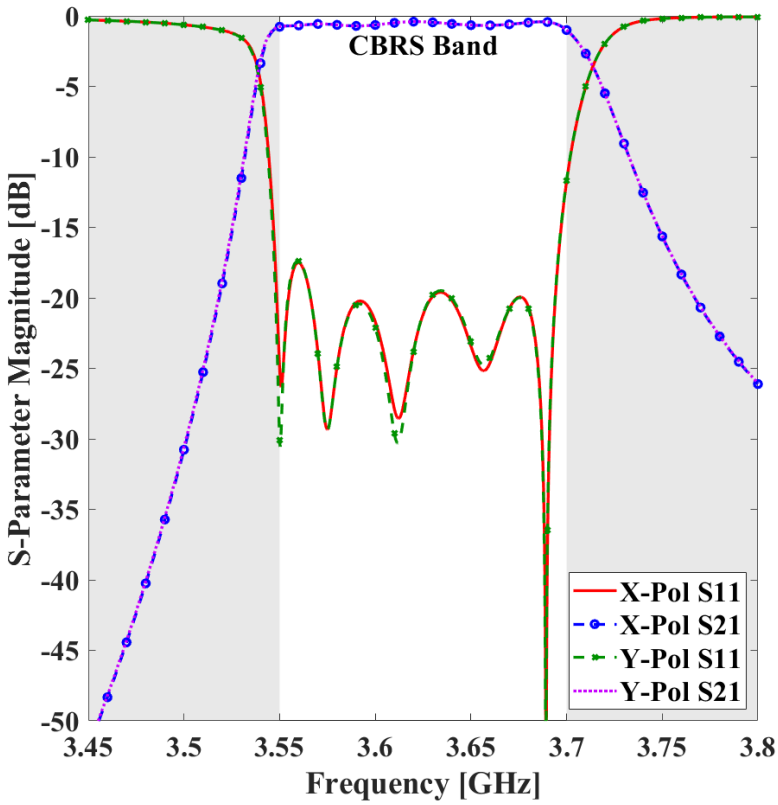

Figure 2.13: The filter response of the fifth-order filter

2.8 Conclusion

This chapter described the cavity resonator design and time-domain tuning methods. They were then applied to the design and tuning of a third-order and a fifth-order Chebyshev cavity filter. Tuned results for both filters were presented.

Chapter 3

Horn Design

Horn antennas are a popular choice for communications operations due to their wide bandwidth [43]. A wider bandwidth than the filter's will ensure the antenna acts as a load rather than a pole of the filter [5]. This chapter introduces the design of three different types of dual-polarized horn antennas. First, the design of conical, corrugated, and pyramidal horns fed through traditional waveguides (WG) is presented. A strategy is then presented for feeding both polarizations of all three horns by coupling the horn to a cavity feed through a cross-slot iris to create a method for tuning the Q_{rad} of the horn.

3.1 Conical Horn with Circular Waveguide

There are a variety of design methods to optimize different characteristics of conical horn antennas, such as bandwidth [44], directivity [43], and radiation pattern [45]. This work focuses on optimizing the conical horn antenna to later support optimal corrugation for spatial filtering. The design procedure in [46] was used to design the conical horn antenna that can be seen in Fig. 3.1 where a is the radius of the horn aperture, b is the radius of the feed waveguide, and c is the length of the horn.

The waveguide and conical horn were designed to have a return loss greater than 25 dB throughout the band of interest, indicating low power reflected back to the source as seen in

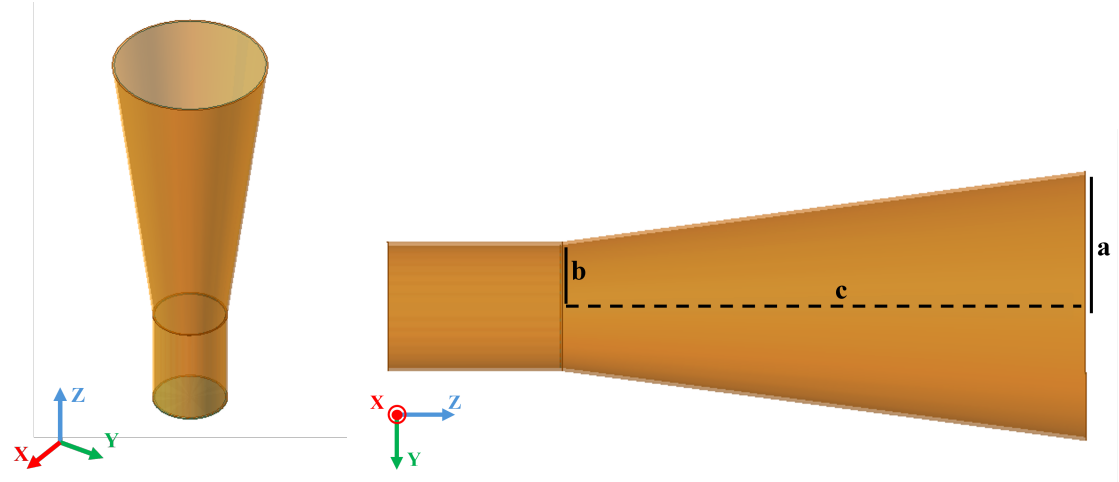

(a) **(b)**

Figure 3.1: Conical horn antenna fed with circular waveguide shown from an (a) isometric view, and (b) side view

Fig. 3.2a. The investigations carried out in Chapter 4 found that in order to achieve low Q_{ext} for matching the horns to the filters, it was advantageous to keep the input reactance of the horn as low as possible throughout the band of the desired filter. For all three horn antennas, this meant keeping the waveguide cutoff frequency as far from the operating frequency of the horn as possible without allowing the propagation of higher-order modes. The cutoff frequency was adjusted by changing the waveguide size. The input impedance for all three horn antennas is shown in Figs. 3.2b, 3.7b, and 3.11b. It is shown that the cutoff frequency occurs around 2.5 GHz, and that within the CBRS band, the input reactance remains near zero.

The realized gain of the conical horn can be seen in Fig. 3.3 with a max gain at boresight of 14.73 dB with a peak side-lobe level of -2.8 dB at 52° off of boresight in RG_θ at $\phi = 90^\circ$. It can also be seen that there is low cross-polarization, which is ideal for horns that support dual-polarization, as it prevents the two polarizations from interfering. Asymmetry in the radiation pattern can be seen between RG_θ at $\phi = 90^\circ$ and RG_ϕ at $\phi = 0^\circ$ even though the conical horn is circularly symmetric. This occurs because the TE_{11} mode that the conical

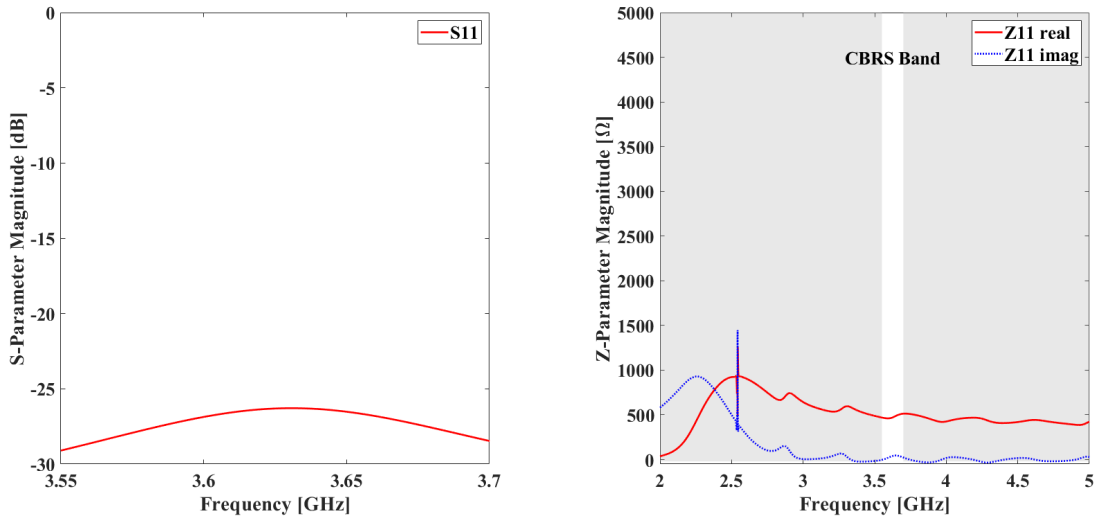

(a) **(b)**

Figure 3.2: The (a) S-Parameters, and (b) Z-Parameters of a conical horn antenna fed with a circular waveguide, excited by a single polarization

horn is fed with is not symmetric in both x and y-coordinates as shown in Fig. 3.5.

3.2 Corrugated Conical Horn with Circular

The sidelobe levels of the conical horn are only 16 dB lower than the main beam. High sidelobes in the horn's radiation pattern increase interference from surrounding transmitters in the same frequency band. An example of a high-sidelobe radiation pattern, compared with a lower-sidelobe pattern, in a physically congested environment is shown in Fig. 3.4. Circumferentially corrugated conical horns are a popular choice for reducing sidelobe levels and generating a rotationally symmetric main beam [47]. A corrugated horn was designed using the design curves for a narrowband corrugated horn antenna given in [46] and can be seen in Fig. 3.6. Sidelobe and backlobe radiation from horn antennas is largely caused by currents on the outside of the horn antenna [48]. Corrugations reduce sidelobe levels by varying the reactance along the length of the horn, which will induce the hybrid HE_{11} and the combined electric and magnetic modes reinforce in the center of the cavity and

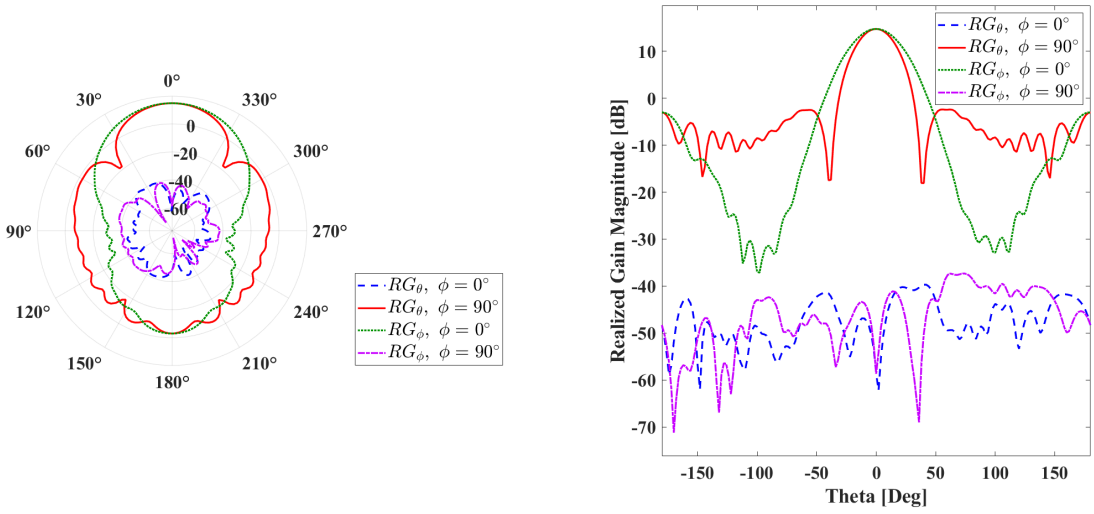

(a) **(b)**

Figure 3.3: The realized gain of a conical horn antenna fed with a circular waveguide with a single polarization in (a) polar, and (b) Cartesian format with a maximum gain of 14.73 dB at boresight

cancel around the perimeter of the horn aperture as shown in Fig. 3.5 [49]. This reduces the currents that travel from the aperture down the sides of the horn. Due to the transition from the TE_{11} mode to the hybrid HE_{11}, the radiation pattern is circularly symmetric because the HE_{11} mode is symmetric in E- and H-planes [49].

The waveguide and corrugated horn were matched to give a return loss greater than 24 dB, shown in Fig. 3.7a, across the band of interest. The same waveguide used for the conical horn was used for the corrugated horn to ensure low input reactance in the CBRS band, seen in Fig. 3.7b.

The realized gain for this corrugated horn can be seen in Fig. 3.8 with a max gain of 13.23 dB at boresight with peak sidelobe levels of -26.64 dB at 92 degrees off of boresight. There is a 1.5 dB reduction in peak gain of the main beam at boresight. This is due to the beamwidth widening slightly compared to the conical horn. A comparison between the normalized realized gain of the conical and the corrugated horns can be seen in Fig. 3.9. It can be seen that the 3 dB beamwidth increases from $16°$ in θ to about $24°$ in θ when

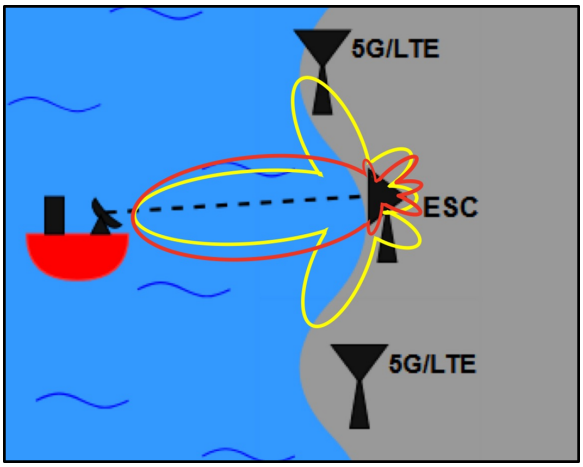

Figure 3.4: Diagram of spatial filtering through reduced sidelobes where the yellow radiation pattern demonstrates a traditional horn and the red radiation pattern demonstrates a horn with spatial filtering

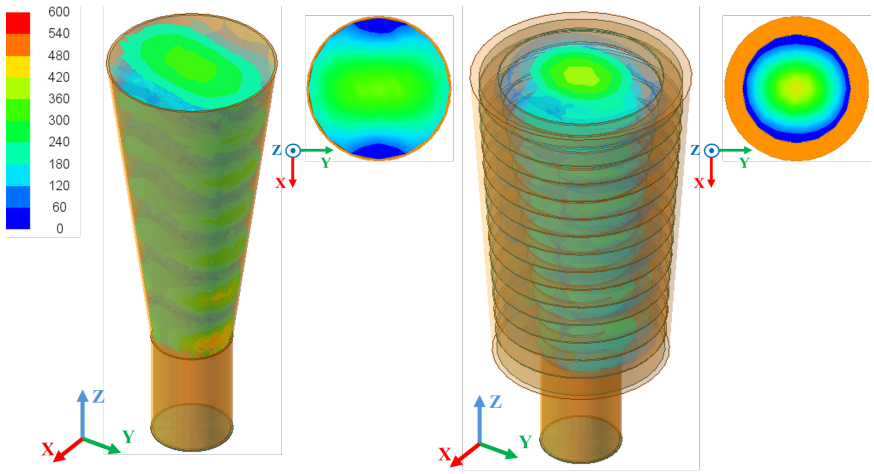

Figure 3.5: Comparison of the electric field distributions for a conical horn antenna compared to a corrugated horn antenna

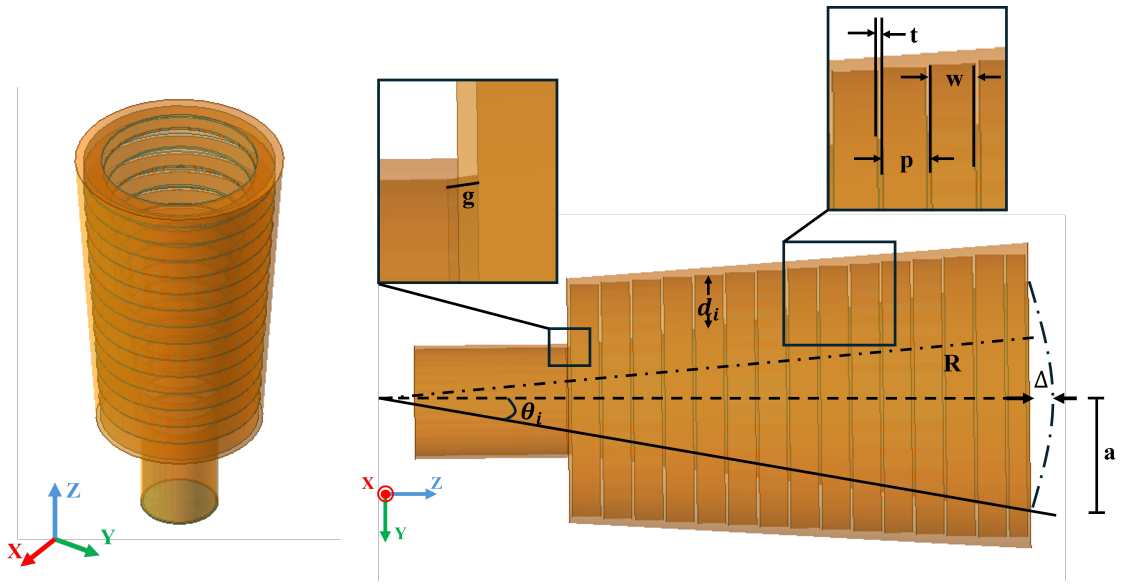

(a) **(b)**

Figure 3.6: Corrugated horn antenna fed with circular waveguide shown from an (a) isometric view, and (b) side view

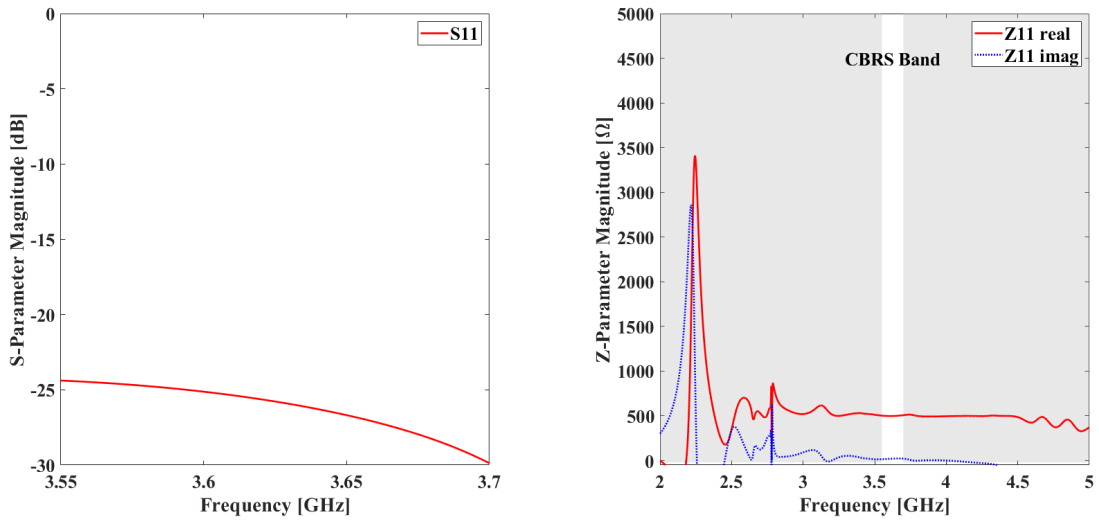

(a) **(b)**

Figure 3.7: The (a) S-Parameters, and (b) Z-Parameters of a corrugated conical horn antenna fed with a circular waveguide, excited by a single polarization

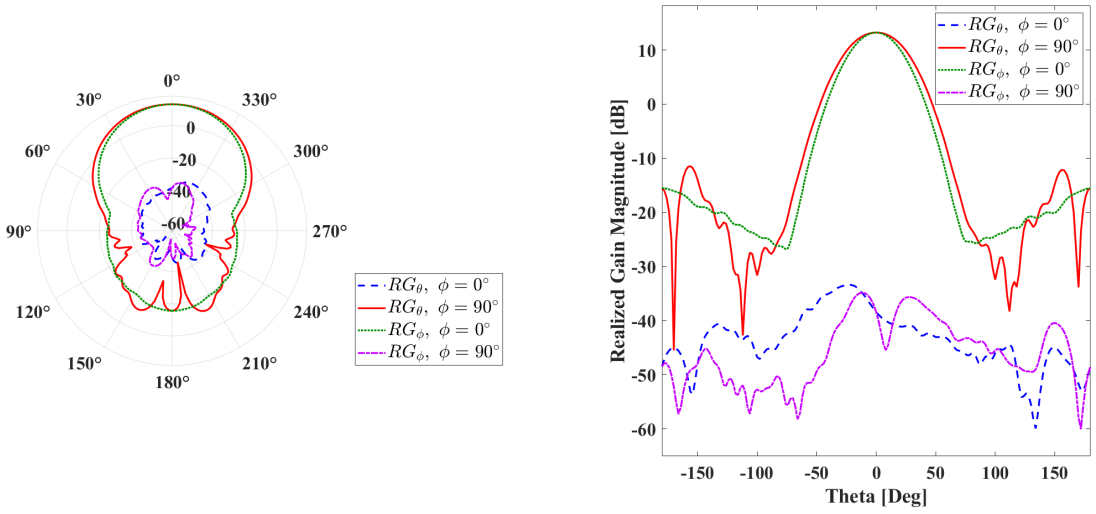

(a) **(b)**

Figure 3.8: The realized gain of a corrugated conical horn antenna fed with a circular waveguide with a single polarization in (a) polar plot, and (b) Cartesian format with a maximum gain of 13.23 dB at boresight

corrugations are introduced. It can also be seen that the separation between the sidelobe and the main beam is 39 dB for the corrugated case and only 17 dB for the high-sidelobe plane of the conical horn. It can also be noted that the corrugated horn successfully introduces circular symmetry, giving both E- and H-planes low sidelobes and identical radiation patterns.

3.3 Pyramidal Horn with Square Waveguide Design

A pyramidal horn fed by a square waveguide was designed with [49] as a starting point and optimized for an ideal radiation pattern in Ansys HFSS. It was designed with a return loss greater than 20 dB across the band, shown in Fig. 3.11a. The waveguide was once again designed to ensure cutoff was well below the filtering band, giving low input reactance, shown in Fig. 3.11b.

The realized gain for the waveguide-fed pyramidal horn can be seen in Fig. 3.12 with a max realized gain of 12.62 dB at boresight and a peak sidelobe level of -7.4 dB at about $86°$

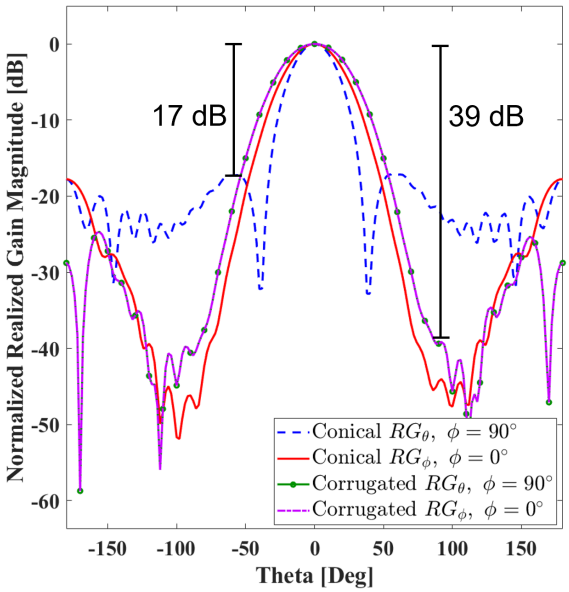

Figure 3.9: Comparison of the normalized realized gain of the conical horn compared to the normalized realized gain of the corrugated horn for sidelobe separation comparison

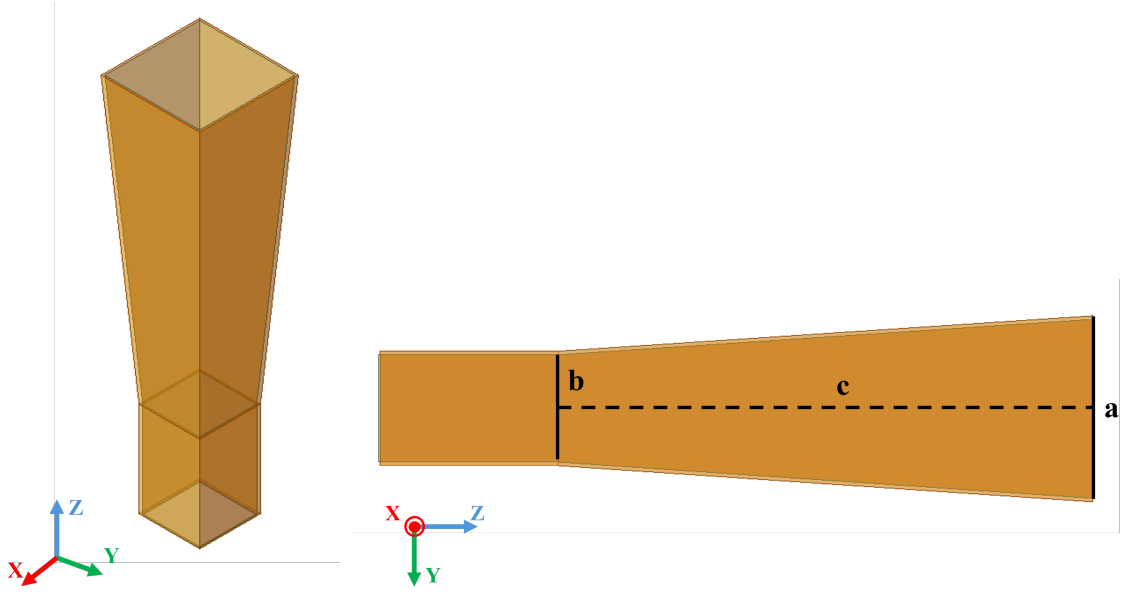

(a) **(b)**

Figure 3.10: Pyramidal horn antenna fed with circular waveguide shown from an (a) isometric view, and (b) side view

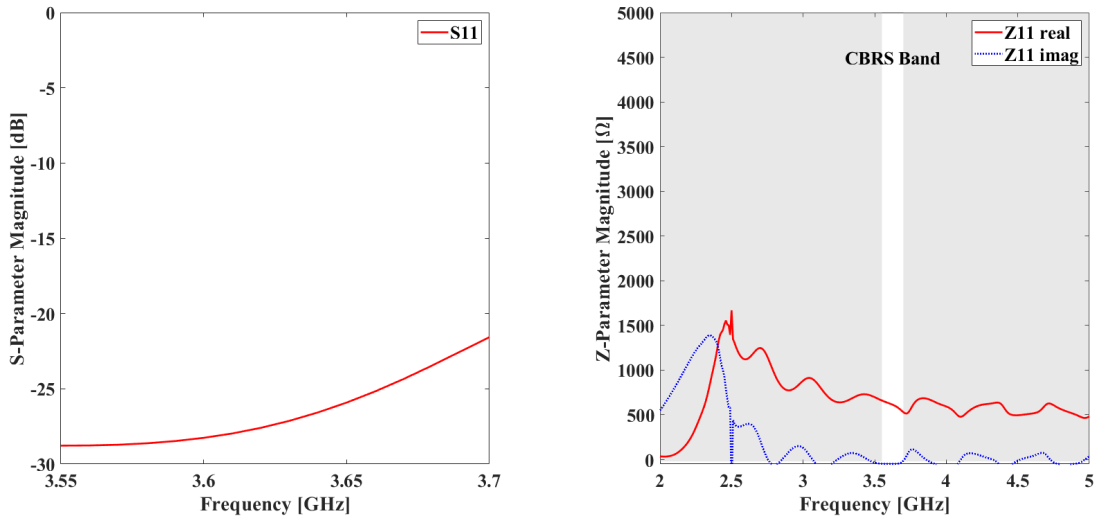

(a) **(b)**

Figure 3.11: The (a) S-Parameters, and (b) Z-Parameters of a pyramidal horn antenna fed with a square waveguide, excited by a single polarization

off of boresight.

3.4 Iris-Fed Horns

It was necessary to design a method to control the coupling between a cavity feed and the previously discussed horns. For this, the cross-slot iris design was chosen for its ability to magnetically couple orthogonal polarizations with low cross-coupling. It was important that the iris-coupled horn maintained the same radiation pattern and achieved the same gain at boresight as the waveguide-fed horn. Fig. 3.13 compares a dual-polarized conical horn fed with a traditional circular waveguide with the same conical horn fed with a cavity excited by a coaxial probe and coupled to the horn via the cross-slot iris. The realized gain and radiation patterns are nearly identical aside from the waveguide-fed horn having slightly deeper nulls at the edges of the main beam and some slight changes in the side and back lobes. The main beam gain remains identical.

The iris-coupled conical horn antenna, shown in Fig. 3.14, exhibited narrow-band

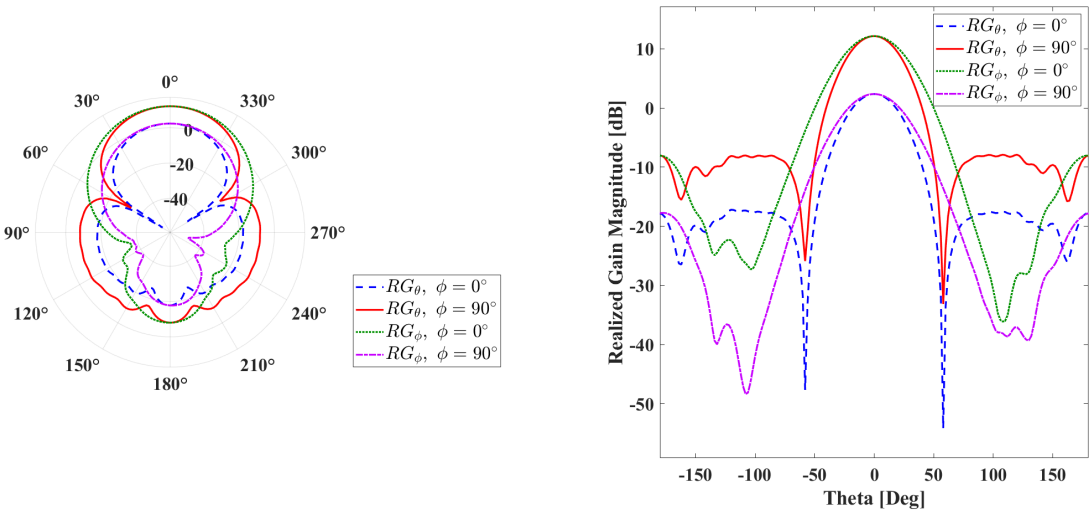

(a) **(b)**

Figure 3.12: The realized gain of a pyramidal horn antenna fed with a square waveguide with a single polarization in (a) polar plot, and (b) Cartesian format with a maximum gain of 12.62 dB at boresight

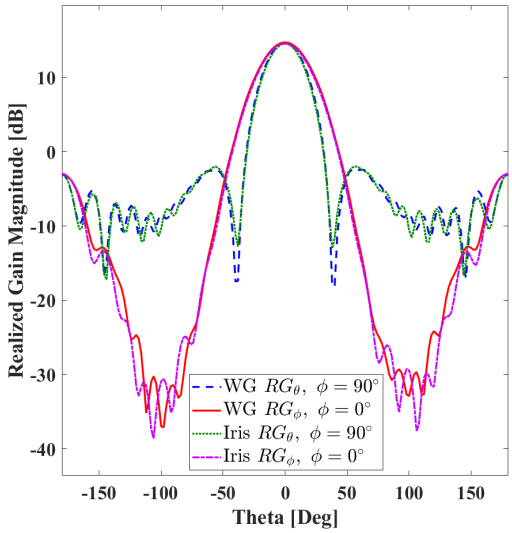

Figure 3.13: Comparison of the realized gain of a dual-polarized waveguide-fed conical horn compared to the realized gain of a dual-polarized iris coupled cavity-fed conical horn for realized gain comparison

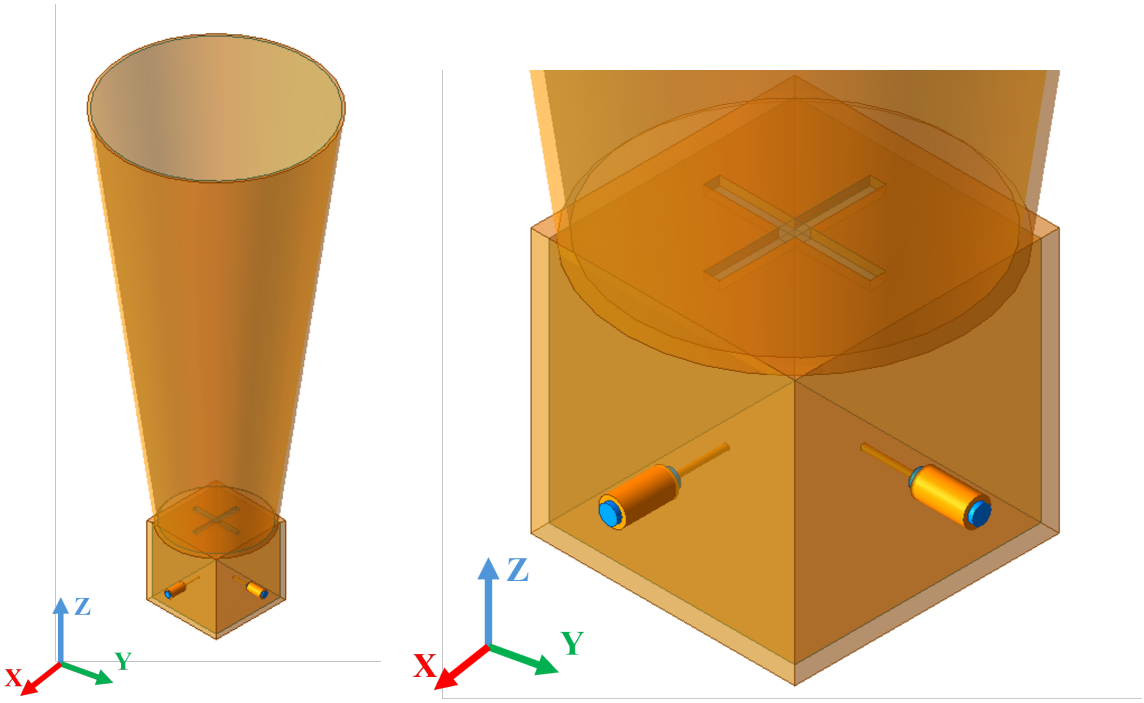

(a) **(b)**

Figure 3.14: The (a) full conical horn fed by an iris coupled cavity, and (b) a close-up of the coaxial feed, cavity, and iris for the conical horn

behavior in the reflection coefficient due to the resonance of the cavity feed, and the conical horn was matched at the center frequency to achieve a return loss of approximately 20 dB, as shown in Fig. 3.15.

The radiation patterns for both E- and H- planes for both feeds are shown in Fig. 3.16. The maximum gain at boresight for both feeds is 14.57 dB. With a separation between co-polarized and cross-polarized gain of 21 dB.

The iris-coupled corrugated conical horn antenna, shown in Fig. 3.17, exhibited narrow-band behavior in the reflection coefficient due to the resonance of the cavity feed, and the conical horn was matched at the center frequency to achieve a return loss of approximately 20 dB, as shown in Fig. 3.18.

The radiation patterns for both E- and H- planes for both feeds are shown in Fig. 3.19. The maximum gain at boresight is 13.04 dB. With a separation between co-polarized and

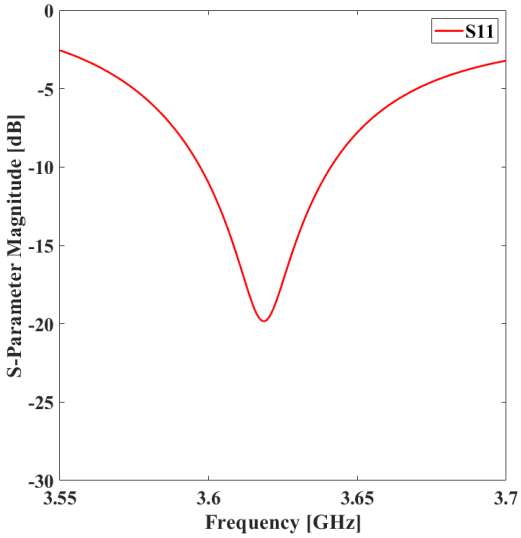

Figure 3.15: Return loss of the conical horn fed by the iris-coupled cavity

cross-polarized gain of 20.58 dB. The minimum separation between the main beam and the peak sidelobe for either polarization is 37.1 dB.

The iris-coupled pyramidal horn antenna, shown in Fig. 3.20, exhibited narrow-band behavior in the reflection coefficient due to the resonance of the cavity feed, and the conical horn was matched at the center frequency to achieve a return loss of approximately 20 dB, as shown in Fig. 3.21.

The radiation patterns for both E- and H- planes for both feeds are shown in Fig. 3.22. The maximum gain at boresight for both feeds is 12.44 dB. With a separation between co-polarized and cross-polarized gain of 23.23 dB. This is higher than the waveguide-fed pyramidal horn because of the strict polarization separation of the cross-slot coupled feed.

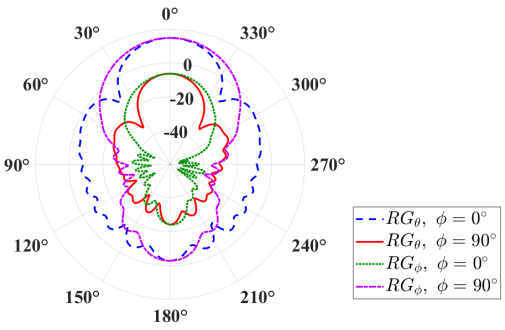

(a)

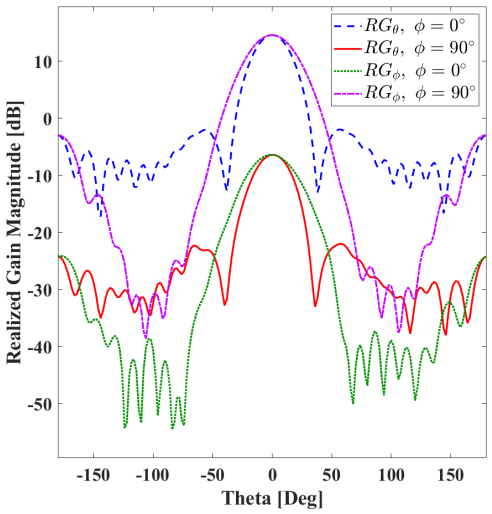

(b)

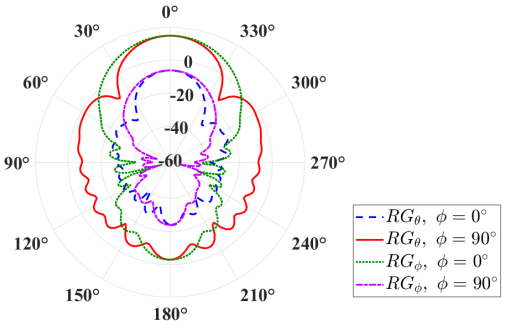

(c)

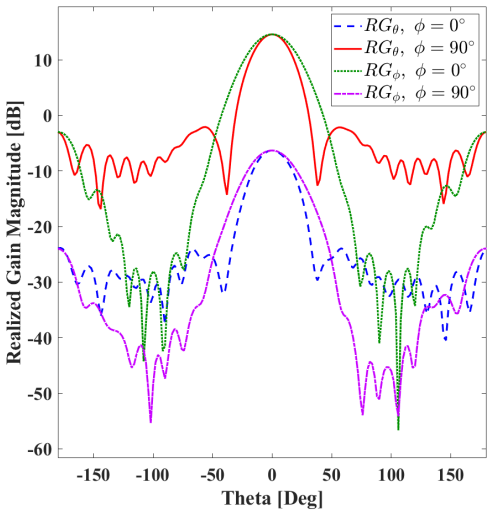

(d)

Figure 3.16: The realized gain of the conical horn for the x-polarized feed in (a) polar and (b) Cartesian, and for the y-polarized feed in (c) polar and (d) Cartesian, with a maximum boresight gain of 14.57 dB

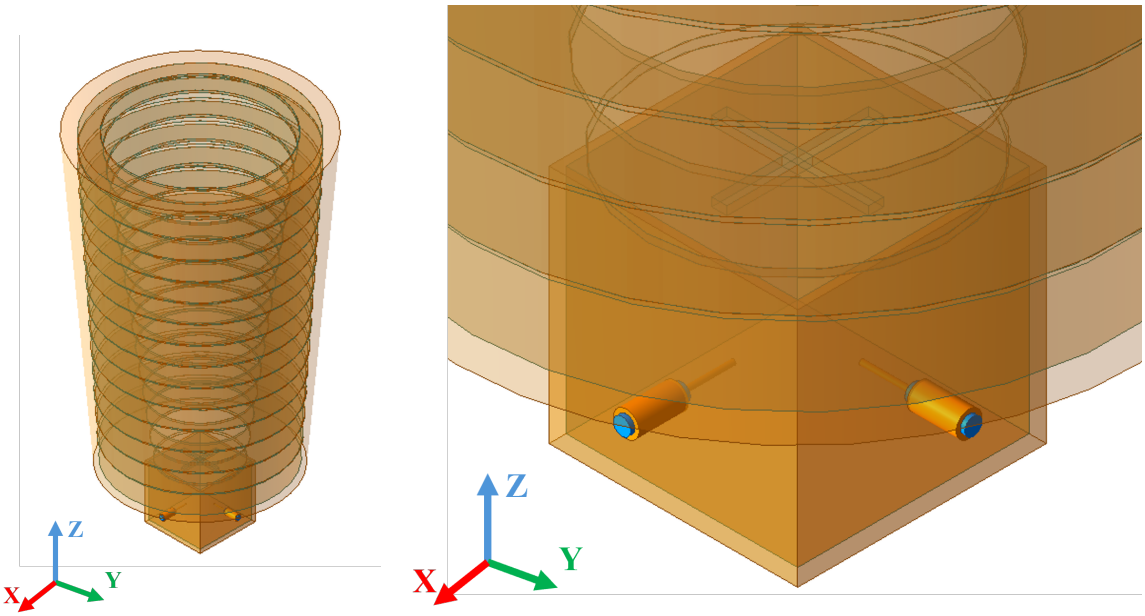

(a) **(b)**

Figure 3.17: The (a) full corrugated conical horn fed by an iris coupled cavity, and (b) a close-up of the coaxial feed, cavity, and iris for the corrugated conical horn

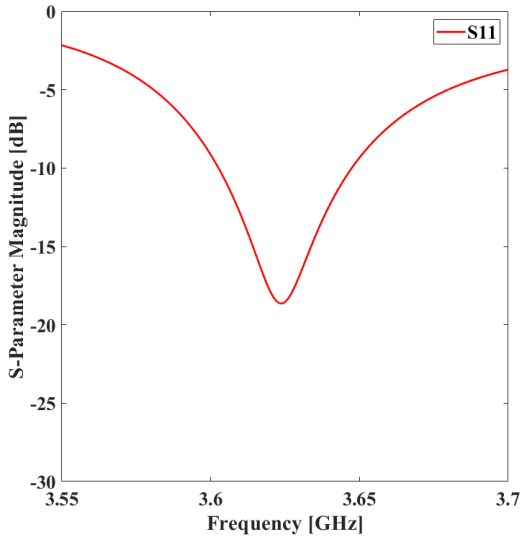

Figure 3.18: Return loss of the corrugated conical horn fed by the iris-coupled cavity

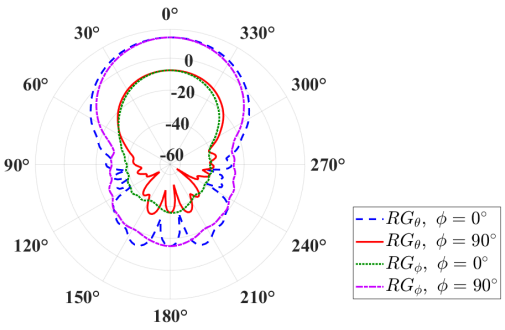

(a)

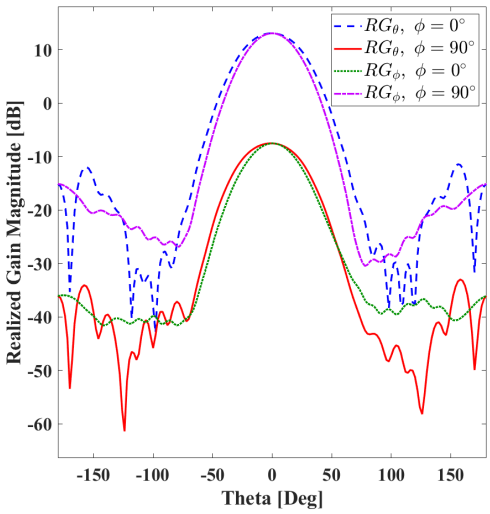

(b)

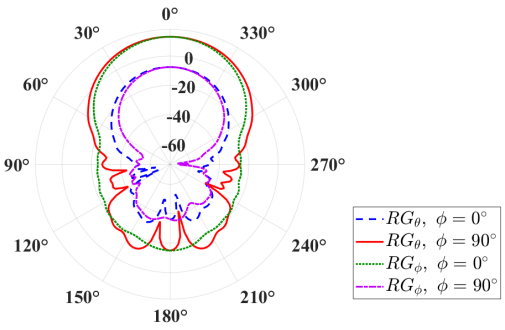

(c)

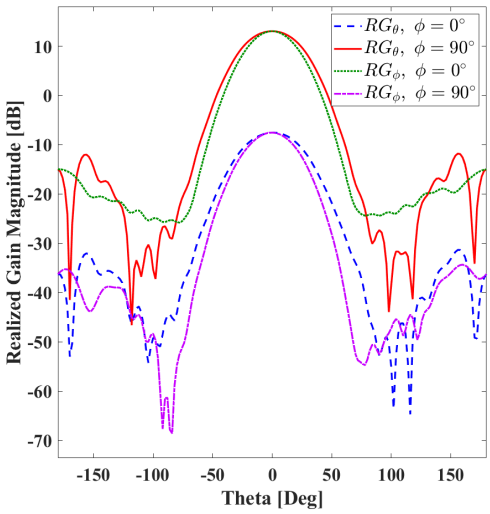

(d)

Figure 3.19: The realized gain of the corrugated conical horn for the x-polarized feed in (a) polar and (b) Cartesian, and for the y-polarized feed in (c) polar and (d) Cartesian, with a maximum boresight gain of 13.04 dB

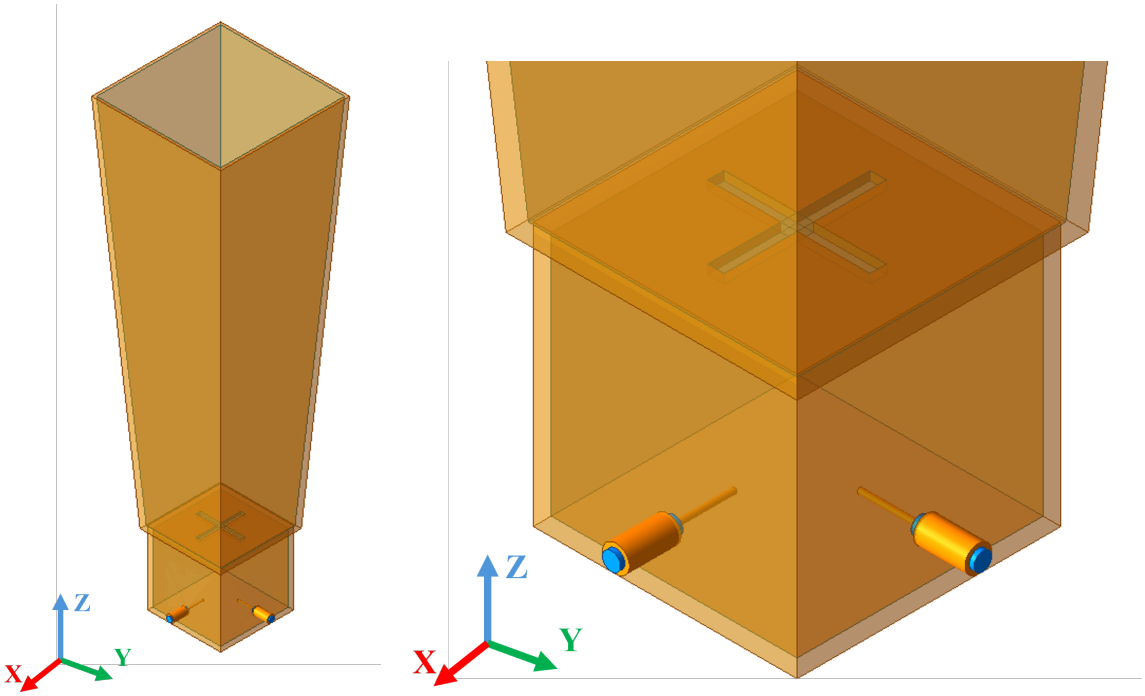

(a) **(b)**

Figure 3.20: The (a) full pyramidal horn fed by an iris coupled cavity, and (b) a close-up of the coaxial feed, cavity, and iris for the pyramidal horn

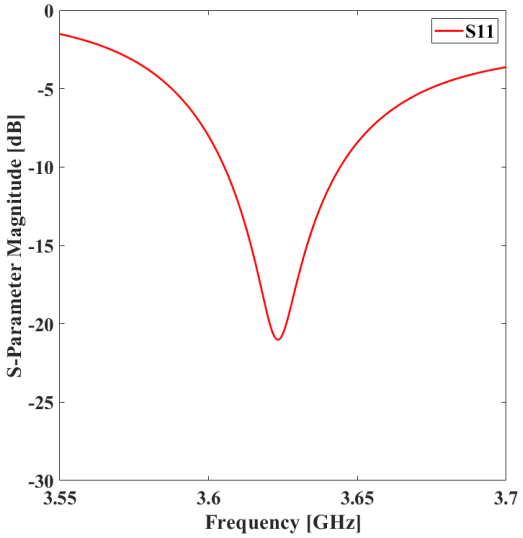

Figure 3.21: Return loss of the pyramidal horn fed by the iris-coupled cavity

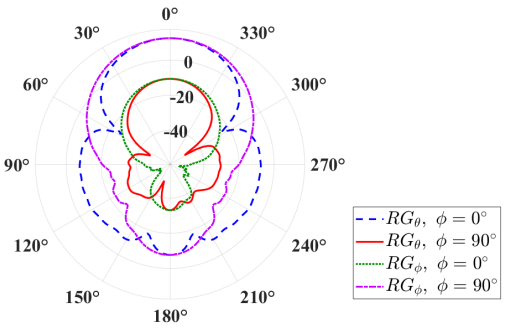

(a)

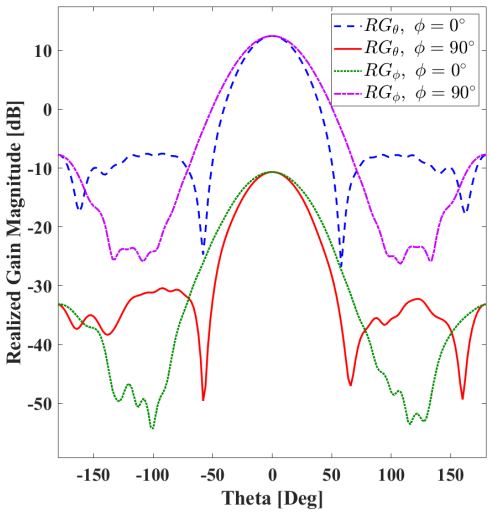

(b)

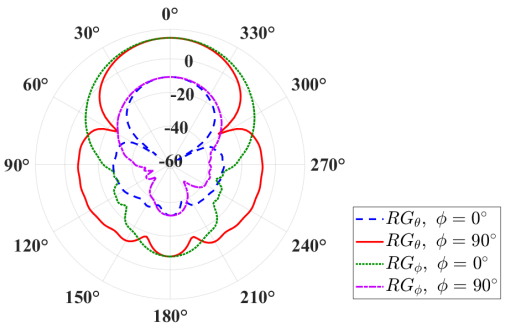

(c)

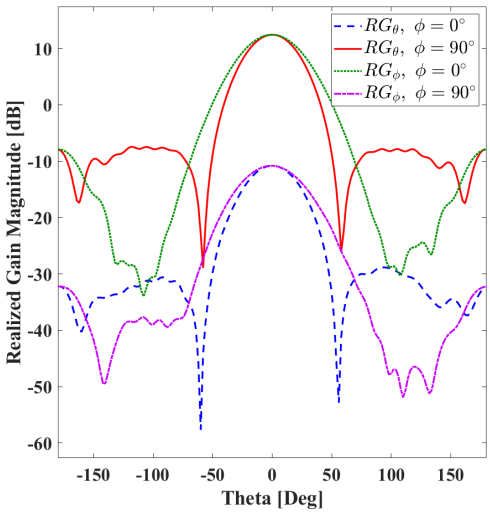

(d)

Figure 3.22: The realized gain of the pyramidal horn for the x-polarized feed in (a) polar and (b) cartesian and for the y-polarized feed in (c) polar and (d) Cartesian, with a maximum boresight gain of 12.44 dB

3.5 Conclusion

The design of a conical, a corrugated, and a pyramidal horn was demonstrated. A method for creating a tunable Q_{ext} of the horns was presented and validated. It is implemented without impacting the horn's performance. In Chapter 4, this tunable Q_{ext} method will be used to design the Q_{ext} of the horns to match the Q_{ext} of the tuned cavity resonator filters discussed in Chapter 2.

Chapter 4

Analyzing Q_{ext} of a horn for matching to filter

Horn antennas are not designed to be resonant at their center frequency. Instead, they present a complex load impedance where they attach to the feed structure. Some narrowband behavior can be introduced through the use of an iris to couple between the last cavity of the filter and the antenna; however, this is the resonance of the cavity, not the resonance of the horn antenna. A circuit diagram of a horn antenna serving as a complex load at the output of a third-order cavity resonator filter is shown in Fig. 4.1, while the circuit diagram of a resonant antenna, in this example, it is a slot antenna acting as a parallel resonator, can be seen in Fig. 4.2. It should be noted that the complex load introduced by the horn will have both reactance and resistance, but it cannot be represented by a single RLC tank at f_0. This behavior is shown in the input impedance behavior comparison in Fig. 4.3. An example of the impedance behavior of a resonant structure adapted from [50], shown in Fig. 4.3a, will have a reactance that crosses zero at the resonant frequency and that will coincide with a peak in the resistance. The horn antenna does not exhibit this same resonant behavior as shown in Fig. 4.3b.

As the Q_{rad} [32] [31] and RLC representations [33] both operate under the assumption that the radiator is resonant at the center frequency of the filter, f_0, these methods cannot be used to derive the Q_{ext} that a horn antenna presents at the load of the filter.

This chapter details a proposed matching method for matching a dual-polarized horn

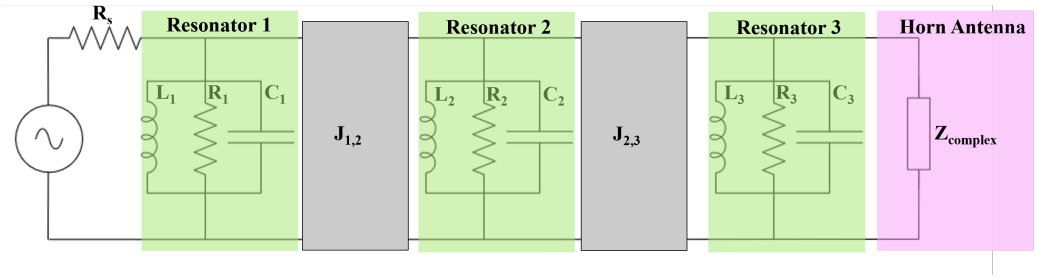

Figure 4.1: Circuit diagram of a horn acting as a complex load at the output of a third-order cavity resonator filter

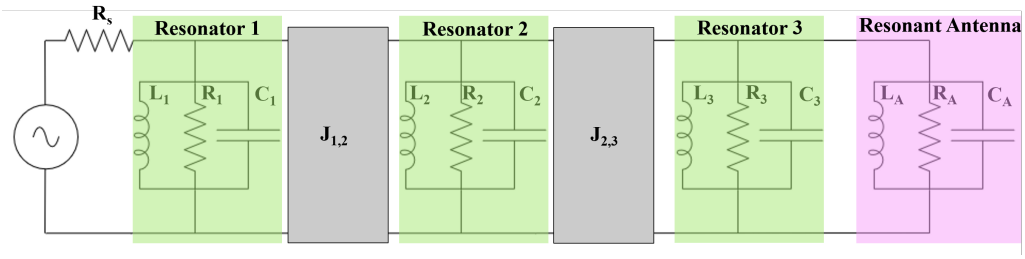

Figure 4.2: Circuit diagram of a slot antenna acting as a resonant structure at the output of a third-order cavity resonator filter

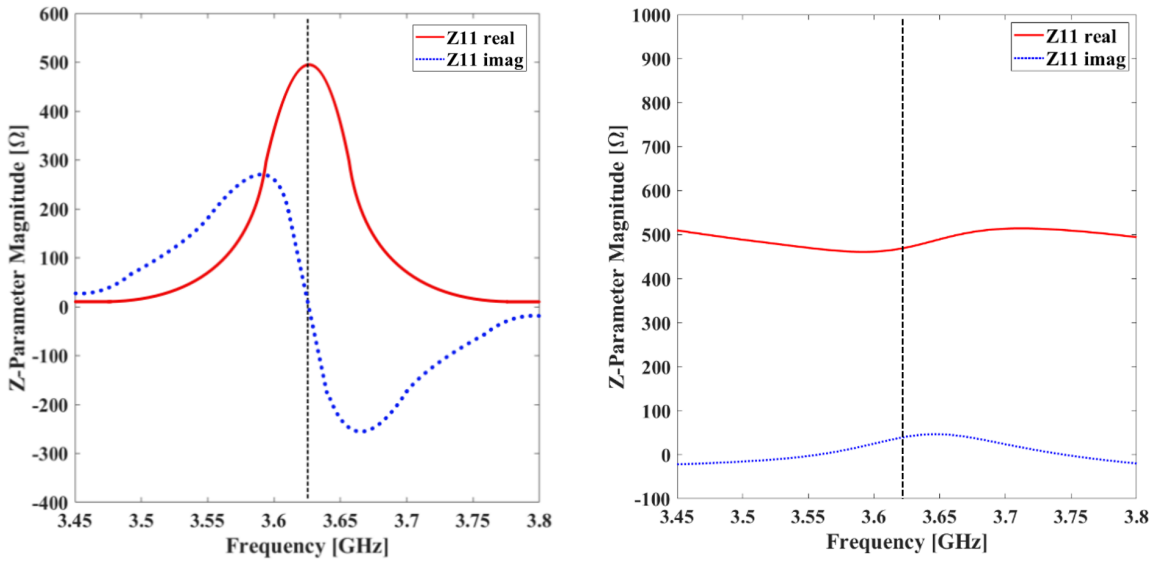

(a) **(b)**

Figure 4.3: (a) An example of the input impedance behavior expected for a slot antenna acting as a parallel resonator, and (b) the input impedance behavior of the conical horn antenna

antenna to a dual-channel cavity filter. It was necessary first to determine the Q_{ext} value needed for the tuned filter, then design an iris-coupled horn antenna to match this necessary value. Properly matching a dual-polarized horn antenna to a filter with Q_{ext} matching reduces computational power and time needed for tuning. It will enable the widespread implementation of cascaded filtering horn antennas with reduced design time. A conical horn attached directly to a cavity filter can be seen in Fig. 4.4a. The iris between the last cavity and the base of the horn is simply a circle that is the diameter of the width of the cavity, as shown in Fig. 4.4b. The frequency domain filter response, time domain group delay magnitude, and time domain magnitude can be seen in Fig. 4.5a, 4.5b, and 4.5c, respectively. It can be seen that the passband of the filter/horn is narrower than the original filter, and there are only two apparent nulls. There is also a decrease in the return loss ripple of more than 15 dB within the passband. This filter/horn requires a long, involved tuning process to return to match the initial filter response. A method of matching the horn to the filter by matching the Q_{ext} of the horn and the filter greatly hastens this process.

4.1 Q_{ext} of filter

Chapter 2 discussed how to calculate the Q_{ext} necessary for the synthesis of a cavity resonator filter from the lowpass prototype g-coefficients. However, those were a starting point, and the tuned filter likely has a slightly different tuned Q_{ext} than calculated. Therefore, it is first necessary to extract what the Q_{ext} of the tuned filter is.

The group delay method discussed in Chapter 2 for extracting the group delay of a singly-terminated cavity from EM full-wave simulation can be used to extract the Q_{ext2} of the tuned filter when the simulation is run using identical dimensions as the last cavity/port of the tuned filter. This, however, can pose problems when the group-delay peak is not centered at f_0 in the dual-channel case. The author of [33] discusses the need to de-embed

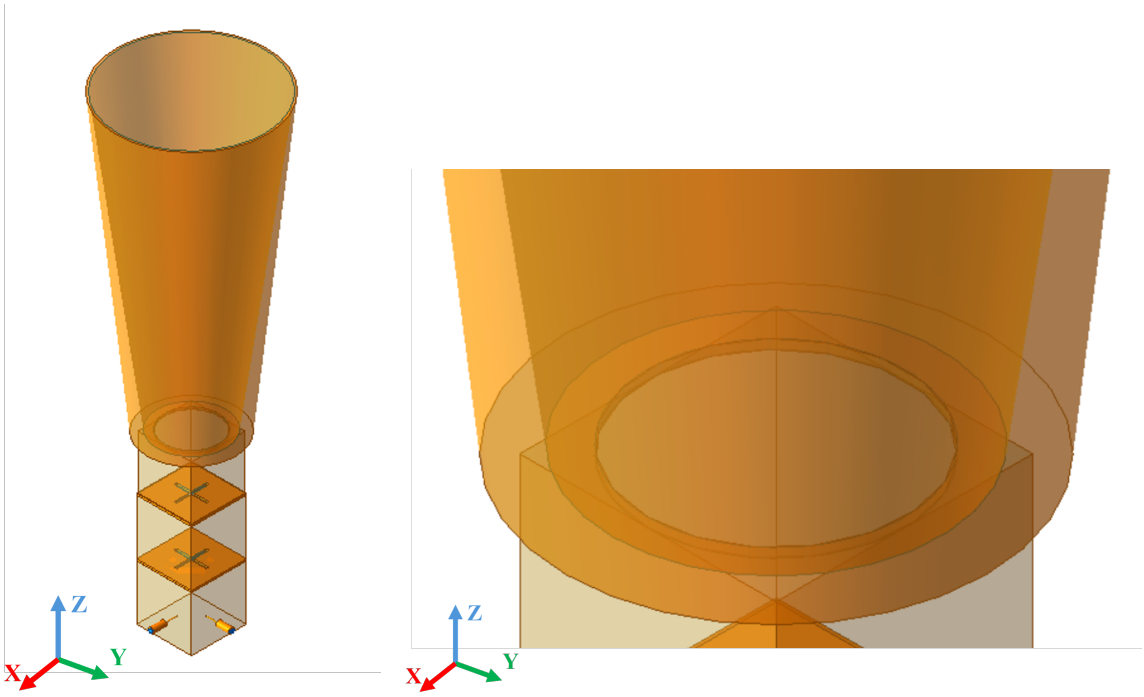

(a) **(b)**

Figure 4.4: The (a) full filter cascaded with the conical horn without a designed iris, and (b) a close-up of the feed between the filter and the conical horn

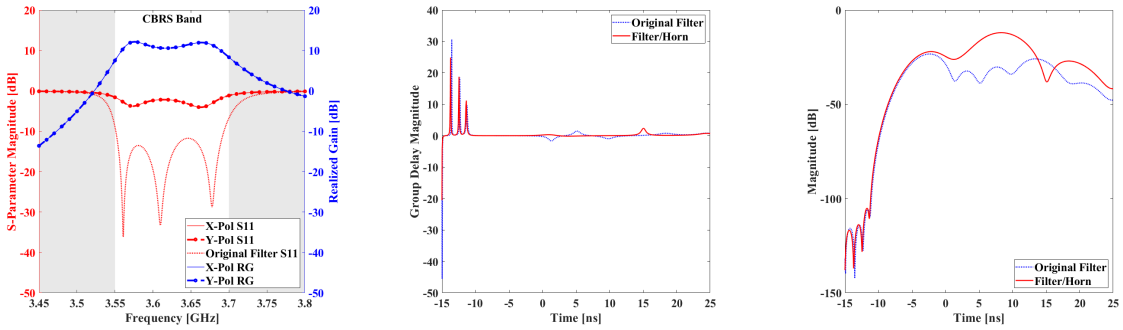

(a) **(b)** **(c)**

Figure 4.5: The (a) frequency-domain filter response, (b) time-domain group delay magnitude, and (c) time-domain magnitude of a dual-polarized, conical horn antenna directly attached to a third-order filter without matching or a specific iris

the feed to keep the group-delay peak/phase shift at the center frequency. In the case of a dual-channel cubic cavity, de-embedding would affect only a single polarization. Ansys HFSS also treats waveport simulations as a waveguide. It becomes necessary to use a coaxial probe feed (or a similar coupled feed) to simulate the required cavity modes, making it impossible to de-embed into the cavity to center the peak at f_0, since the waveport is placed outside the cavity to simulate a transmission line. The cavity size then needs to be adjusted to center the group-delay peak at f_0. When adjusting the cavity size, the coaxial feed's location relative to the cavity's magnetic fields also changes, which can affect coupling into the mode. Different methods for extracting the Q_{ext} of the tuned horn were investigated using the group delay extraction method and using a method of analyzing coax coupling into resonators by plotting the reflection coefficient on the Smith chart discussed in [51].

A resonator operating near resonance will demonstrate a circle when the reflection coefficient is plotted across frequency [51]. The diameter (d) of this circle corresponds to the coupling coefficient (κ) as $\kappa = \frac{d}{2-d}$ [51]. Then the loaded quality factor can be determined from $Q_L = \frac{Q_0}{1+\kappa}$ or $Q_L = \frac{f_L}{f_1 - f_2} \tan \phi_L$ where f_L is the center frequency of the loaded cavity, ϕ_L is the arbitrary angle chosen for calculating diameter, and f_1 and f_2 are the frequencies corresponding to $\pm\phi_L$. For all assumptions and derivations, refer to [51]. However, upon application of this method in the Q_{ext} extraction of a coaxial probe coupled filter, the values obtained for Q_{ext} were not logical for a cavity resonator coupled using a coaxial probe. Upon further investigation, it was found that [51] does not hold when coupling is strong [52], and the horn required strong coupling into the cavity for proper coupling to the horn for excitation. Therefore, the best method available for this structure is the extraction of Q_{ext} using the group delay method described in [41].

4.2 Extracting Q_{ext} of a Horn Antenna

The next challenge is in extracting the Q_{ext} of the horn antenna. There are a few established methods for extracting the Q_{ext} of an antenna [33] [31], however, they rely on the antenna itself being a resonant structure and cannot be applied to Q_{ext} extraction of a horn. However, with some considerations, the group delay method used to find the Q_{ext} of the coaxial fed cavities can be applied to extract the Q_{ext} of the iris-coupled horn antenna.

The simulation for extracting the Q_{ext} of the horn antenna using group delay needs to operate with the proper cavity modes, so it needs to be excited with a coaxial probe. This structure can be seen in Fig. 4.6a. It should be noted that the Q_{ext} of the horn was extracted using a single coax feed, but the full cross-slot was simulated as the off-polarization slot will still affect the overall coupling of the horn slightly. Through symmetry, the dimensions were later applied to the dual-polarized filter/horns. The diagram of dimensions used for matching can be seen in Fig. 4.6b. The cavity size also has to be adjusted to keep the group delay centered at f_0. There is also the challenge of extracting the Q_{ext} of the horn only, without the effects of the coupling of the coaxial probe being included in this value. The effects of the coaxial feed were extracted using group delay in a separate simulation of a singly-excited cavity in an attempt to remove the effects of the coaxial feed to the horn simulation from the final values for horn Q_{ext}.

4.3 Matching Methods

Five methods were tested to extract the Q_{ext} from the filter. The simulated structure can be seen in Fig. 4.7. The first method was to extract the group delay at f_0 without shifting the cavity size ($CavW$). This means the peak group delay did not occur at f_0. The second method was to adjust the peak group delay to f_0, keeping the coaxial probe distance (CoaxOffset) from the cavity wall constant as the cavity size changed. The third method

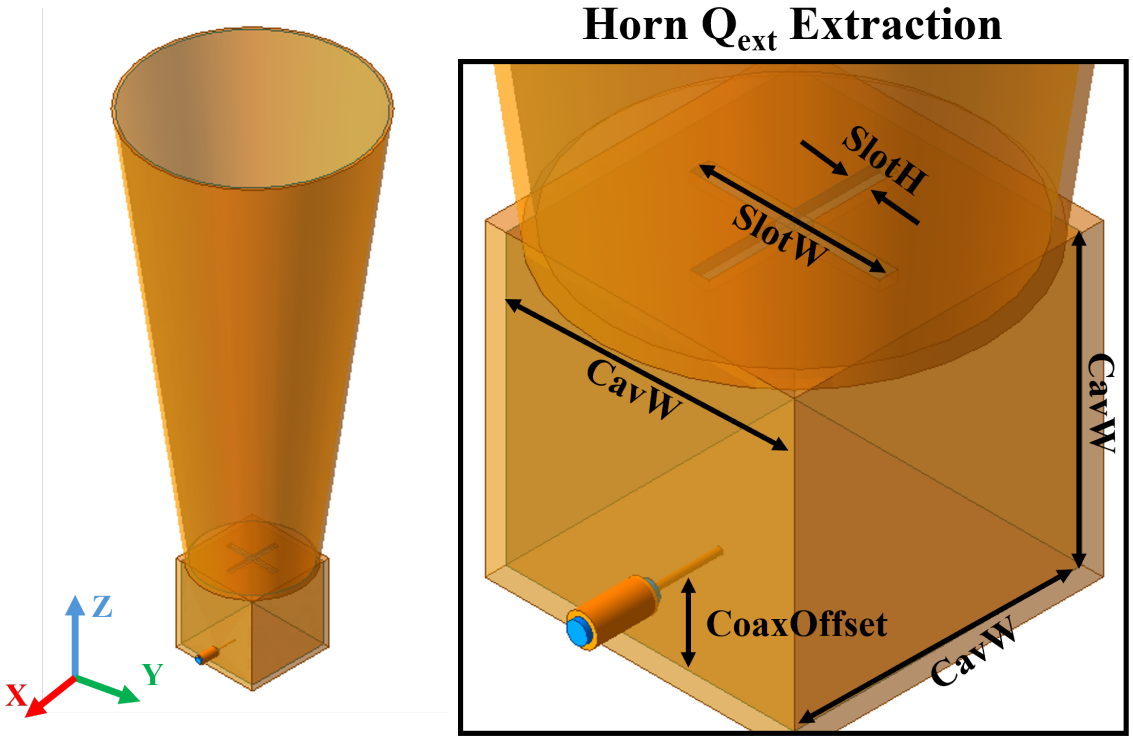

(a) **(b)**

Figure 4.6: The (a) full view, and (b) the zoomed view of a conical horn antenna fed by an iris-coupled cavity.

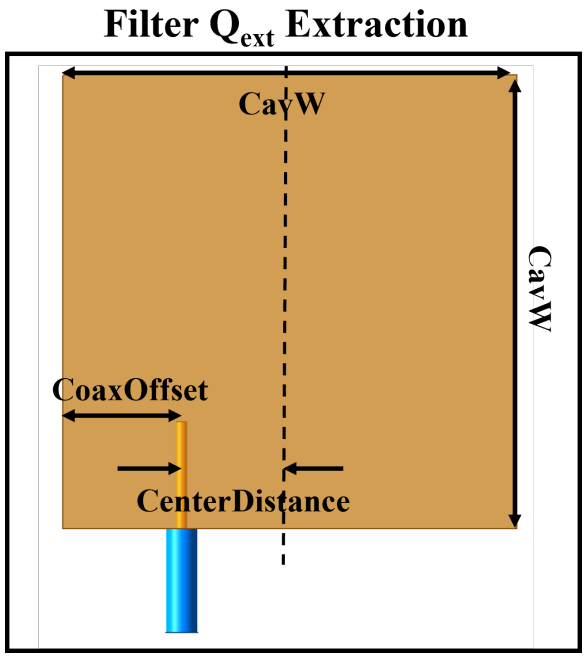

Figure 4.7: Diagram of the filter Q_{ext} extraction

was to take the peak group delay at the frequency it occurs f_{peak} and match the horn to this group delay at that frequency. The fourth method was to shift the peak group delay to f_0 by changing (CavW) and adjusting (CoaxOffset) in proportion to the new cavity size relative to the old cavity size. This may be an iterative process if the group-delay peak shifts as the coaxial probe position is changed. Finally, the fifth method was to shift the peak group delay to f_0 using $CavW$ and keeping the coaxial probe distance from the center of the cavity consistent as the cavity size changed. This keeps the coaxial probe, an inductive feed structure, in a consistent location relative to the magnetic field distribution in the cavity.

It was also necessary to test the methods for accounting for the Q_{ext} of the coaxial feed of the cavity-fed iris-coupled horn simulation. This was accomplished by extracting the group delay of the single cavity fed with the coaxial probe, with the probe size and location, and the cavity size matching those of the cavity-fed iris-coupled horn simulation. A diagram of the simulation used to find the effects of the coaxial feed can be seen in Fig. 4.9. For all methods except for Method 3, an attempt was made to de-embed the Q_{ext} of

the coaxial probe feed. Cavity size ($CavW$) began as the size of the cavity-fed iris-coupled horn simulation. The coaxial probe location began with the same location as the cavity-fed iris-coupled horn simulation. The effects of the coaxial probe feed were calculated using

$$\frac{1}{Q_{probe,iris,horn}} = \frac{1}{Q_{probe}} + \frac{1}{Q_{horn}} \tag{4.1}$$

where Q_{probe} is the Q_{ext} found when simulating the singly-terminated cavity with the coaxial feed, Q_{horn} is the Q_{ext} presented by the horn, and $Q_{probe,iris,horn}$ is the Q_{ext} presented by the group delay of the cavity-fed iris-coupled horn antenna simulation. By setting Q_{horn} equal to the Q_{ext} of the tuned filter, the necessary group delay of the cavity-fed iris-coupled horn simulation can be found that accounts for the Q_{ext} of the coaxial probe. This coaxial probe de-embedding process can be iterative. When matching the cavity-fed iris-coupled horn simulation to the new group delay, it may be necessary to change the cavity dimensions, and the entire process may need to be repeated.

Extracting the coaxial feed effects using the group delay method required the same considerations as those applied to extracting the Q_{ext} of the tuned filter. The coaxial probe, simulated as a single feed to a cavity with the same dimensions as the cavity-fed iris-coupled horn simulation, had a peak centered at 3.775 GHz, as shown in Fig. 4.8. Method 1 was tested without accounting for the coaxial feed effects and with the coaxial probes accounted for, using group-delay shifted with $CavW$ to get the peak at f_0. Method 2 was tested both without accounting for the coaxial probe effects and with them accounted for using group delay shifted using $CavW$ to get the peak at f_0. Method 3 was tested without accounting for the effects of the coaxial probe feed. Method 4 was tested without taking coaxial feed effects into account and by taking the effects into account using group delay peak shifted to be at f_0 using $CavW$ and adjusting coaxial probe location ($CoaxOffset$) by ratio of $\frac{CavW_{new}}{CavW_{old}}$. Method 5 was tested without taking coaxial feed effects into account and with

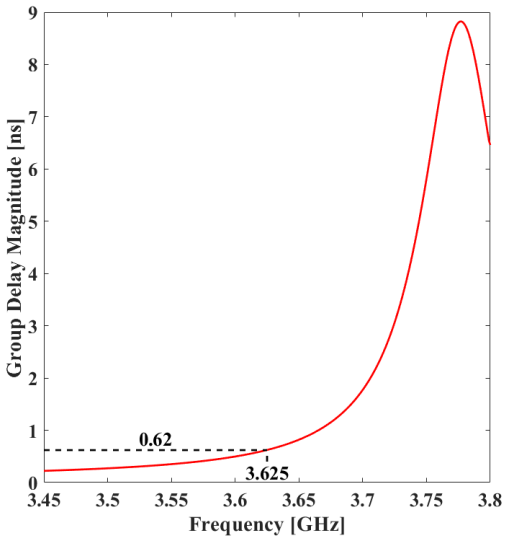

Figure 4.8: Group delay of initial coaxial probe feed

them accounted for, using a peak group delay shifted by $CavW$ to occur at f_0, and keeping the coaxial probe location ($CenterDistance$) at a consistent distance from the center of the cavity.

4.4 Method Comparisons

- Method 1: Filter group delay is extracted at f_0 without shifting peak using $CavW$
  - Method 1.1: Coaxial probe effects were not calculated
  - Method 1.2: Coaxial probes effects were calculated by peak group delay centered at f_0 using $CavW$
- Method 2: Filter group delay is extracted at f_0 after shifting group delay peak using $CavW$
  - Method 2.1: Coaxial probe effects were not calculated

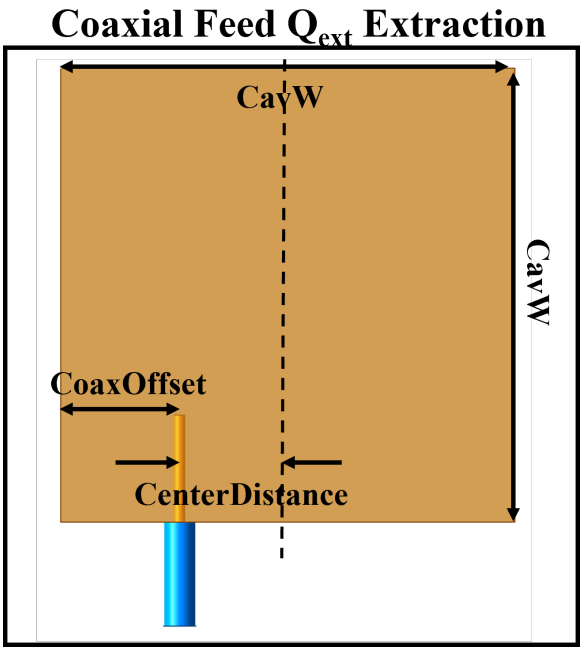

Figure 4.9: Diagram of the coaxial feed Q_{ext} extraction

  - Method 2.2: Coaxial probes effects were calculated by peak group delay centered at f_0 using $CavW$

- Method 3: Filter group delay is extracted at f_{peak} and horn is matched to that group delay at f_{peak}

  - Method 3.1: Coaxial probe effects were not calculated

- Method 4: Filter group delay is extracted at f_0 after shifting group delay peak using $CavW$ and then adjusting coax position by $\frac{CavW_{new}}{CavW_{old}}$

  - Method 4.1: Coaxial probe effects were not calculated

  - Method 4.2: Coaxial probes effects were calculated by peak group delay centered at f_0 using $CavW$ and then adjusting coax position by $\frac{CavW_{new}}{CavW_{old}}$

- Method 5: Filter group delay is extracted at f_0 after shifting group delay peak using $CavW$ and coaxial $CenterDistance$ is kept consistent

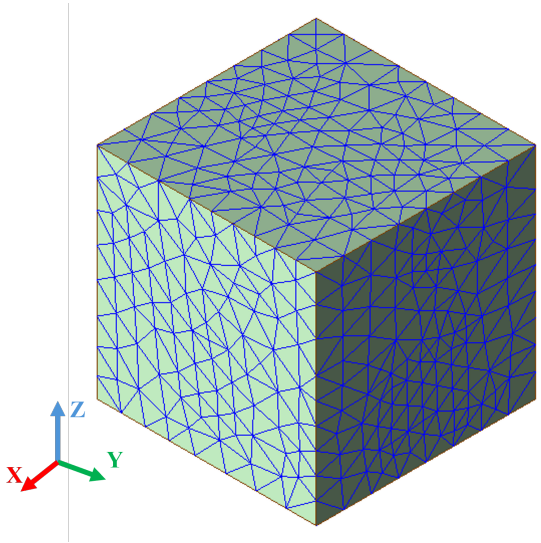

Figure 4.10: Example of the mesh of a cavity filter

- Method 5.1: Coaxial probe effects were not calculated
- Method 5.2: Coaxial probes effects were calculated by peak group delay centered at f_0 using $CavW$ and coaxial $CenterDistance$ is kept consistent

The matching methods were compared by analyzing the time-domain responses of the filter/horns relative to the tuned filter without the horn, to better understand the behavior of each iris and cavity. The structures were simulated using Ansys HFSS, a mesh-based solver. This means the structure is meshed for field analysis, with a tighter mesh yielding more accurate results but taking longer. The default mesh settings are based on the solution frequency. It is generally advisable to set this to the highest frequency in the band, as the mesh size is based on the wavelength at that frequency. The field analysis varies with mesh size, so it is necessary to mesh as finely as time allows. It was found that setting the same solution frequency yields the best match between the horn and filter simulations. It was set to the top of the filter band, 3.8 GHz, for the matching case comparisons, and to 6 GHz for the final matching between the different horns and the filter, as well as for the conical horn matched to the fifth-order filter. An example of the cavity mesh is shown in Fig. 4.10.

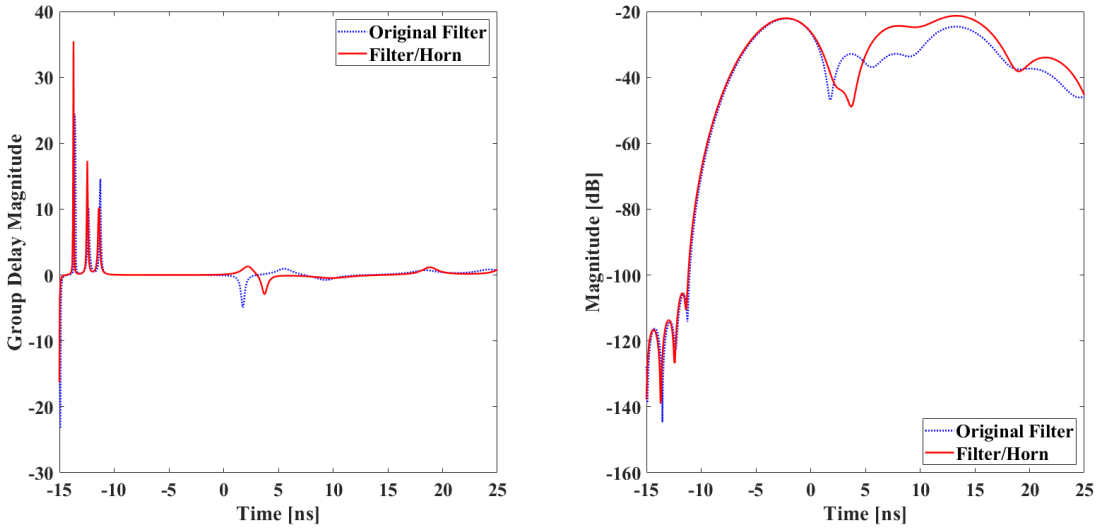

(a) **(b)**

Figure 4.11: The (a) group delay magnitude, and (b) the magnitude of the time-domain response for the matching using Method 1.1 of a conical horn antenna to a third-order filter.

Fig. 4.11 shows the time-domain group delay magnitude and the time-domain magnitude of the filter/horn matched using Method 1.1 compared to that of the original third-order filter. It can be seen in Fig. 4.11a that the resonant frequencies of the first two cavities differ from the original filter. In Fig. 4.11b, it can be seen that Q_{ext1} is tuned well but that the $k_{1,2}$ is over-coupled. The rest of the couplings appear to be close to what they need to be. It is important to remember, however, that detuning in preceding cavities affects later cavities, but the full time-domain response still provides some insight into the tuning of the filter/horn relative to the original filter.

Fig. 4.12 shows the time-domain group delay magnitude and the time-domain magnitude of the filter/horn matched using Method 1.2 compared to that of the original third-order filter. Fig. 4.12a shows that the first and second resonator sizes are again detuned. It can also be seen in Fig. 4.12b that $k_{1,2}$ is so strongly coupled that the hump of the coupling almost completely disappears. $k_{2,3}$ appears to be under-coupled based upon the location of the null representing the third cavity.

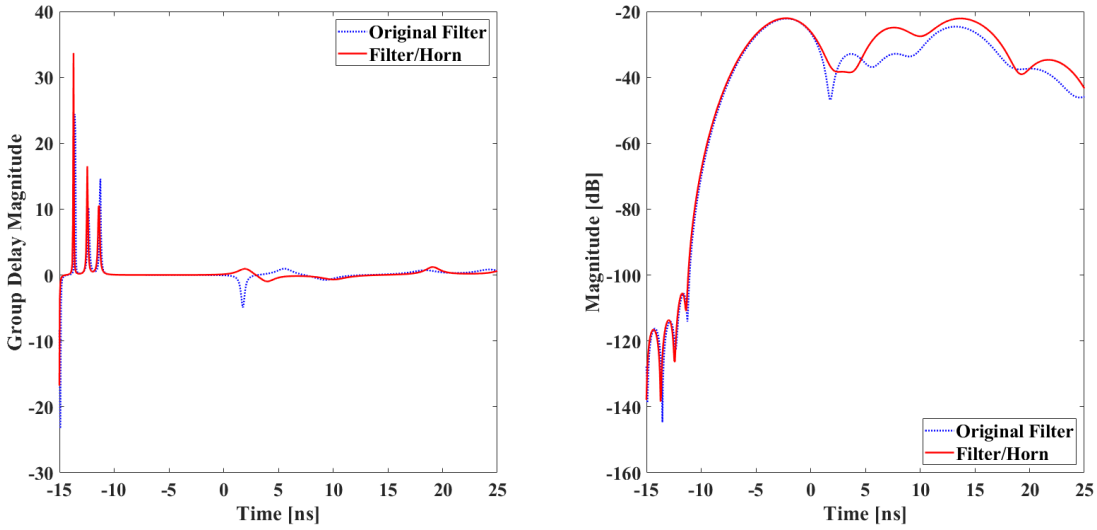

(a) **(b)**

Figure 4.12: The (a) group delay magnitude, and (b) the magnitude of the time-domain response for the matching using Method 1.2 of a conical horn antenna to a third-order filter.

Fig. 4.13 shows the time-domain group delay magnitude and the time-domain magnitude of the filter/horn matched using Method 2.1 compared to that of the original third-order filter. It can be seen in Fig. 4.13a that the first and second resonator frequencies are detuned, and the third resonator is detuned enough that the resonance is not even visible in the group delay plot. Fig. 4.13b shows that $k_{1,2}$ is extremely over-coupled and $k_{2,3}$ appears under-coupled.

Fig. 4.14 shows the time-domain response of the conical horn antenna matched to the third-order filter using matching method 2.2. Fig. 4.14a demonstrates that the first and second resonators are detuned. Fig. 4.14b shows that Q_{ext1} is tuned but $k_{1,2}$ is over-coupled and $k_{2,3}$ is slightly under-coupled.

Fig. 4.15 shows the time-domain response of the conical horn antenna matched to the third-order filter using matching method 3.1. Fig. 4.15a shows that all three resonances are de-tuned in frequency and Fig. 4.15b shows that all couplings aside from Q_{ext1} are de-tuned. Given how detuned the resonances are, it is unclear in which direction the couplings are detuned.

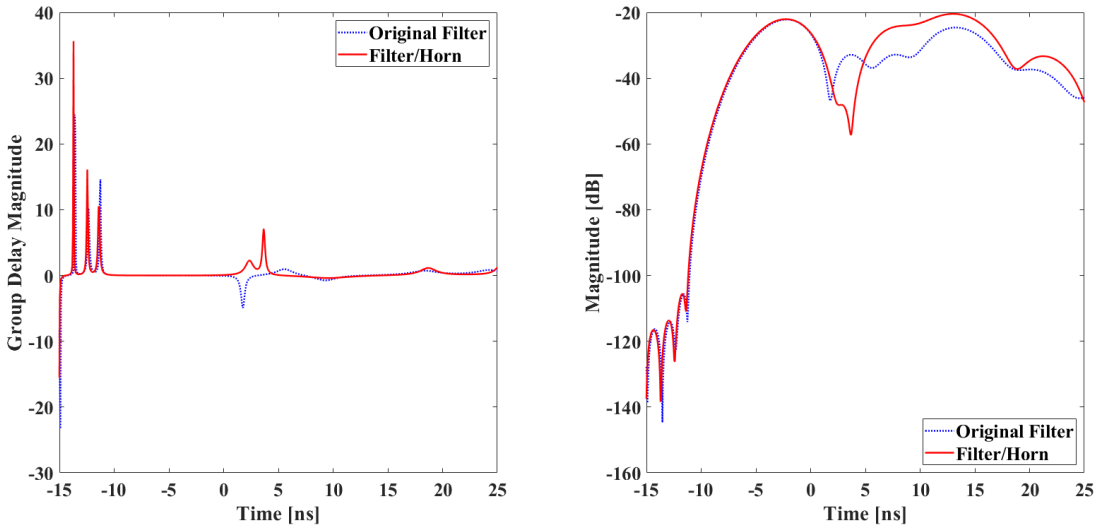

(a) **(b)**

Figure 4.13: The (a) group delay magnitude, and (b) the magnitude of the time-domain response for the matching using Method 2.1 of a conical horn antenna to a third-order filter.

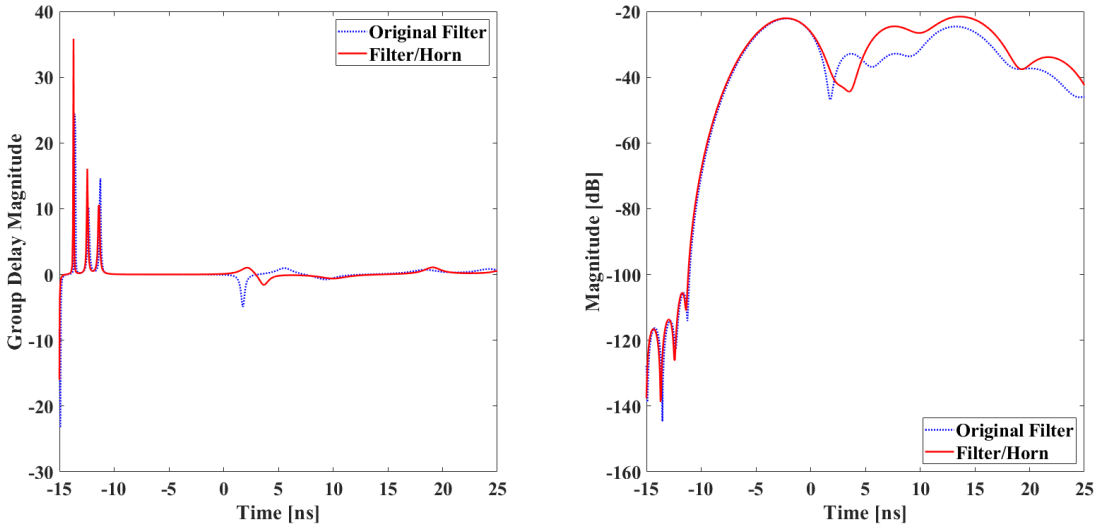

(a) **(b)**

Figure 4.14: The (a) group delay magnitude, and (b) the magnitude of the time-domain response for the matching using Method 2.2 of a conical horn antenna to a third-order filter.

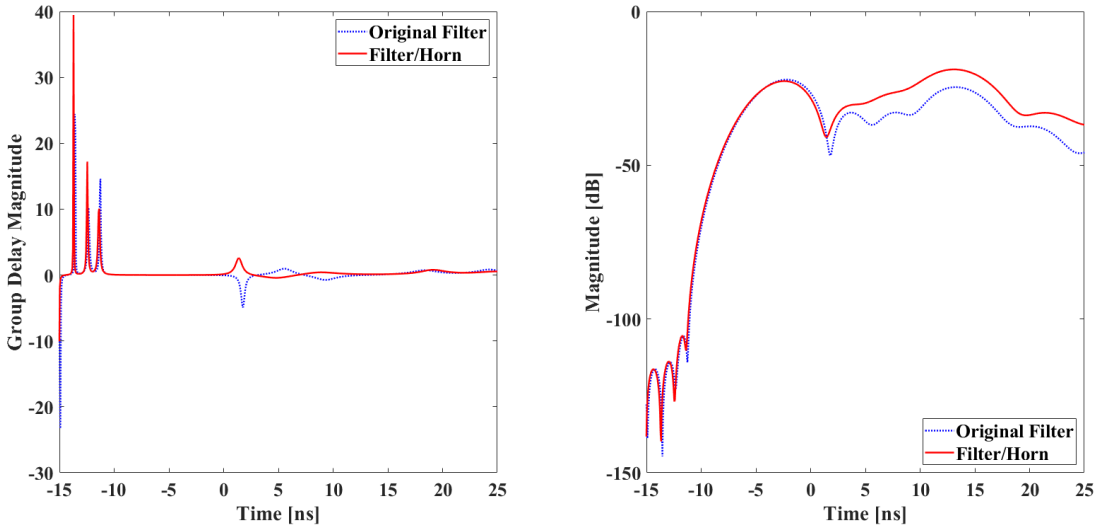

(a) **(b)**

Figure 4.15: The (a) group delay magnitude, and (b) the magnitude of the time-domain response for the matching using Method 3.1 of a conical horn antenna to a third-order filter.

Fig. 4.16 shows the time-domain response of the conical horn antenna matched to the third-order filter using matching method 4.1. All of the resonances are well tuned with the exception of the first, as seen in Fig. 4.16a. However, Fig. 4.16b shows that Q_{ext1} is too high. $k_{1,2}$ and $k_{2,3}$ are off as well although that could be due to Q_{ext1} being de-tuned.

Fig. 4.17 shows the time-domain response of the conical horn matched to the third-order filter using Method 4.2. The group delay magnitude, seen in Fig. 4.17a, shows that the first and second resonators are detuned. It can be seen in Fig. 4.17b that Q_{ext1} is well tuned and $k_{1,2}$ is over-coupled.

Fig. 4.18 shows the time-domain response of the conical horn matched to the third-order cavity filter using method 5.1. As shown in Fig. 4.18a, the resonances are all tuned close to those of the original filter. It can be seen in Fig. 4.18b that Q_{ext1} matches the original filter well. $k_{1,2}$ is over-coupled, but the humps representing $k_{2,3}$ and Q_{ext2} appear to end at roughly the same points in time as the original filter.

The time-domain response for the conical horn matched to the third-order filter is seen

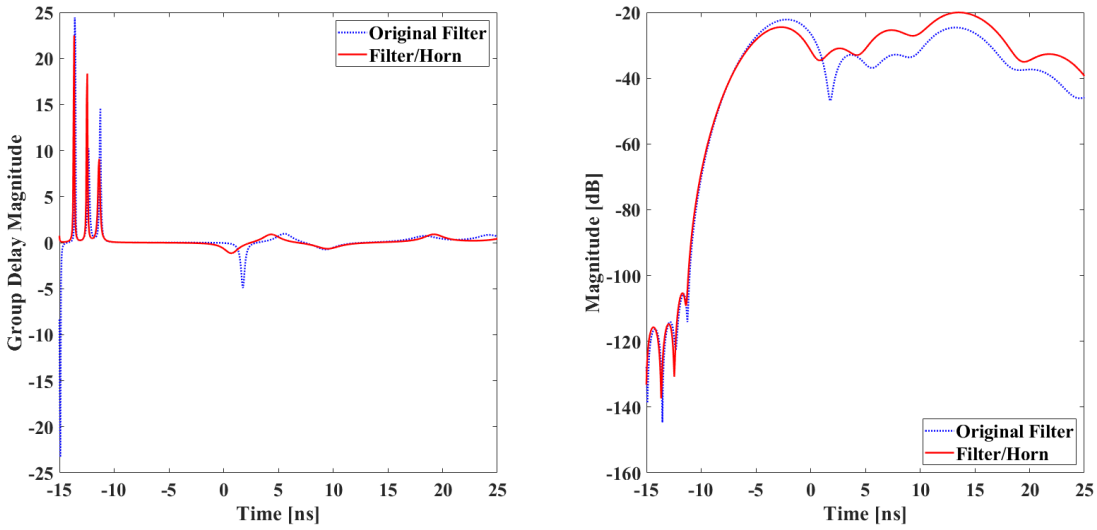

(a) **(b)**

Figure 4.16: The (a) group delay magnitude, and (b) the magnitude of the time-domain response for the matching using Method 4.1 of a conical horn antenna to a third-order filter.

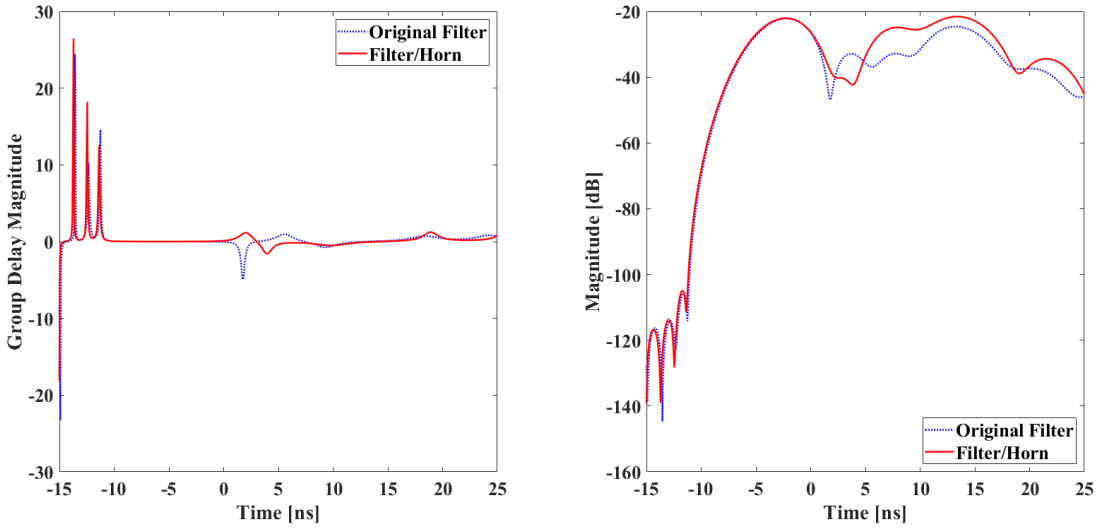

(a) **(b)**

Figure 4.17: The (a) group delay magnitude, and (b) the magnitude of the time-domain response for the matching using Method 4.2 of a conical horn antenna to a third-order filter.

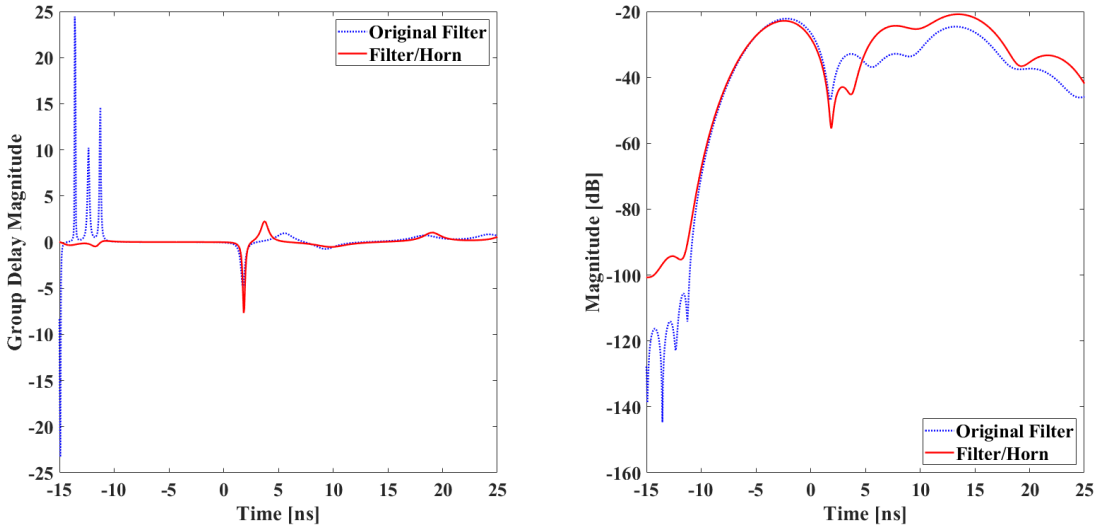

(a) **(b)**

Figure 4.18: The (a) group delay magnitude, and (b) the magnitude of the time-domain response for the matching using Method 5.1 of a conical horn antenna to a third-order filter.

in Fig. 4.19. It can be seen in Fig. 4.19a that the first and second resonators are detuned, and in Fig. 4.19b it can be seen that $k_{1,2}$ and $k_{2,3}$ are detuned.

Looking at the time-domain plots for all matching methods, the coaxial de-embedding method did not yield significantly improved results and is complicated and iterative. The lack of improvement in matching with coaxial de-embedding is because, as shown in Fig. 4.8, the coaxial feed of the cavity-fed iris-coupled horn simulation was designed in such a way that the group delay of the response is much higher in frequency than f_0 and is outside of the filter band of interest. It would then be expected that the coaxial probe would not have a significant impact on the overall Q_{ext} of the cavity-fed iris-coupled horn simulation when the group delay is analyzed at f_0. The Q_{ext} extracted using Q_{rad} in [32] also does not calculate the effects of the feed and still achieves solid filtenna synthesis.

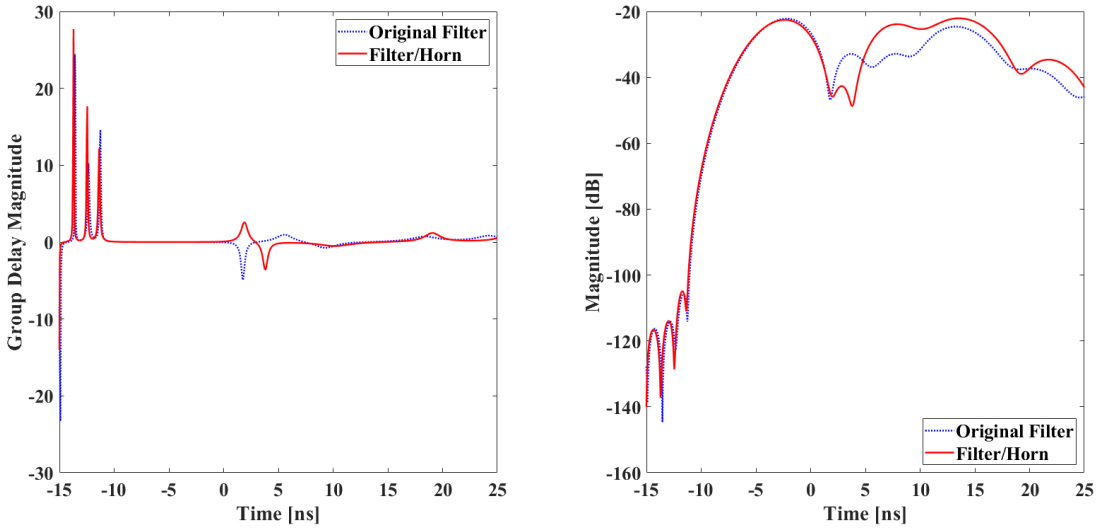

(a) **(b)**

Figure 4.19: The (a) group delay magnitude, and (b) the magnitude of the time-domain response for the matching using Method 5.2 of a conical horn antenna to a third-order filter.

4.5 Varying Horns

The method that gave the most satisfactory results was Method 5.1, as the first resonator is well matched and all subsequent resonances are identifiable in the time-domain response. The couplings were fairly well-tuned aside from $k_{1,2}$, which was detuned for all methods.

Method 5.1 was then applied to match the corrugated horn and pyramidal horn designed in the previous chapter to the third-order Chebyshev filter, to test its replicability and versatility across different dual-polarized horn antennas. The method was applied to matching the conical horn antenna, the corrugated conical horn antenna, and the pyramidal horn antenna to the third-order filter. Even with the solution frequency set to the same value across all simulations, the large size differences between the horns led to uneven meshing among filters/horns, making comparisons difficult. Therefore, a mesh operation was forced to define exactly the mesh size in the filter structure. The mesh length in the slots was set to 1.5 mm, and the mesh inside the cavities was set to 10 mm. The filter simulated with this updated

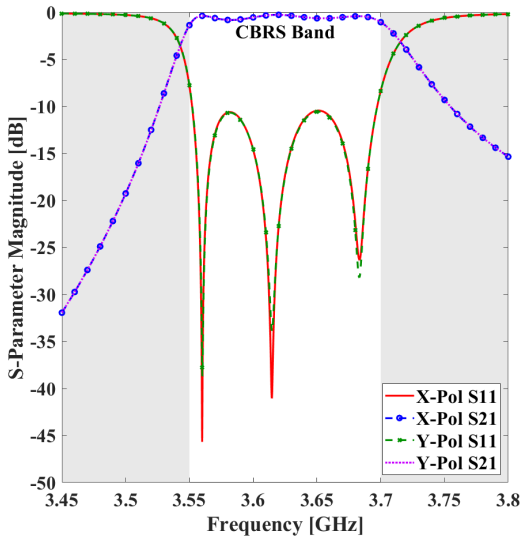

Figure 4.20: Final tuned third-order filter response simulated with a solution frequency of 6 GHz and set mesh length

mesh is shown in Fig. 4.20.

The initial match for the conical horn coupled to the third-order filter can be seen in Fig. 4.21a, and the frequency domain filter response can be seen in Fig. 4.21b. The time-domain group delay and magnitude responses are shown in Fig. 4.21c and 4.21d, respectively. All three resonances are visible in the frequency response and occur at approximately the same location as the original filter resonances. The average return loss ripple is 4.55 dB lower for the filter/horn, and the bandwidth is narrower by 0.006 GHz. Looking at the time-domain group-delay response, the resonators appear to be approximately tuned to the proper frequency. However, it can be seen in the time-domain magnitude that while the Q_{ext} appears to be tuned, $k_{1,2}$ appear over-coupled.

The initial match for the corrugated conical horn matched to the third-order filter can be seen in Fig. 4.22a. The frequency-domain filter response is shown in Fig. 4.22b, and it can be seen that all three resonances are visible in the frequency response and occur at approximately the same location as the original filter resonances. The average return loss ripple is 4.24 dB lower, and the bandwidth of the filter/horn is 0.0074 GHz narrower than

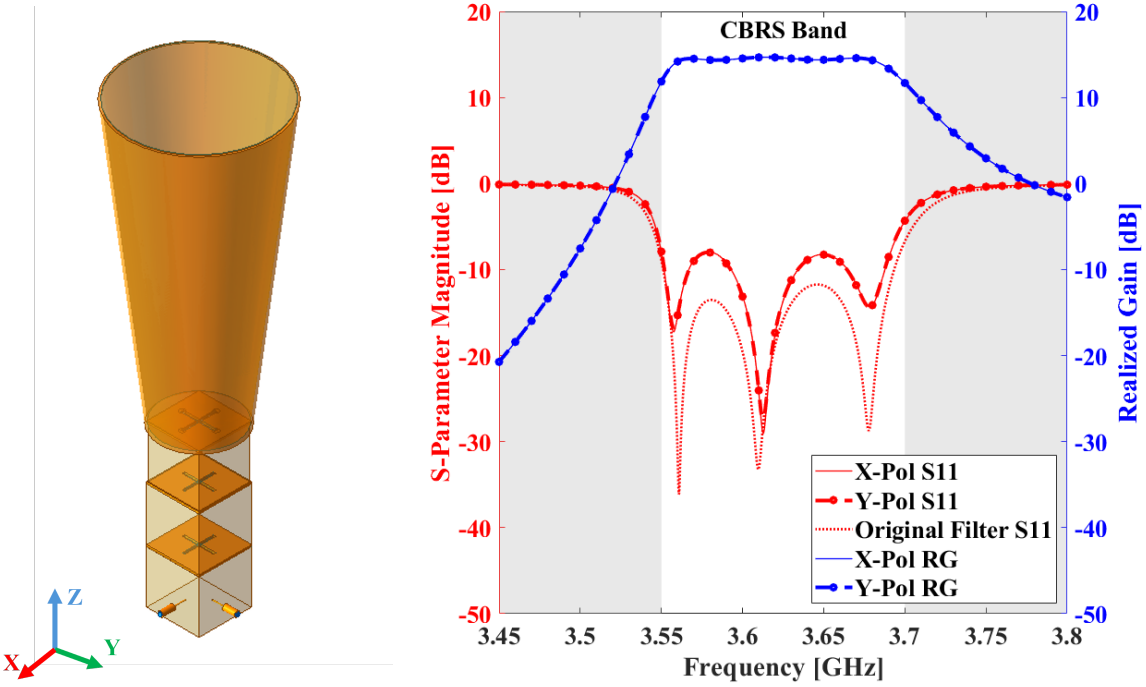

(a) (b)

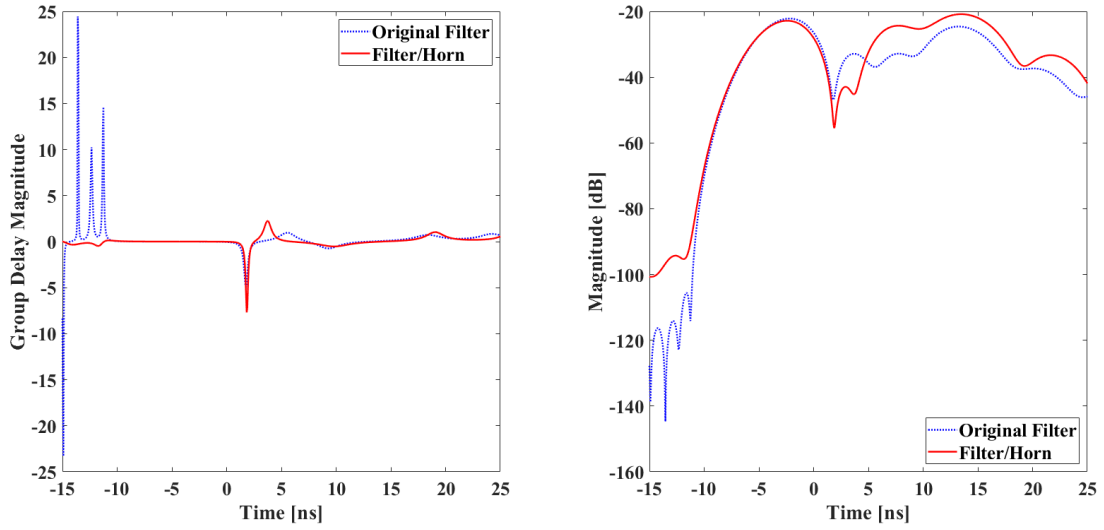

(c) (d)

Figure 4.21: The (a) conical horn coupled to the third-order filter with a cross-slot iris, (b) frequency-domain filter response, (c) time-domain group delay magnitude, and (d) time-domain magnitude of a dual-polarized, conical horn antenna directly attached to a third-order filter using a singly-polarized matching method

that of the original filter. The time-domain group delay magnitude is shown in Fig. 4.22c, and it can be seen that the resonator frequencies are tuned close to those of the original filter. Fig. 4.22d shows that the coupling is well-tuned aside from $k_{1,2}$ being over-coupled.

The initial match for the pyramidal horn coupled to the third-order filter can be seen in Fig. 4.23a. The frequency-domain filter response is shown in Fig. 4.23b, and it can be seen that all three resonances are visible in the frequency response and occur at approximately the same location as the original filter resonances. The average return loss ripple is 5.13 dB lower than that of the original filter, and the bandwidth of the filter/horn is 0.0087 GHz narrower. The time-domain group delay magnitude is shown in Fig. 4.23c. It can be seen that the first and second resonators' resonant frequencies differ from those of the original filter. Fig. 4.23d shows that Q_{ext1} is lower than the original filter and $k_{1,2}$ is over-coupled.

The method was similarly successful across all three horns it was tested with. The proposed matching method yields a much closer match than simply attaching any horn to the cavity filter. Some time-domain tuning will be required to replicate the original filter response exactly, but the starting point for that tuning has been greatly improved.

4.6 Varying Filters

It was then necessary to determine if this method is applicable to any cavity resonator filter. The conical horn antenna was matched to the fifth-order filter using the method proposed. The conical horn coupled to the fifth-order filter can be seen in Fig. 4.24a and the frequency-domain filter response can be seen in Fig. 4.24b. It can be seen that all five nulls in the return loss are present in the filter/horn and occur at approximately the same frequencies as those of the original filter. However, the average return loss ripple is 9.97 dB lower than that of the original filter. The bandwidth of the filter/horn is 0.0042 GHz wider than the original fifth-order filter. The time-domain group delay magnitude is shown in Fig. 4.24c. The first

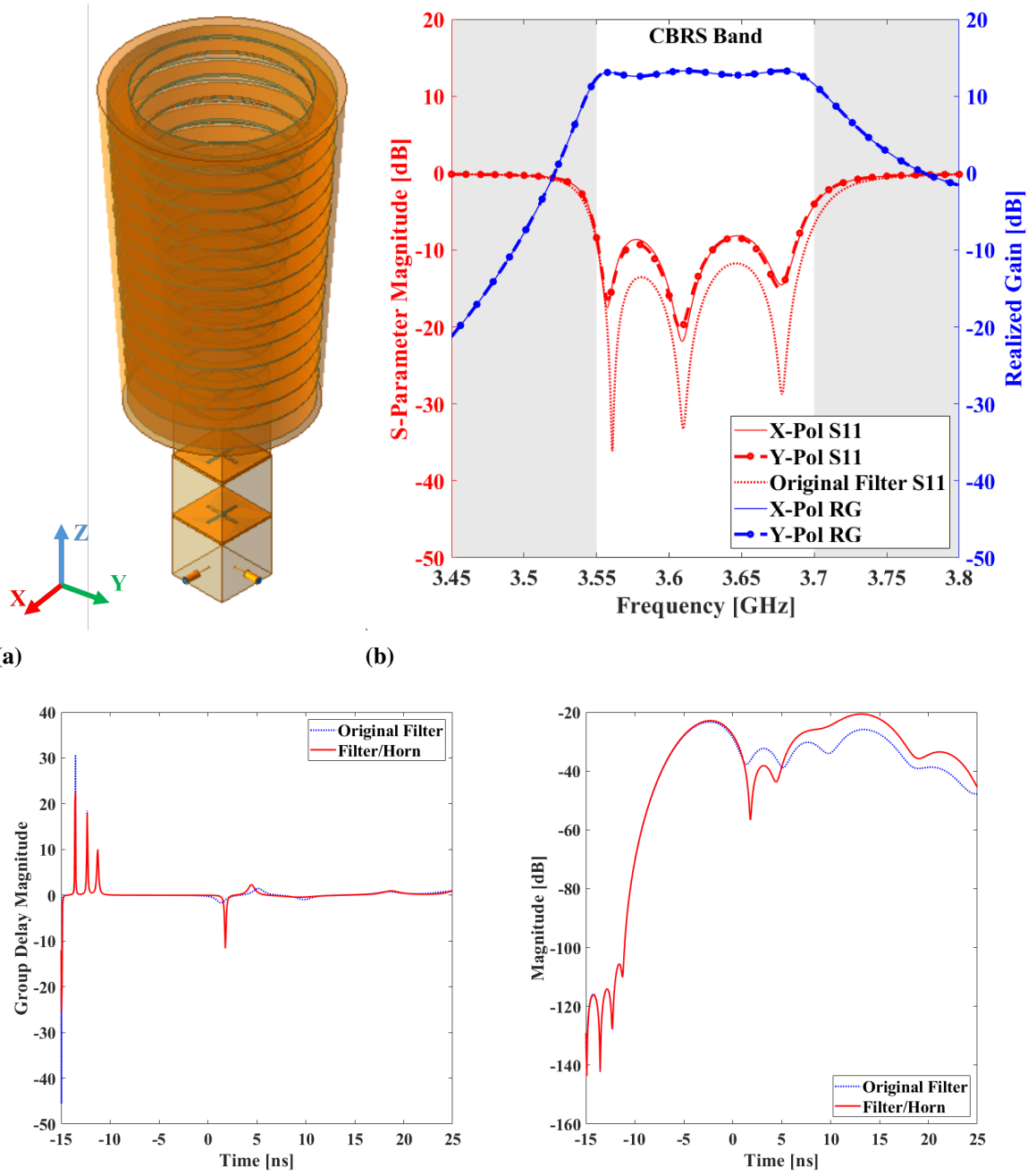

Figure 4.22: The (a) corrugated conical horn attached to the third-order filter with a cross-slot iris, (b) frequency-domain filter response, (c) time-domain group delay magnitude, and (d) time-domain magnitude of a dual-polarized, corrugated, conical horn antenna directly attached to a third-order filter using a singly-polarized matching method

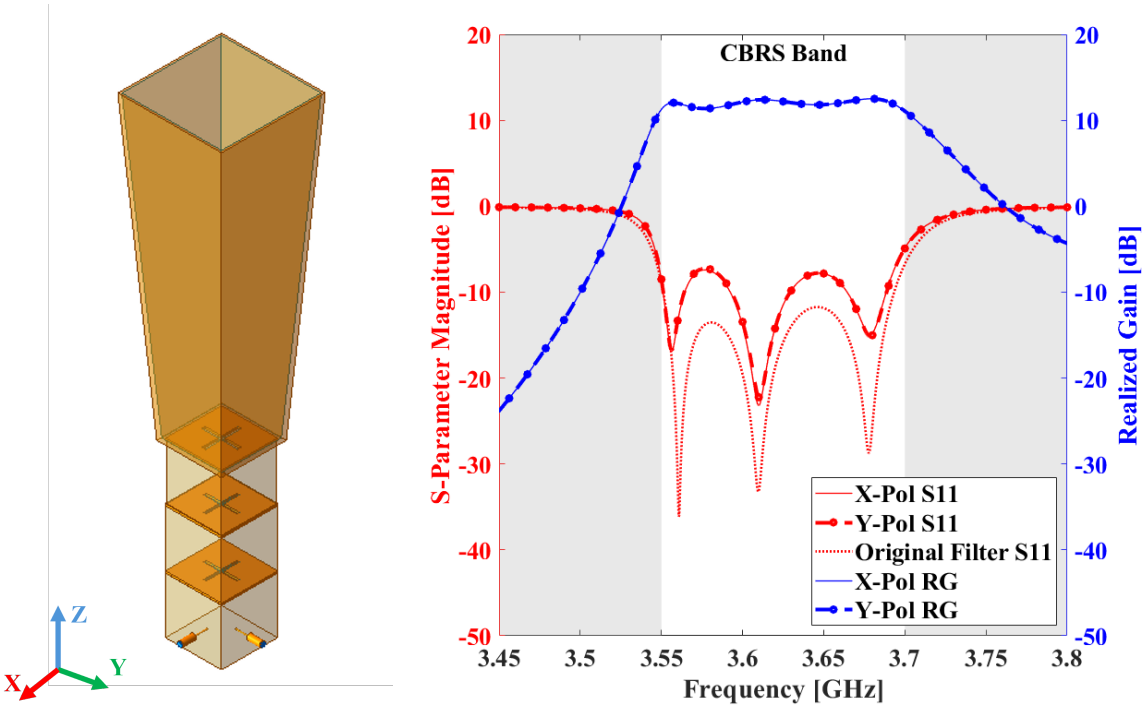

Figure 4.23: The (a) pyramidal horn attached to the third-order filter with a cross-slot iris, (b) frequency-domain filter response, (c) time-domain group delay magnitude, and (d) time-domain magnitude of a dual-polarized, pyramidal horn antenna directly attached to a third-order filter using a singly-polarized matching method

and second resonators are well-tuned, and the third resonator is slightly higher in frequency than that of the original filter. The fourth and fifth resonators have become so detuned that they are largely invisible in the group delay magnitude. The time-domain magnitude can be seen in Fig. 4.24d. Q_{ext1} and $k_{1,2}$ couplings match the original filter exactly, but the rest of the couplings are almost indistinguishable, likely due to the resonances being very detuned. The matching method provides a strong starting point for further tuning of the fifth-order filter, which is coupled directly to the conical horn.

4.7 Dual-Polarized Considerations

Up until now, the Q_{ext} values were extracted from simulations operating with a single polarization because the isolation between the polarizations was expected to be low based on the isolation demonstrated by the filter with this same square cavity and cross-slot iris topology. The isolation between the filter polarizations is shown in Fig. 4.25. The isolation is 15 dB or greater throughout the filter bandwidth. However, even the small cross-polarization coupling could affect the values for Q_{ext} of the filter and horn antenna, so this section investigates how the matching success changes when the Q_{ext} is extracted from dual-polarized simulations. The second coaxial probe also has a loading effect on the Q_{ext} of the tuned filter, which should be accounted for to give the most accurate Q_{ext} to match to. Method 5.1 remains the matching method used in the dual-polarized investigations.

The Q_{ext} presented by the third- and fifth-order filters was extracted using the single cavity structure. However, the dual-coaxial feed structure was simulated rather than the single-coaxial probe feed utilized earlier. This dual-fed structure is shown in Fig. 4.26a. The cavity-fed iris-coupled horn simulation used to extract the Q_{ext} of the horn antenna was also simulated with the dual-coaxial feed as shown in Fig. 4.26b.

The values for Q_{ext} for the third-order filter were then extracted from group delay as

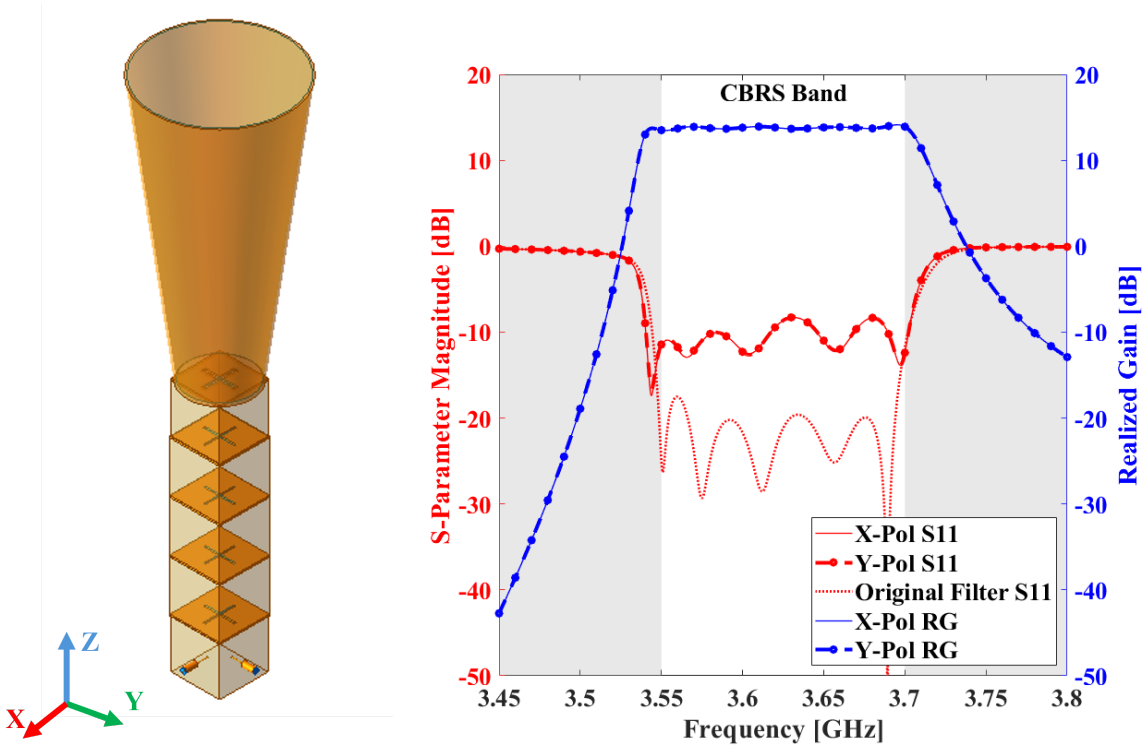

Figure 4.24: The (a) conical horn attached to the fifth order filter with a cross-slot iris, (b) frequency-domain filter response, (c) time-domain group delay magnitude, and (d) time-domain magnitude of a dual-polarized, conical horn antenna directly attached to a third order filter using a singly-polarized matching method

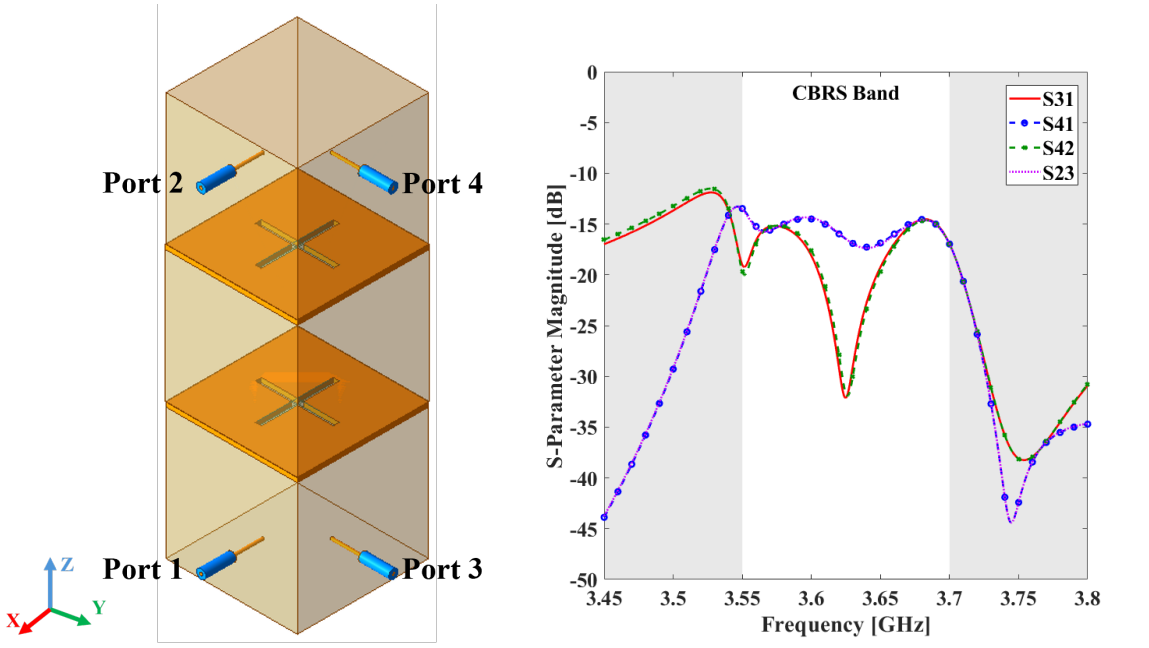

(a) (b)

Figure 4.25: The third-order filter (a) image with the ports labeled, and (b) the isolation between ports demonstrated by scattering parameters

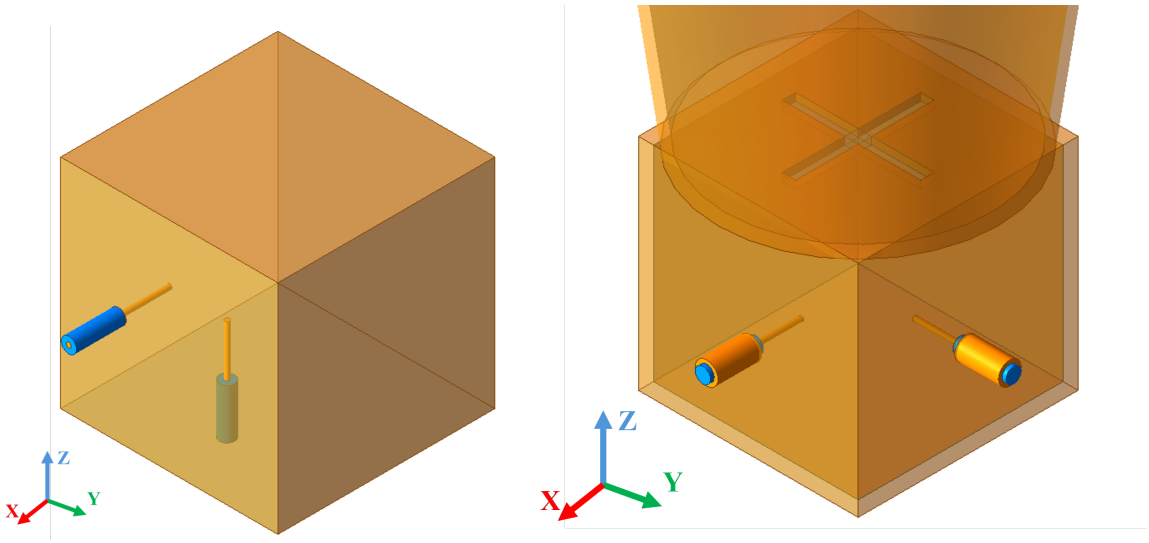

(a) (b)

Figure 4.26: The dual-fed (a) single cavity, and (b) cavity-fed iris-coupled horn

detailed for Method 5.1. The Q_{ext} for the tuned third-order filter extracted with the single feed was 26.76, and the Q_{ext} extracted with the dual feed was 30.29. While these values are not vastly different, the difference is large enough to be expected to affect the success of the match for the final cascaded filter/horn. Therefore, the Q_{ext} for all three horn antennas was matched to that of the dual-fed tuned filter Q_{ext} to determine how well the dual-polarized matching performs. The performance of dual-polarized matching was also investigated for the conical horn coupled to the fifth-order filter.

The frequency response of the initial match for the conical horn antenna coupled to the third-order filter using the dual-polarized matching method is shown in Fig. 4.27b. The cascaded conical filter/horn has a bandwidth that is 0.0113 GHz narrower than that of the original filter and an average return-loss ripple that is 2.16 dB lower. The average return-loss ripple for the dual-polarized matching method is closer to the original filter than that of the single-polarized matching method, but the bandwidth of the dual-polarized case differs more from the original filter than the single-polarized method. However, the time-domain plots show significant improvement over the single-polarized match. The time-domain group delay, shown in Fig. 4.27c, shows that the first two resonances of the cascaded filter/horn are resonant at almost the same frequencies as those of the original filter. The third resonance differs in frequency from the original filter, likely due to the loading effects of the iris between the filter and the horn. The time-domain magnitude, shown in Fig. 4.27d, indicates that Q_{ext1} closely matches that of the original filter. $k_{1,2}$ differs slightly from that of the original filter, and $k_{2,3}$ differs more from the original filter, likely due to the frequency of the third resonator differing in frequency. The hump representing Q_{ext2} appears to still end at the proper point in time, but the magnitude of the hump differs from that of the original filter.

The frequency response of the initial match for the corrugated conical horn antenna coupled to the third-order filter using the dual-polarized matching method is shown in Fig.

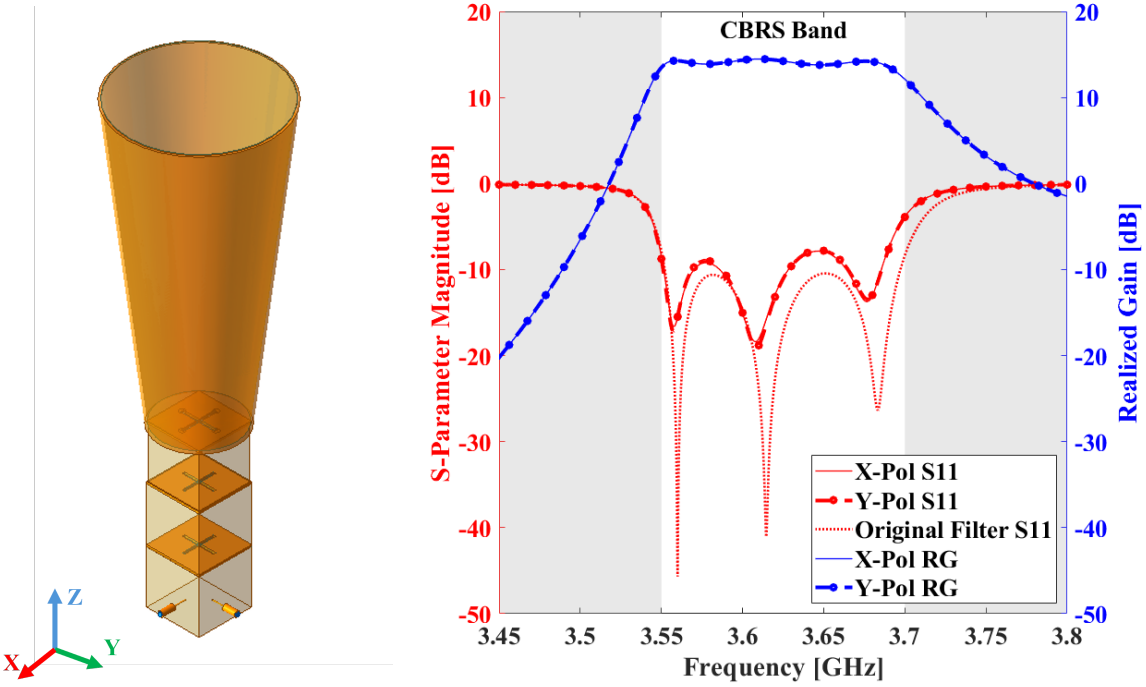

(a) (b)

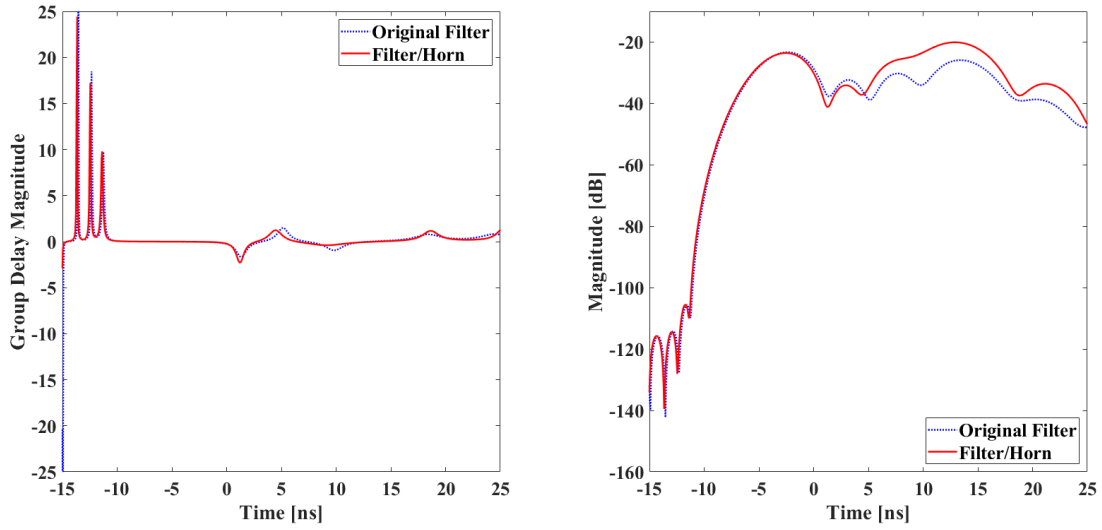

(c) (d)

Figure 4.27: The (a) conical horn coupled to the third-order filter with a cross-slot iris, (b) frequency-domain filter response, (c) time-domain group delay magnitude, and (d) time-domain magnitude of a dual-polarized, conical horn antenna directly attached to a third-order filter using a dual-polarized matching method

4.28b. The cascaded corrugated filter/horn has a bandwidth that is 0.0084 GHz narrower than that of the original filter and an average return-loss ripple that is 3.61 dB lower. The average return-loss ripple for the dual-polarized matching method is closer to the original filter than that of the single-polarized matching method, but the bandwidth of the dual-polarized case differs slightly more from the original filter than the single-polarized method. However, the time-domain plots show significant improvement over the single-polarized match. The time-domain group delay, shown in Fig. 4.28c, shows that the first resonance of the cascaded filter/horn is resonant at almost the same frequency as that of the original filter. The second resonance differs slightly in frequency from that of the original filter. The third resonance differs in frequency from the original filter more, likely due to the loading effects of the iris between the filter and the horn. The time-domain magnitude, shown in Fig. 4.28d, indicates that Q_{ext1} and $k_{1,2}$ closely matches those of the original filter. The $k_{2,3}$ of the filter/horn differs from the original filter, likely due to the frequency of the third resonator differing in frequency. The hump representing Q_{ext2} appears to end slightly later in time, and the magnitude of the hump differs from that of the original filter.

The frequency response of the initial match for the pyramidal horn antenna coupled to the third-order filter using the dual-polarized matching method is shown in Fig. 4.29b. The cascaded pyramidal filter/horn has a bandwidth that is 0.0042 GHz wider than that of the original filter and an average return-loss ripple that is 5.17 dB lower. The average return-loss ripple difference for the dual-polarized matching method is about the same as that of the single-polarized match. The time-domain plots show similar results to the single-polarized match for the pyramidal filter/horn. The time-domain group delay, shown in Fig. 4.29c, shows that all three resonances differ slightly from the original filter, with the third resonance being almost indistinguishable. The time-domain magnitude, shown in Fig. 4.29d, indicates that Q_{ext1} nearly matches that of the original filter, but $k_{1,2}$ is overcoupled when compared to the original filter. The $k_{2,3}$ of the filter/horn differs from the original filter, likely due to

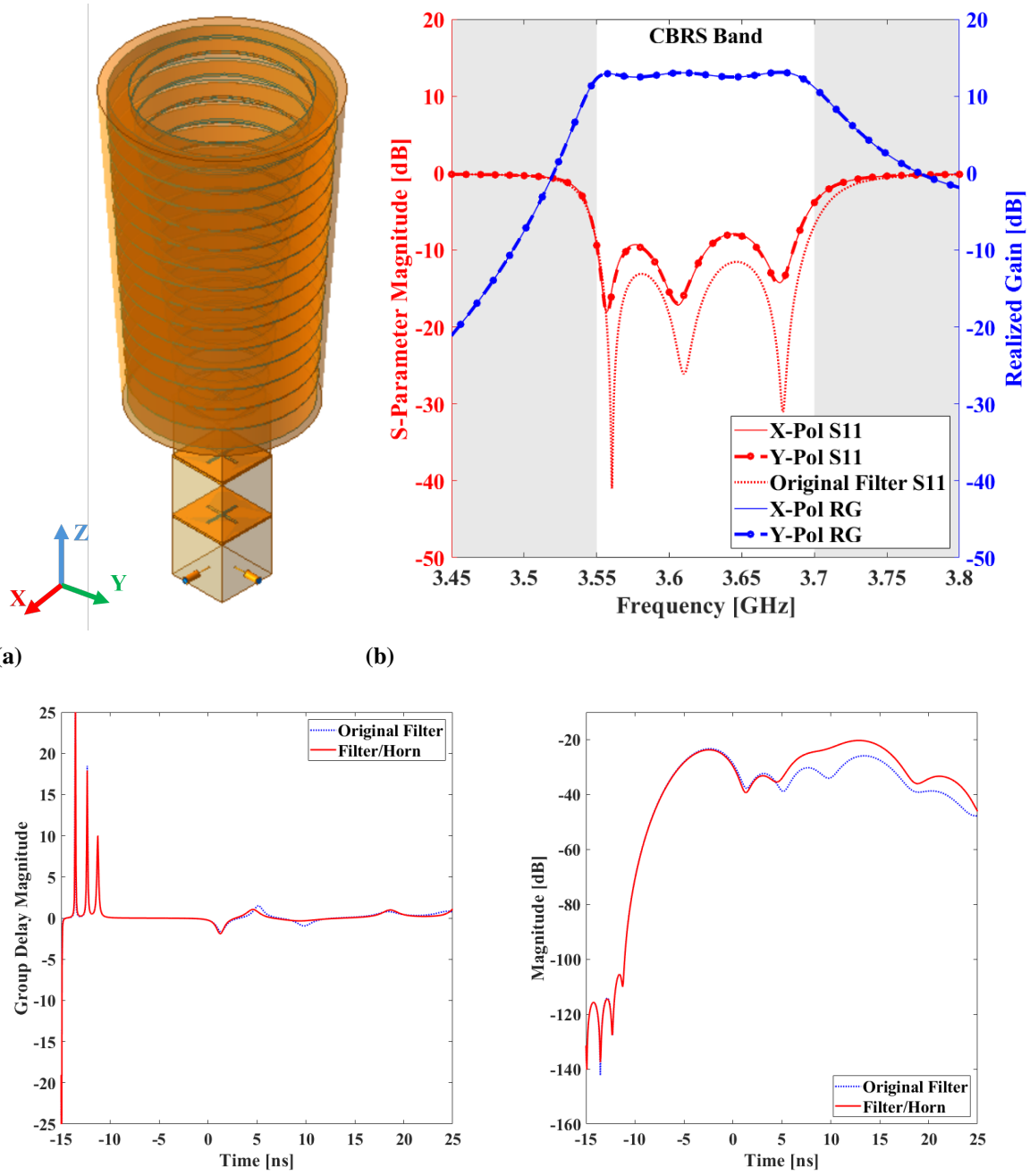

Figure 4.28: The (a) corrugated horn coupled to the third-order filter with a cross-slot iris, (b) frequency-domain filter response, (c) time-domain group delay magnitude, and (d) time-domain magnitude of a dual-polarized, corrugated horn antenna directly attached to a third-order filter using a dual-polarized matching method

the frequency of the third resonator differing in frequency. The hump representing Q_{ext2} appears to end slightly later in time, and the magnitude of the hump differs from that of the original filter.

The frequency response of the initial match for the conical horn antenna coupled to the fifth-order filter using the dual-polarized matching method is shown in Fig. 4.30b. The cascaded conical filter/horn has a bandwidth that is 0.0047 GHz wider than that of the original filter and an average return-loss ripple that is 9.96 dB lower. The average return-loss ripple difference between the filter/horn and the original filter for the dual-polarized matching method is similar to that of the single-polarized matching method. The bandwidth widening of the dual-polarized case differs only 0.0005 GHz from the bandwidth widening of the single-polarized case more, and the time-domain plots show similar performance to the single-polarized match. The time-domain group delay, shown in Fig.4.30c, shows that the first two resonances of the cascaded filter/horn are resonant at almost the same frequencies as those of the original filter. The rest of the resonance differs in frequency from the original filter, likely due to the loading effects of the iris between the filter and the horn. The time-domain magnitude, shown in Fig. 4.30d, indicates that Q_{ext1} and $k_{1,2}$ closely matches that of the original filter. The inter-resonator couplings $k_{2,3}$, $k_{3,4}$, $k_{4,5}$, and Q_{ext2} are largely indistinguishable in the time-domain magnitude response.

4.8 Tuned Conical Horn Cascaded with the Third-Order Filter

The conical horn cascaded with the third-order filter was fine-tuned slightly using the time-domain tuning method described in Chapter 2. The tuned frequency response of the third-order conical filtering horn can be seen in Fig. 4.31a, and the radiation patterns for both the x- and y-polarized feeds can be seen in Figs. 4.31b and 4.31c, respectively. The tuned filter/horn was tuned to a fractional bandwidth of 3.47% with an average realized gain

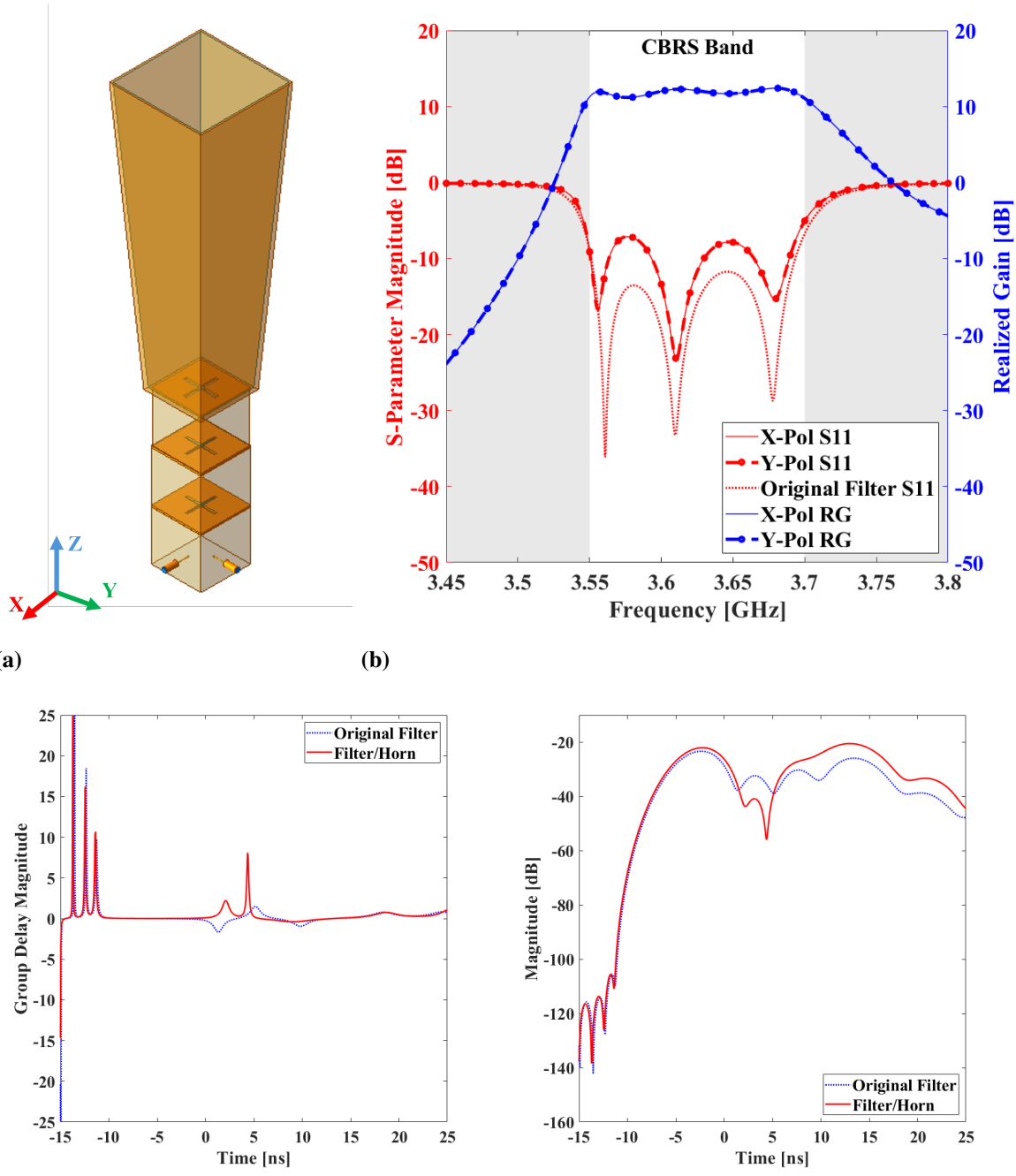

Figure 4.29: The (a) pyramidal horn coupled to the third-order filter with a cross-slot iris, (b) frequency-domain filter response, (c) time-domain group delay magnitude, and (d) time-domain magnitude of a dual-polarized, pyramidal horn antenna directly attached to a third-order filter using a dual-polarized matching method

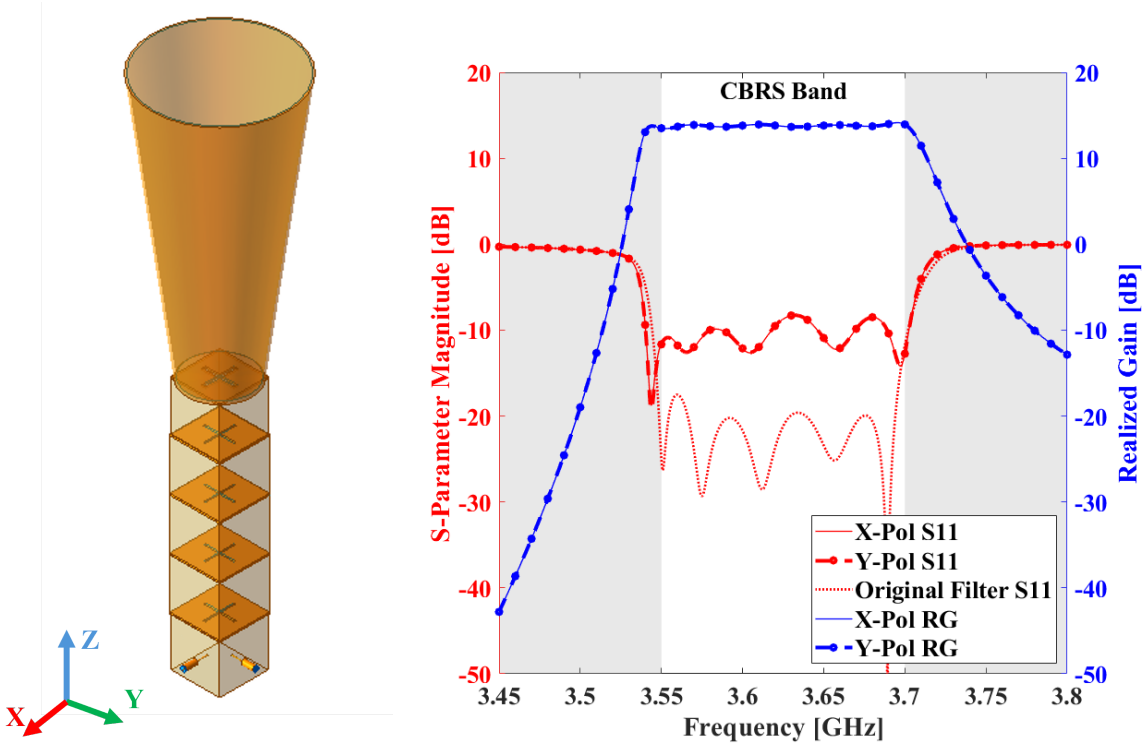

Figure 4.30: The (a) conical horn coupled to the fifth-order filter with a cross-slot iris, (b) frequency-domain filter response, (c) time-domain group delay magnitude, and (d) time-domain magnitude of a dual-polarized, conical horn antenna directly attached to a fifth-order filter using a dual-polarized matching method

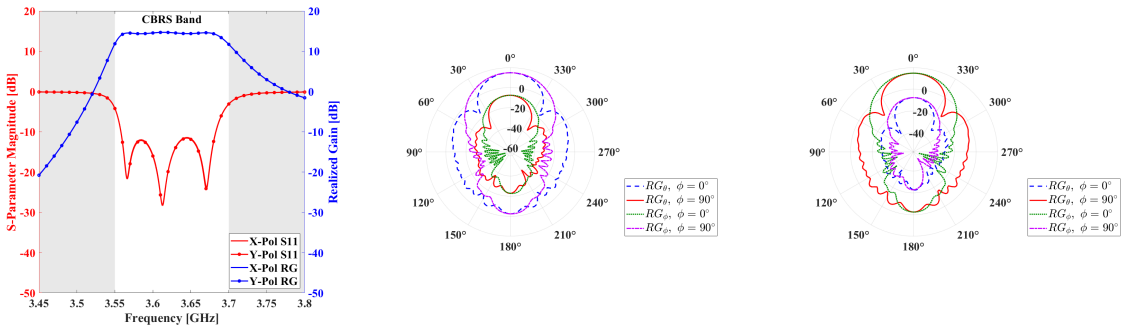

(a) **(b)** **(c)**

Figure 4.31: The (a) frequency response, (b) radiation patterns for the x-polarized feed, and (c) radiation patterns for the y-polarized feed are shown

ripple of 0.33 dB in the passband.

One important factor in designing filtering antenna systems is the group delay introduced by the filter/horn. The group delay through a filter is also known as the envelope delay [41]. A flat group-delay response within the passband is ideal because it reduces distortion of the transmitted signal [41]. The envelope delay of a filter would traditionally be calculated from the transmission coefficient of the two-port filter system, as [41]

$$\tau_d = -\frac{d\phi_{21}}{d\omega} s \tag{4.2}$$

where τ_d is the envelop delay and ϕ_{21} is the phase of the transmission coefficient, S_{21}. However, a cascaded filter/horn topology does not follow a traditional two-port system design, as the second port is replaced with the horn antenna. The three-antenna group delay method can be adapted to calculate the transmitted group delay of a horn antenna using two identical horn antennas transmitting to each other at boresight [53] [54]. This allows the extraction of the envelope delay of the cascaded filter/horn designed in this work. The group delay of a single filter/horn is calculated from

$$\tau_e = \frac{\tau_{total} - \frac{d}{c}}{2} \tag{4.3}$$

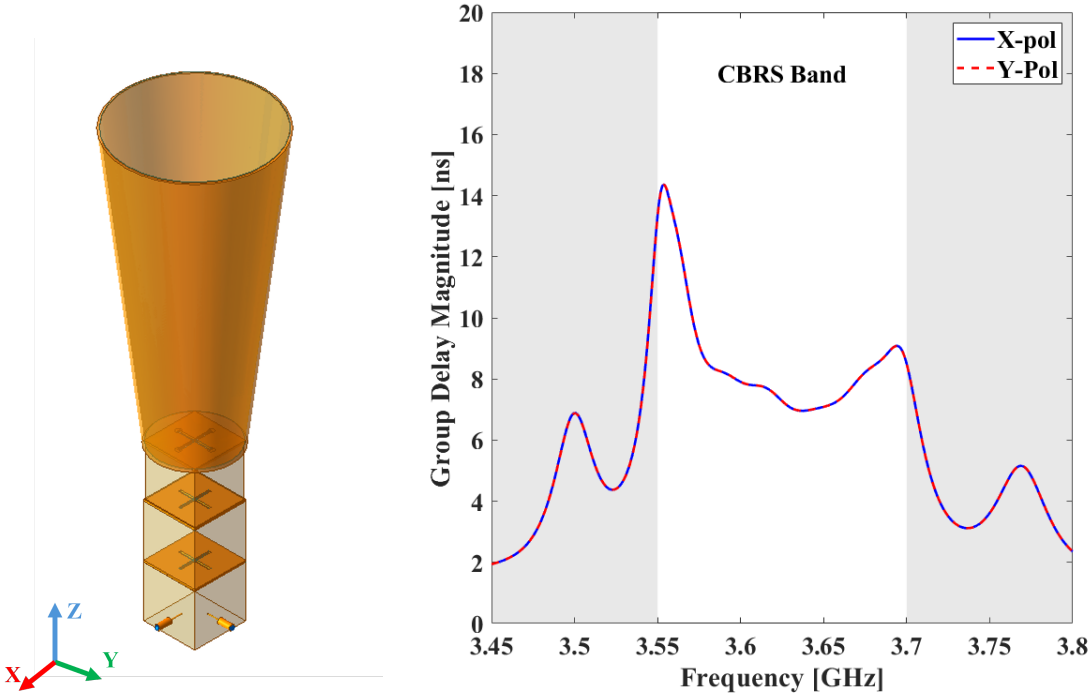

(a) **(b)**

Figure 4.32: The (a) tuned conical horn directly cascaded with the third-order filter, and (b) transmitted group delay for both x- and y-polarizations

where τ_e is the envelop group delay of a single filter/horn, τ_{total} is the full group delay between the transmit at one antenna and the receive at the other, d is the distance between the two identical filter/horns, and c is the speed of light approximately equal to $3 \cdot 10^8$. The two horns need to be a sufficient distance apart to be in each other's far-field region. The minimum distance for far-field operation is calculated as $d = \frac{2D^2}{\lambda}$ where D is the diameter of the horn aperture and λ is the wavelength at the highest frequency of the sweep.

The group delay for the tuned conical filter/horn is shown in Fig. 4.32b. Within the filter's pass band, it varies between 6.96 ns and 14.36 ns. This significant variance could lead to signal distortion, which must be accounted for when processing signals received from the cascaded filter/horn.

4.9 Conclusion

Various methods were tested for extracting the Q_{ext} of a conical horn antenna and matching it to a third-order cavity filter. The most successful method was then applied to match a conical horn, a corrugated conical horn, and a pyramidal horn, thereby validating the method for different types of horn antennas. A conical horn was then matched to a fifth-order cavity filter with a different ripple to assess the matching method's performance across different filter orders. The proposed synthesis method successfully matched the third-order filter to multiple horns. The matching method achieved a solid match for the conical horn to the fifth-order filter. The fifth-order filter/horn has a lower average return loss ripple than the original filter, but all nulls occur in approximately the same location as the original filter, and the bandwidth of the filter/horn is only 0.0042 GHz wider than the original filter. Comparing the third-order matching cases and the fifth-order matching case, the issue likely lies in the extraction of the Q_{ext} of the tuned filter to which the horn is then matched. The loading of the rest of the cavities/irises of the filter on the coaxial feed is not accounted for when simulating a single, coaxial-fed cavity for Q_{ext} extraction. This loading factor increases as the number of cavities and irises scales with the filter order. However, the matching method still provides a much better starting point for the filter's final tuning than simply attaching the horn to the filter.

Then, it was investigated how the matching method simulated with dual-polarized structures compared to the matching method using singly-polarized structures. The time-domain response showed that the initial match using the dual-polarized method for the conical and corrugated horn coupled to the third-order filter gave a closer match to the original filter than the single-polarized matching method. The matching for the pyramidal horn coupled to the third-order filter and the conical horn coupled to the fifth-order filter did not show any significant changes between the single- and dual-polarized methods.

Finally, the conical horn coupled to the third-order filter was tuned in the time domain. The radiation patterns and filter response were shown. The group delay through the filter/horn was also investigated to understand how the cascaded filtering horn affects the transmitted group delay, since group-delay variance within the passband will distort the signal.

Chapter 5

Coupling Screw Mode Polarizer

The idea of using the cavity's orthonormal modes to create a dual-mode, dual-channel filter capable of exciting a circularly polarized pyramidal horn antenna was explored. This would allow for easier deployment to remote locations by requiring only a single feed structure to the circularly polarized filter/horn. Mode polarizers have been well-studied, and there are many existing methods for mode polarization, such as septum polarizers [55], iris polarizers [56], corrugated polarizers [57], ridge polarizers [58], and post polarizers [59]. However, these mode polarizers require two separate feeds or a single feed oriented at 45° to the two orthogonal modes. Dual-mode filter theory was introduced by [60] in 1948 and proposes that a capacitive screw inserted at 45° induces equal coupling between existing orthonormal modes in a square/circular cavity. The length of the screw affects the amount of coupling between the modes. This idea has been applied to the design of compact RF filters, as the use of orthogonal degenerate modes reduces the number of cavities needed by a factor of two compared to single-mode resonators [61], which is shown in Fig. 5.1. Screws inserted into waveguides are also used to tune wave impedance by introducing capacitance or inductance, thereby introducing phase shifts [60]. The goal was to leverage the dual-mode operation of filters to equally excite both modes in a dual-channel filter and reduce the filter size by half. The careful design of the screw inserted would introduce a phase shift, leading to the generation of a dual-mode, dual-channel filter that outputs a circularly polarized wave to be

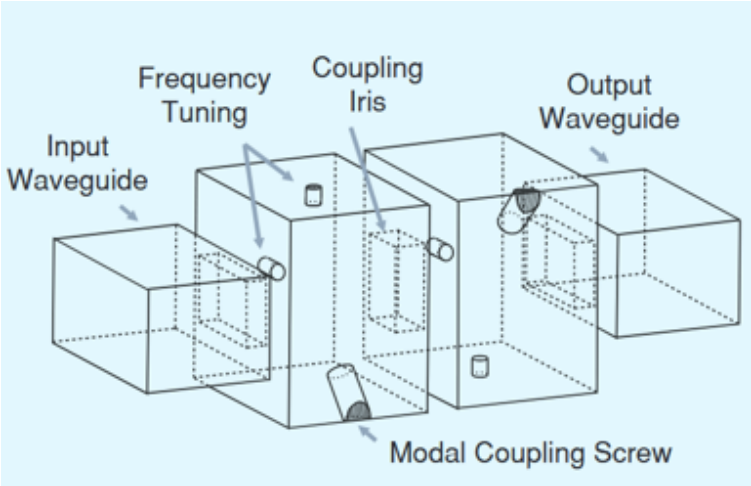

Figure 5.1: Example of the implementation of modal coupling screws in a dual-mode cavity filter

radiated by the pyramidal horn antenna.

5.1 45° Coupling Screw as Mode Polarizer

The ability of a single coupling screw to be used as a mode polarizer in a square cavity was investigated. The cavity was excited using a coaxial probe feed, and a screw was introduced at a 45° angle to the coaxial probe, as shown in Fig. 5.2a. The simulation structure used for this analysis can be seen in Fig. 5.2b. The screw position is set to $\frac{\lambda}{2}$ as that corresponds to the peak in the magnetic field of the waveguide, seen in Fig. 5.3, inducing maximum induced current on the coupling screw. Circular polarization is achieved when orthogonal polarizations have equal magnitude and a phase difference of 90° [43].

The magnitude of the two polarizations produced by the coupling screw was found from the transmission scattering parameter, S_{21}, for the TE_{10} and TE_{01} modes and the absolute phase difference between the two modes is $\phi_\Delta = |\phi_{TE01} - \phi_{TE10}|$ where ϕ_{TE01} and ϕ_{TE10} are the unwrapped phase for the modes defined in Fig. 5.2b. The screw length was varied to determine the resulting phase shift. The results can be seen in Fig. 5.4. It was found that the phase difference between polarizations can be tuned with different screw lengths, and that a

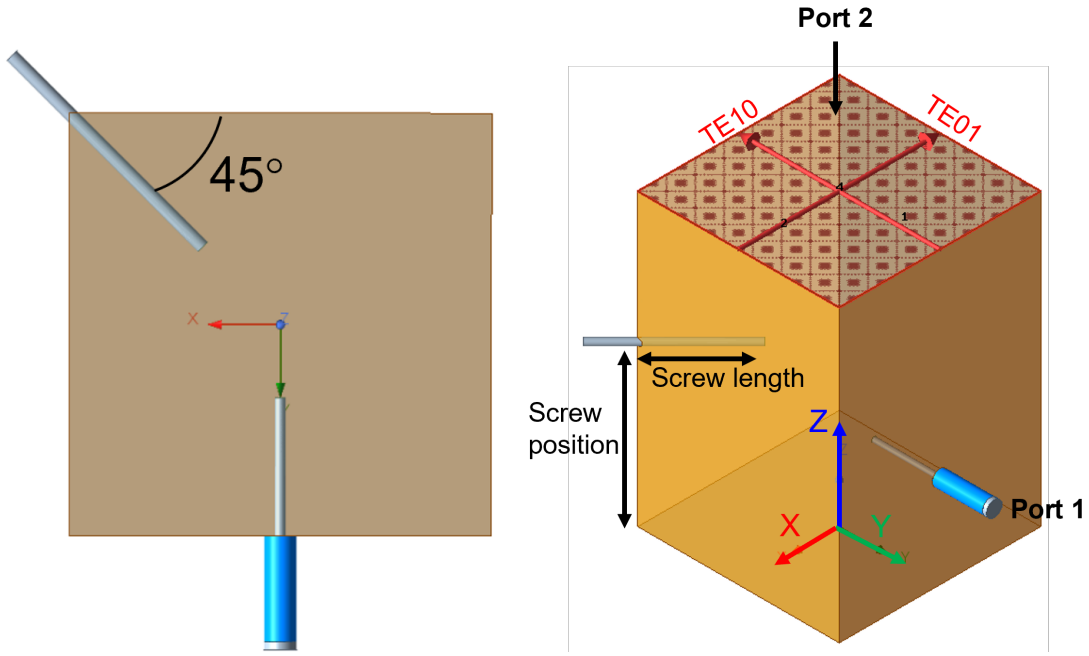

(a) **(b)**

Figure 5.2: The (a) top view, and (b) isometric view of the coaxial probe-fed waveguide with a coupling screw inserted at 45°

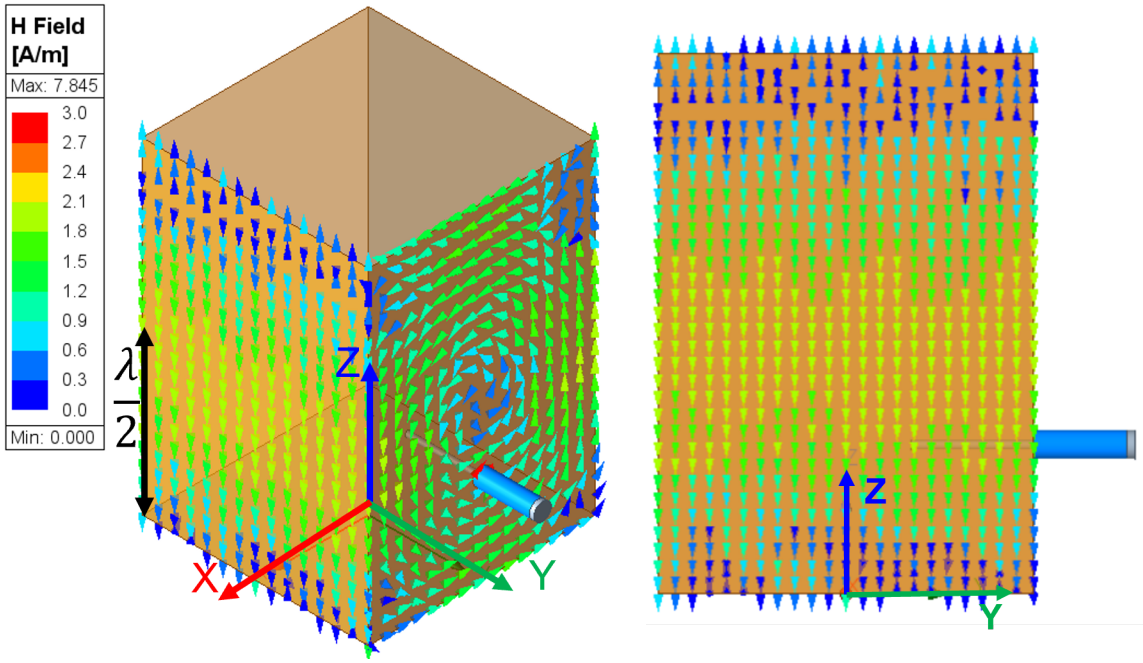

(a) **(b)**

Figure 5.3: The (a) isometric view, and (b) side view of the magnetic fields in the coaxial probe-fed waveguide

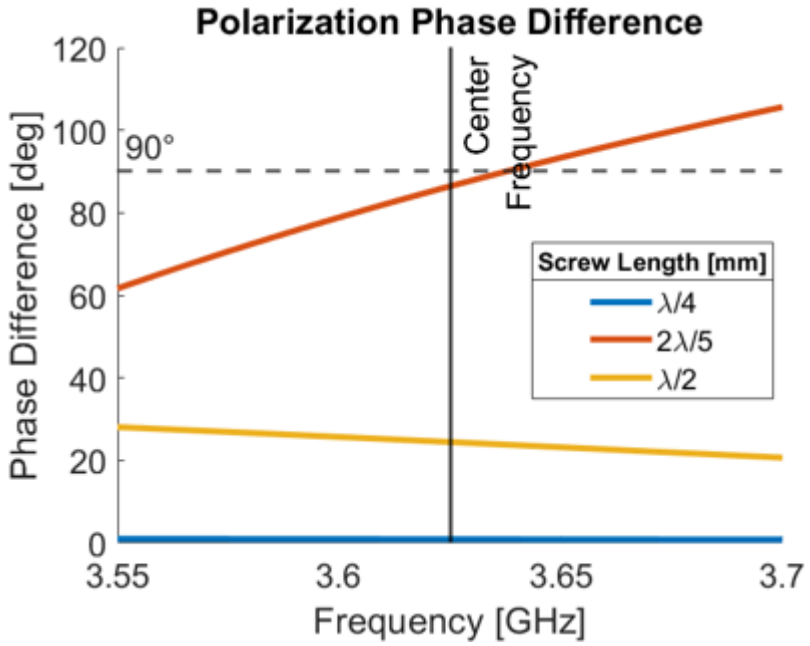

Figure 5.4: Plot of phase difference across frequency as coupling screw length varies

$90°$ phase shift between polarizations is also possible.

Screw length was then varied to achieve a $90°$ phase difference between polarizations seen in Fig. 5.5a. Screw position was also varied within about 5 millimeters around $\frac{\lambda}{2}$. It was found that at a phase difference of $90°$, the magnitudes of the two polarizations were not equal. It was expected that if all power is transferred, power will be split equally, and the S_{21} magnitude should be around -3 dB for both polarizations. It can be seen in Fig. 5.5b that this did not occur when the screw was tuned to give a $90°$ phase shift. It can be seen in Fig. 5.6 that the power is equally split between the two polarizations when the phase difference is $180°$. As there is only one tuning mechanism, it is impossible to achieve both a $90°$ phase shift and equal power coupled between modes with a single tuning screw using a traveling wave structure.

The waveguide was then used to feed a pyramidal horn antenna. It was found that through designing the waveguide to operate close to cutoff, the wave impedance can be kept sufficiently high to induce a cavity-like mode in the waveguide. The waveguide

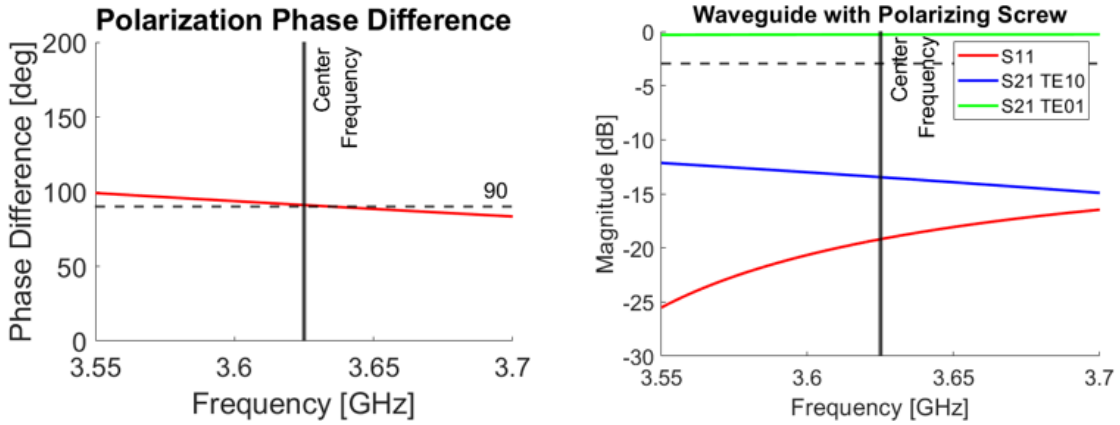

(a) **(b)**

Figure 5.5: The (a) phase difference, and (b) magnitude of the orthogonal polarizations with a $90°$ phase difference in a coaxial probe-fed waveguide with a coupling screw inserted at $45°$

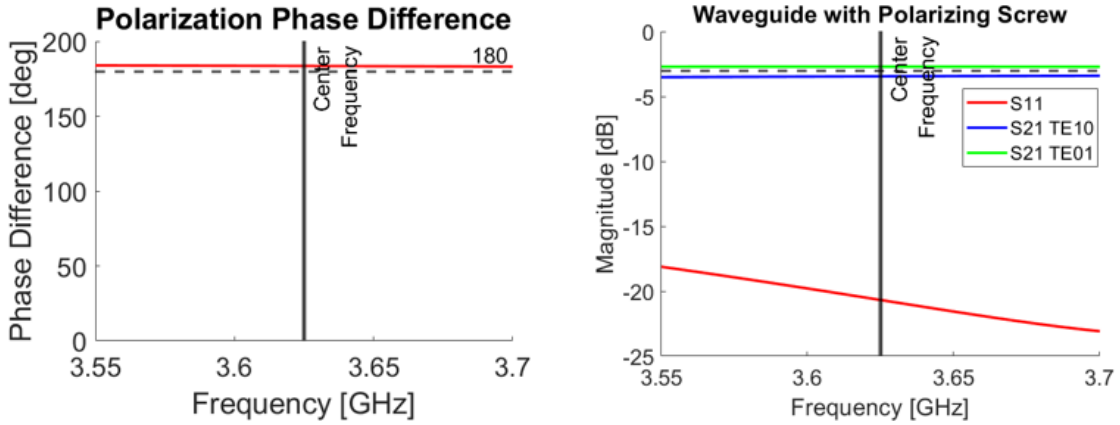

(a) **(b)**

Figure 5.6: The (a) phase difference, and (b) magnitude of the orthogonal polarizations with equal magnitudes in a coaxial probe-fed waveguide with a coupling screw inserted at $45°$

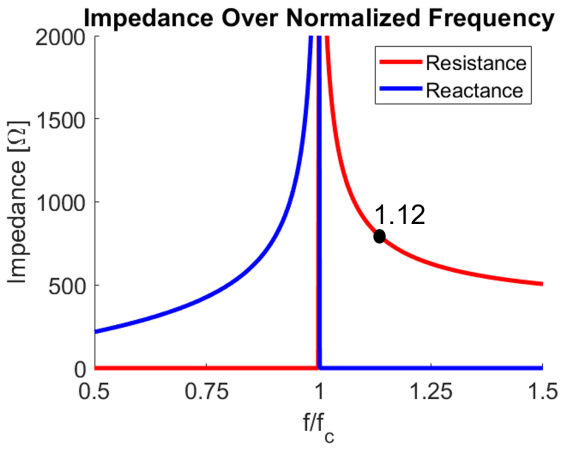

Figure 5.7: Wave impedance plot versus frequency normalized by f_0

operating frequency was set to occur right on the curve following the asymptote at cutoff at a normalized operating frequency of 1.12, which can be seen in Fig. 5.7. Utilizing this cavity mode, circular polarization can be achieved in the waveguide as the feed between the horn and the waveguide acts as an iris, and the coupling screw induces a phase shift, giving two separate mechanisms acting on the fields. The horn and feed structure can be seen in Fig. 5.8a and the field distribution can be seen in Fig. 5.8b.

Circular polarization is seen in the 31.64 dB separation in the main beam between right-hand circularly polarized and left-hand circularly polarized realized gain plotted in Fig. 5.9a. This separation indicates that the power is adequately converted to one polarization. There would be much less separation between RHCP and LHCP if the polarization were elliptical. An example of the realized gain of an elliptically polarized horn can be seen in Fig. 5.9b. The separation between LHCP and RHCP was 9.76 dB. It was designed with the coupling screw polarizer as well, but with a waveguide designed much farther from cutoff. Another method for analyzing circular polarization is the axial ratio. An axial ratio of one indicates circular polarization. The axial ratio of the circularly polarized horn is shown in Fig. 5.10a. It varies around 1 by about 0.5 from $\theta = -50$ to $\theta = 50$ and varies by about 0.8 around 1 within the CBRS band, being right at about 1 at f_0. It can be seen in Fig.5.10b

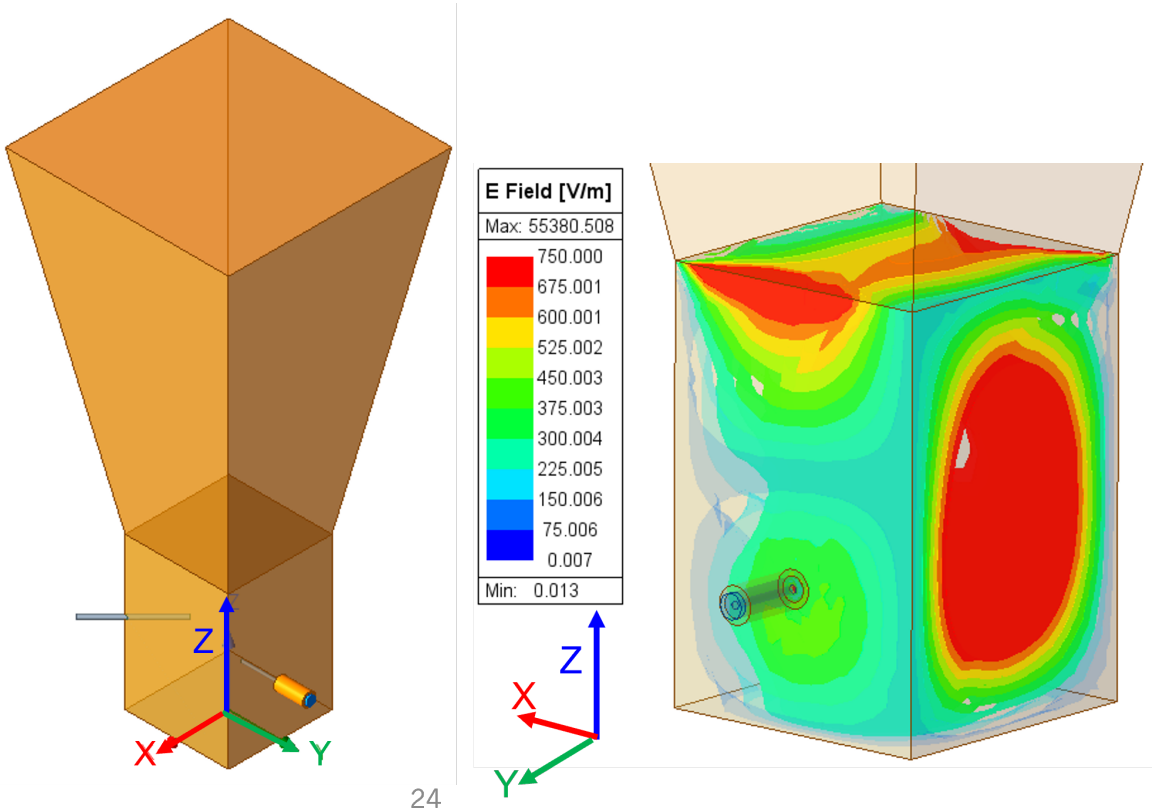

(a) **(b)**

Figure 5.8: The (a) horn structure with coupling screw polarizer in square waveguide feed, and (b) the field distribution within the square waveguide feed

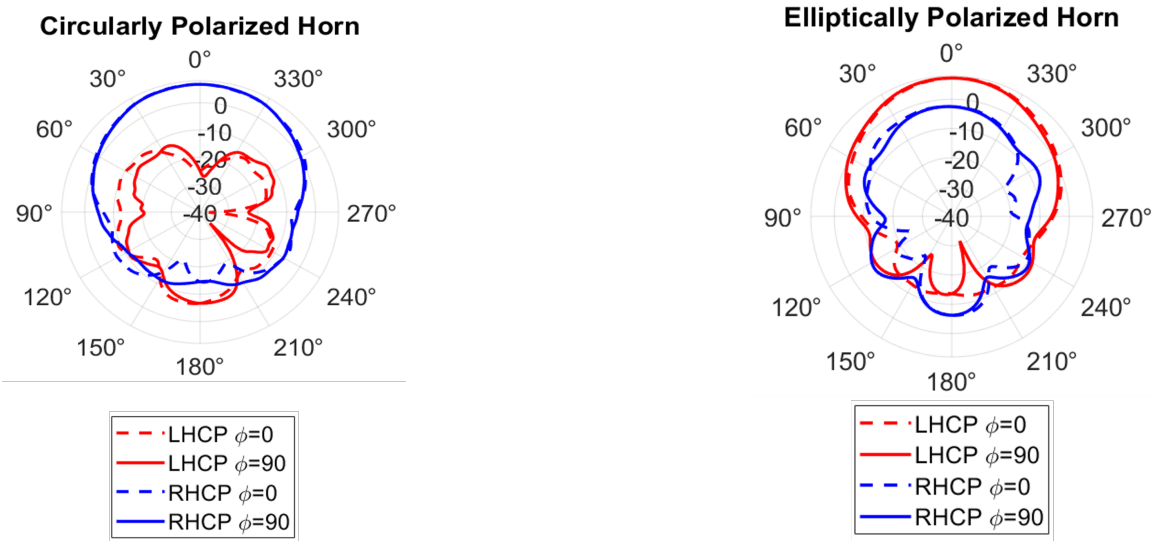

(a) **(b)**

Figure 5.9: The LHCP and RHCP realized gain radiation pattern of an (a) circularly polarized horn antenna, and (b) elliptically polarized horn antenna

that the axial ratio for the elliptically polarized horn is farther from 1 than the circularly polarized horn.



(a) **(b)**

Figure 5.10: The axial ratio of an (a) circularly polarized horn antenna, and (b) elliptically polarized horn antenna

5.2 Conclusion

A single coupling screw per cavity can be utilized to excite orthogonal degenerate modes for the design of a dual-channel filter. When the filter is attached to a horn antenna, dual-polarization is possible with a single coaxial probe feed. However, to achieve the 90° phase shift required for circular polarization, another mode-polarizing method is needed. Successful implementation could significantly impact the deployment of the remote filtering horn antenna by reducing feed complexity. This idea was not further investigated, as it fell outside the scope of the project. Further investigation into how a precise 90° phase shift method between the filter and horn would be implemented while not hindering the tunability of Q_{ext} is needed.

Chapter 6

Fabrication and Measurements

The conical horn cascaded with the third-order filter was prototyped to validate the proposed design. The tuned third-order Chebyshev filter, directly cascaded with the conical horn, was fabricated using stereolithographic additive manufacturing and plated with copper. Stereolithography is a method of additive manufacturing that has increasingly been used to fabricate radio-frequency (RF) components for its ability to produce complex geometries that traditional fabrication methods may struggle to achieve [62]. It operates by curing a thin layer of resin layer by layer using ultraviolet (UV) light [63]. The most typical material used in SLA is polymer, but ceramic and metallic photo-reactive materials have also been developed. SLA pieces need to be metallicized for RF components if they are not printed using metal. The common method for metalizing the structure is to deposit a conductive seed layer on the plastic and then electroplate to obtain a uniform copper layer [64] [65].

This chapter details the fabrication and measurement of the cascaded filter/horn antenna. The tuned filter/horn was additively manufactured via stereolithography (SLA) using the Formlabs Form 4 printer and Formlabs resin. Prototypes I-III were printed using the Formlabs grey V5 resin. For Prototype IV, the resin type was switched to Formlabs High Temp V2 resin in the hope that it would off-gas less during the electroless plating process and that the connectors could be soldered on. The structure then had a copper "seed" layer deposited by electroless copper plating to create a conductive surface for subsequent

copper electroplating. The filter/horn radiation pattern was measured in a far-field anechoic chamber, and the filter response of the reflection coefficient will be measured using a Field Fox vector network analyzer.

6.1 SLA Printing - Dividing Structure

The tuned conical horn cascaded with the third-order Chebyshev filter is 173.41 mm long and 56.48 mm wide at the largest points. The filter was attached directly to a conical horn 300 mm long, with an upper radius of 154 mm. The Formlabs Form 4 has a maximum build volume of 200 mm by 125 mm by 210 mm. Therefore, to print the filter/horn, it was necessary to divide the piece into parts that would be joined together using a flange structure.

One of the natural divide points is between the horn antenna and the end of the filter, with the iris being printed as part of the filter. However, the conical horn itself was still too large and had to be divided into four parts. As the overall length of the horn antenna was too large to fit in any orientation, it was decided to divide the horn in half horizontally, and then each half was split in half vertically. This left the conical horn broken down into four semicircular sections as seen in Fig. 6.1. The filter also needed to be split into parts due to its closed-square-cavity structure, as printing in one piece can result in internal supports that cannot be removed and improper curing. It also limits the flow of the copper plating solutions throughout the piece. By dividing the filter lengthwise, as shown in Fig. 6.2, the structures can be SLA-printed without failures, and the copper plating process is improved, as both electroless plating and electroplating require fluid movement throughout the structure.

Dividing radio-frequency structures into pieces requires careful consideration to avoid affecting performance. There will be surface currents that run along the walls of the cavity, and it is desirable to avoid cutting across the path of these currents whenever possible



Figure 6.1: Electroplated horn sections

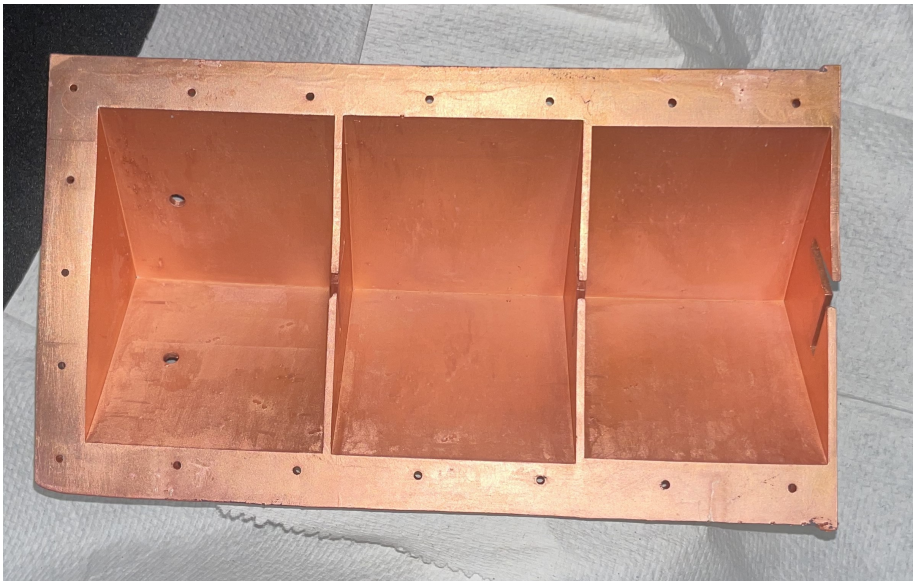

Figure 6.2: Electroplated filter half

[66]. In dual-polarized/dual-channel devices, it is also necessary to avoid disrupting the physical symmetry that maintains identical polarizations. There also needs to be a method for connecting the separate parts after fabrication. A flange structure does not produce a perfectly seamless result, but the impacts of flange gaps can be minimized through careful design. The exact location for splitting the structure was investigated by splitting the iris-coupled cavity feed of the horn to gauge how the splits affect the antenna's dual-polarization performance. The cavity feed was initially split straight down the x-axis as seen in Fig. 6.3. An air gap thickness of 0.2 mm was introduced to simulate the effects of a flange split. A gap size of 0.2 mm for a flange connection is on the optimistic side, given the tolerances of the SLA printer and the likelihood of warping during printing. Looking at the scattering parameters of the cavity-fed horn in both polarizations, it can be seen that adding a flange down the center of one polarization shifts the affected polarization in frequency and magnitude relative to the cavity without the gap. However, when the flange is added diagonally, as seen in Fig. 6.4, it shifts the response of both polarizations, but they stay identical. The return loss of both polarizations of a cavity feed with a straight split and no split can be seen in Fig. 6.5a and Fig. 6.5b shows the results of the diagonal split compared to having no split. To avoid differences in the two polarizations, it was necessary to split the cavity diagonally.

Another challenge posed by dividing the design into pieces is how the flange connection gap affects filter performance. The effects of gap size and material were investigated. The results of the gap size investigation can be seen in Fig. 6.6. The gap was simulated as vacuum for this analysis, and the filter was placed in a radiation box to effectively model the power escaping the filter. Performance increases as the gap size decreases, as expected. However, there are limits to how small the achievable gap size for a resin-printed flange can be. Experiments in printing demonstrated a typical gap size of about 0.5 mm. It did not remain consistent across the filter, especially in sensitive areas such as the irises, which

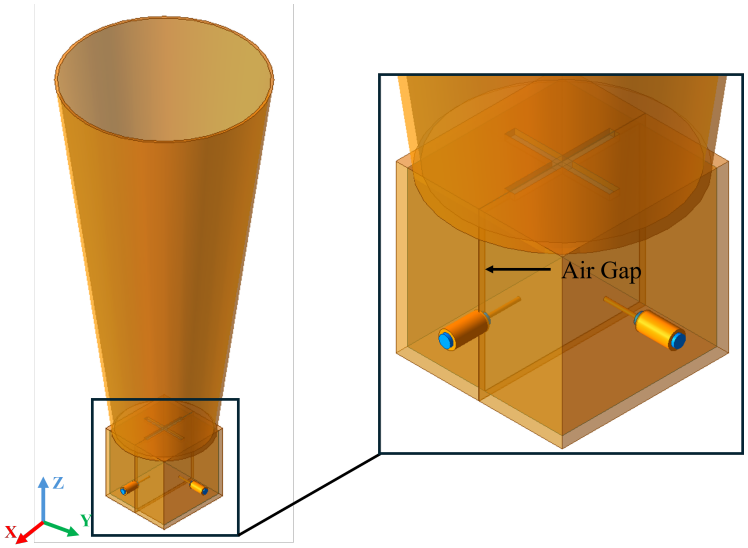

Figure 6.3: An image of the cavity feed to a conical horn split straight through one feed

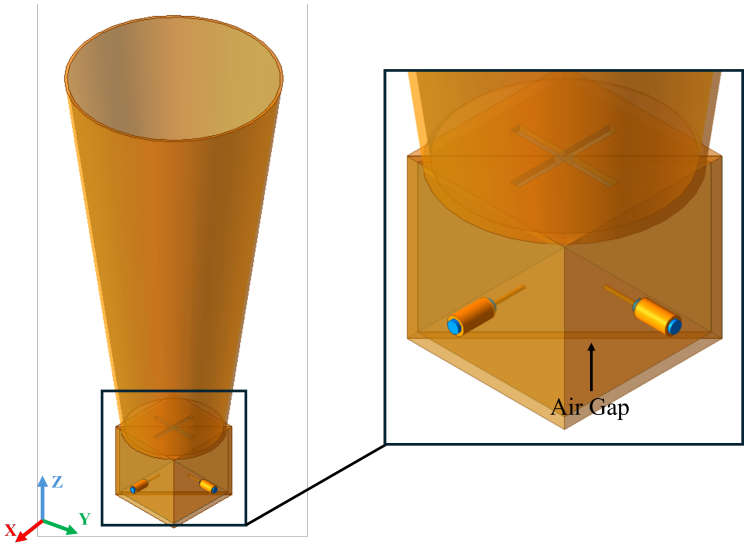

Figure 6.4: An image of the cavity feed to a conical horn split diagonally

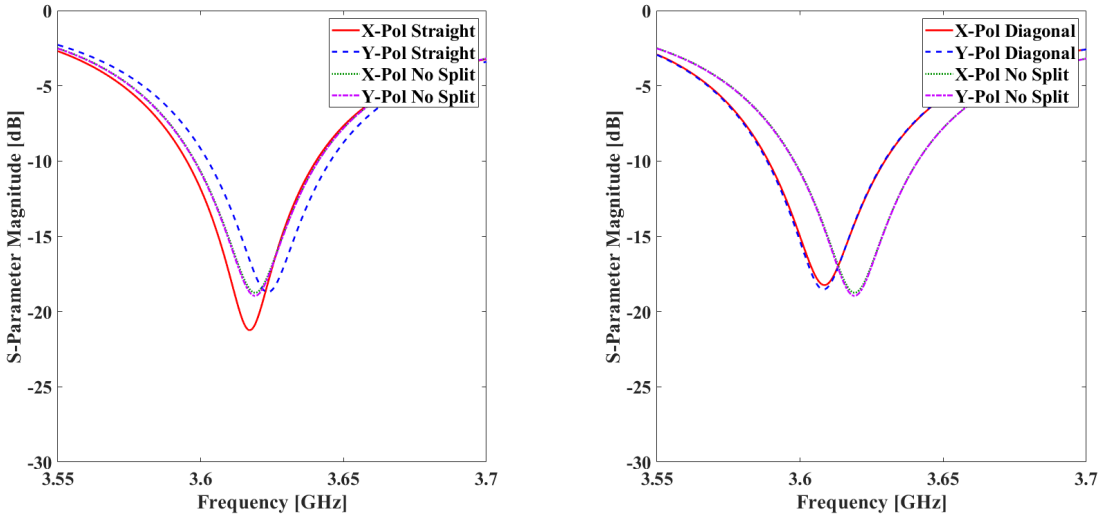

(a) **(b)**

Figure 6.5: The reflection coefficient of a cavity-fed horn with the cavity split (a) straight through one polarization, and (b) diagonally

were prone to warping.

Conductive epoxies were explored to fill these gaps when they could not be completely minimized. Silicone Solutions offers a range of conductive epoxies. The epoxy had to be carefully chosen because the polymer pieces are heat-sensitive. Even slight heat can cause off-gassing, and extreme heat can cause melting and warping. It was important that the chosen epoxy was curable at room temperature, had good electrical conductivity, and was not prohibitively expensive. The conductive epoxy chosen was the SS26-S silver epoxy. Although Silicone Solutions did not provide exact conductivities for their epoxies, silver has a conductivity of $6.3x10^7$ [67]. The flange and gap were simulated in Ansys HFSS, with the gap material modeled as vacuum and silver, and the results were compared with the filter performance without a gap, as shown in Fig. 6.7. Due to silver's superior performance over the vacuum gap, silver epoxy was chosen to form a gasket between the two flange halves.

The final analysis investigated the effect of surface roughness on the filter's performance. Surface roughness was found to vary between about 0.1 μm and 0.4 μm for SLA prints

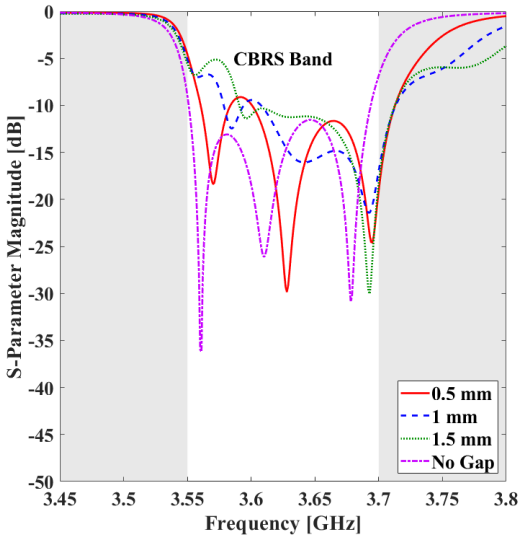

Figure 6.6: Reflection coefficient for different flange gap sizes is plotted

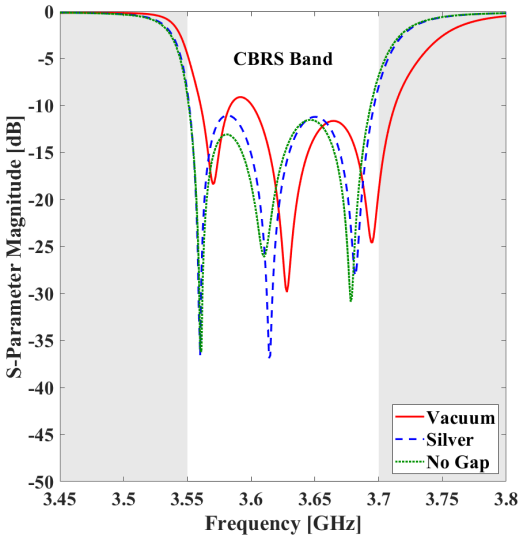

Figure 6.7: Reflection coefficient for different flange gasket materials is shown and compared to the filter without a flange gap

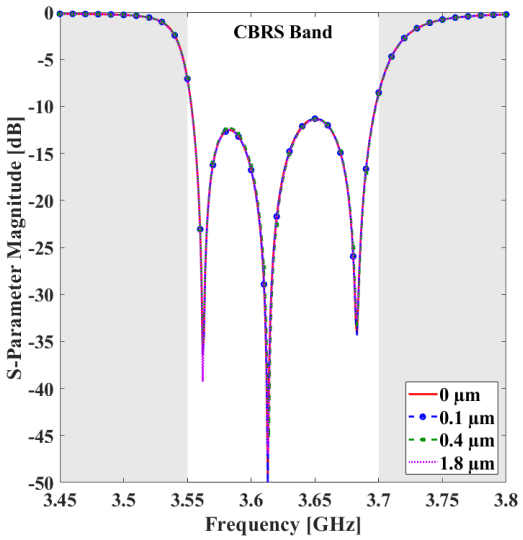

Figure 6.8: Reflection coefficient for different surface roughnesses is shown

with a surface roughness of 1.8 μm achievable with copper plating [63]. It was found that surface roughnesses of this magnitude had little effect within the CBRS band. The filter response as surface roughness changes is shown in Fig. 6.8. Higher frequencies are more sensitive to surface roughness because the roughness is larger relative to the wavelength, but the wavelength at f_0 of the CBRS band is 82.7 millimeters, so the design is not particularly sensitive to surface roughness.

6.2 SLA Printing - Printing, Cleaning, and Curing

The models to be SLA-printed were designed in Ansys HFSS and exported as .obj files for import into Preform, Formlabs' slicing software for the Formlabs printers. The printing files can be uploaded directly from Preform to the printer of choice. Following printing, the support structures were removed, and the pieces were thoroughly cleaned with isopropyl alcohol to remove any uncured resin before undergoing a final UV cure at $60°$C for the grey V5 resin, $80°$C for the High Temp resin. The pieces were then wet-sanded to remove sharp peaks and roughness from the supports, as shown in Fig. 6.9, which can impede

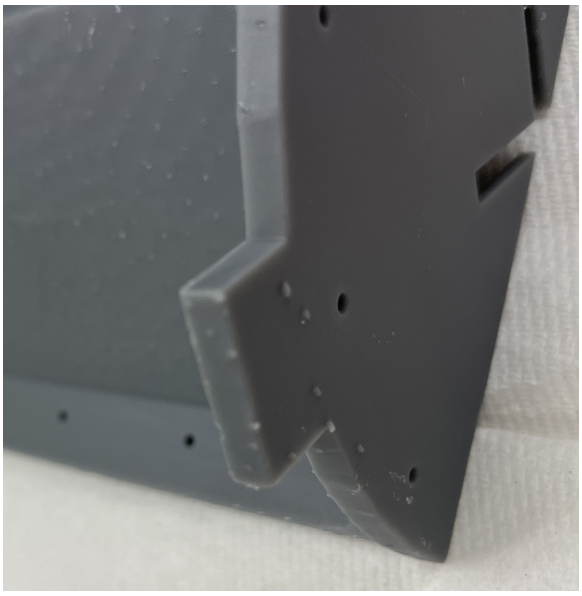

Figure 6.9: An image of the roughness of an SLA print before wet-sanding

plating. They then received a final cleaning using isopropyl alcohol to ensure the surface is completely clean. Any oils from fingers can leave fingerprints in the final plating, so it is best to always wear gloves when handling.

6.3 Electroless Plating

Electroless plating was conducted using a catalyst bath followed by a copper solution bath. The first step in the electroless plating process is to immerse the structure in the catalyst tank for 5 minutes. However, this was best practice for printed circuit boards (PCBs), not resin. A trade-off was observed: less catalyst time reduced the risk of delamination but also resulted in a thinner layer of copper coverage from the electroless plating. This variable can be adjusted to suit the needs of the specific piece. The catalyst tank is kept at $105°$F with a pump circulating the liquid. Following the dip in the catalyst, the piece is thoroughly cleaned with de-ionized (DI) water. This is a crucial step, as any liquid catalyst introduced into the plating bath will cause the bath to fail. This is typically indicated by the formation

of copper flakes that sink to the bottom of the bath or copper beginning to plate the sides of the glass bath. The wire and support structure used to dip the structure into the catalyst should also be changed to avoid cross-contamination.

The piece is then dipped in the copper bath. The copper bath, shown in Fig. 6.10, is heated to $115°$F with a pump or stirring, keeping the solution moving throughout the plating process. It is vital that the plastic not remain in the copper bath long enough to heat up and begin off-gassing. It was found best to remove the bath from the heat source and stir thoroughly before dipping the polymer piece to avoid the bottom of the bath being warmer than the top. It was also found that the best success was achieved by being closer to $105 - 110°$F, giving more leeway before off-gassing. Trial and error found the highest success with short dips of about 30 seconds followed by 30-45 seconds outside of the tank to allow the piece to cool before dipping again. This dipping process will be repeated until a solid copper layer covers the entire structure or delamination is observed. The piece is then cleaned thoroughly with DI water again.

There is some risk of electroless plating delamination, even with care to avoid overheating the piece, especially in complex areas such as corners and irises. An example of this delamination is shown in Fig. 6.12.

6.4 Electroplating

After the piece is electroless plated, a 6-mil layer of copper is applied via electroplating. It is likely there are gaps in the electroless plating that will not electroplate as they are non-conductive. These will be dealt with later. A current is chosen based on the set electroplating time and the surface area of the piece to be plated. The current is run throughout the conductive electroless plating layer while the piece is submerged in the electroplating bath. The metal rack and tank for electroplating are shown in Fig. 6.13. For larger pieces, it was



Figure 6.10: An image of the electroless plating bath used to deposit the copper seed layer

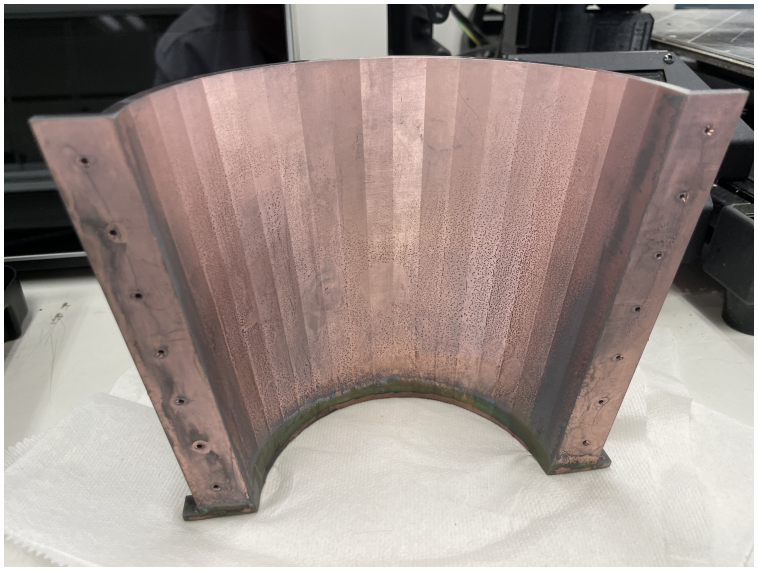

Figure 6.11: An example image of a piece following the electroless plating process



Figure 6.12: An example image of delamination of copper during the electroless plating process

most successful to have at least two points where the current is introduced to the piece. It is best practice to change the piece's orientation a few times to ensure even plating. The piece will come out of this first electroplating process looking like Fig. 6.14. The piece is then rinsed thoroughly.

Where gaps may be present due to insufficient electroless plating, SPI conductive silver paint was applied by brush to provide a conductive surface across the entire piece. The silver paint was chosen to be curable at room temperature and also capable of being used as a base for plating. This requires that the paint not be washed away by the water-based solution in the electroplating tank. The silver paint applied to the structure is shown in Fig. 6.15. The piece was then electroplated again with a 6-mil uniform copper layer across the piece, as shown in Fig. 6.16.

The silver paint was applied using both an airbrush and the brush that comes with it. The airbrush struggled to apply the paint smoothly, without clogging or producing large bumps, due to the paint's viscosity and texture. It also required a hood setup and the cleaning of the airbrush. The brush that comes with the paint was found to be convenient. Some

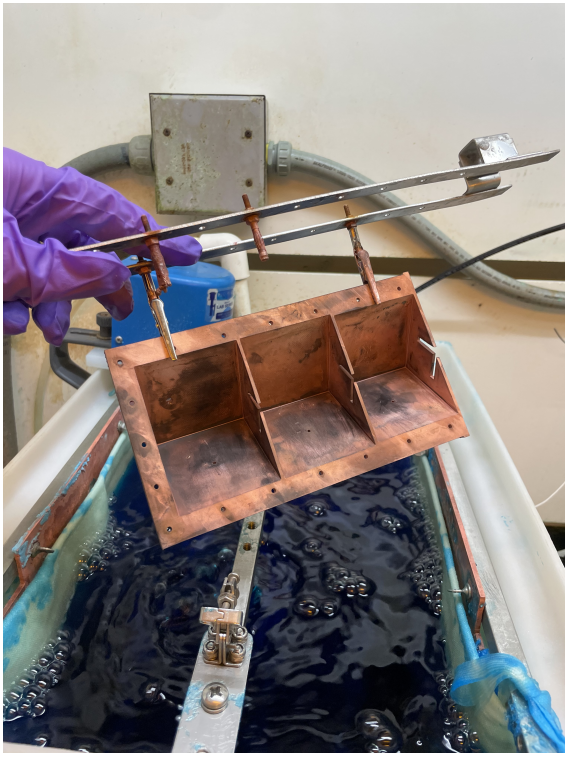

Figure 6.13: An image of the electroplating rack and tank

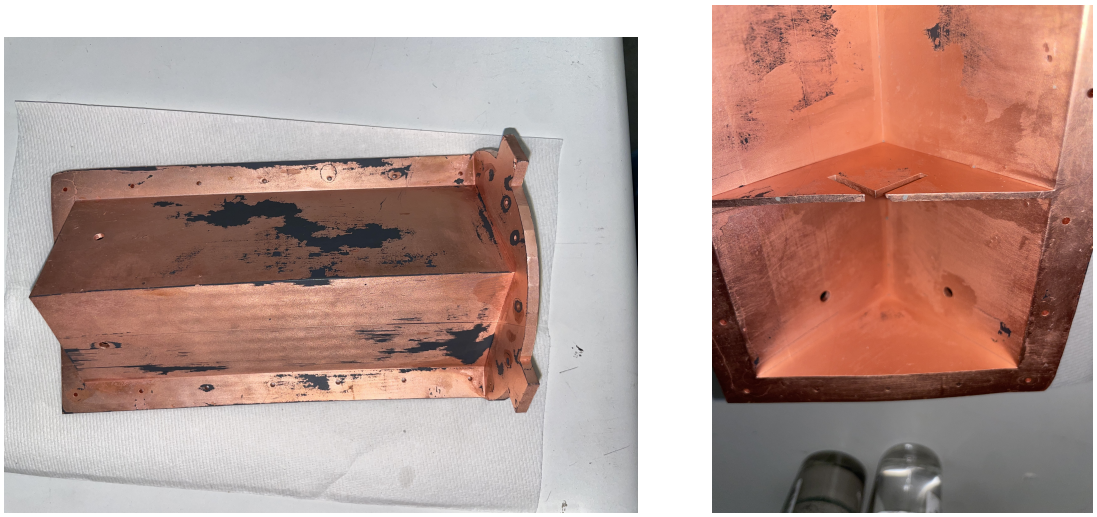

(a) **(b)**

Figure 6.14: Example images of the (a) outside of a resin print, and (b) inside of the piece after the first electroplating cycle

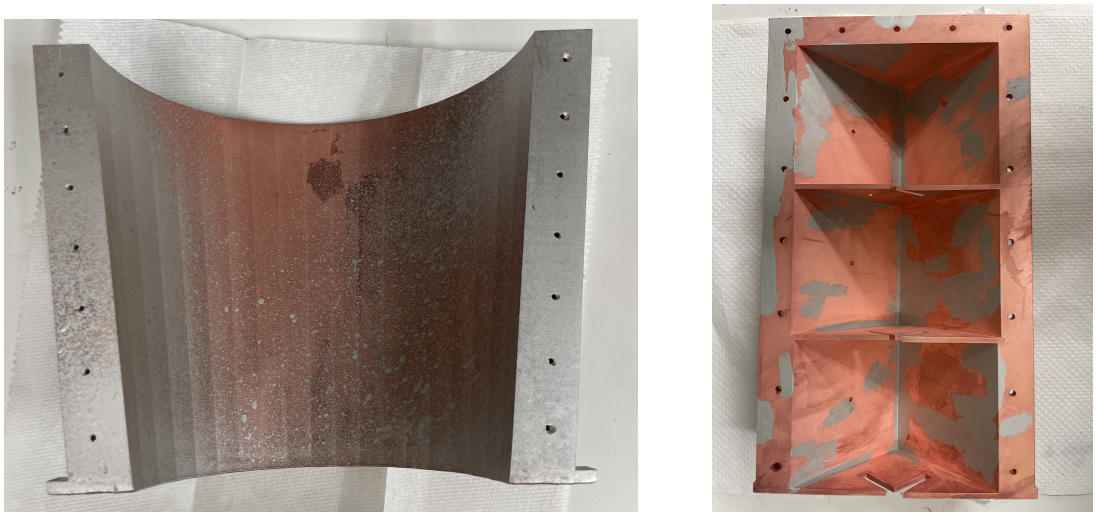

(a) **(b)**

Figure 6.15: Example images of the silver paint application (a) using an airbrush, and (b) a paintbrush

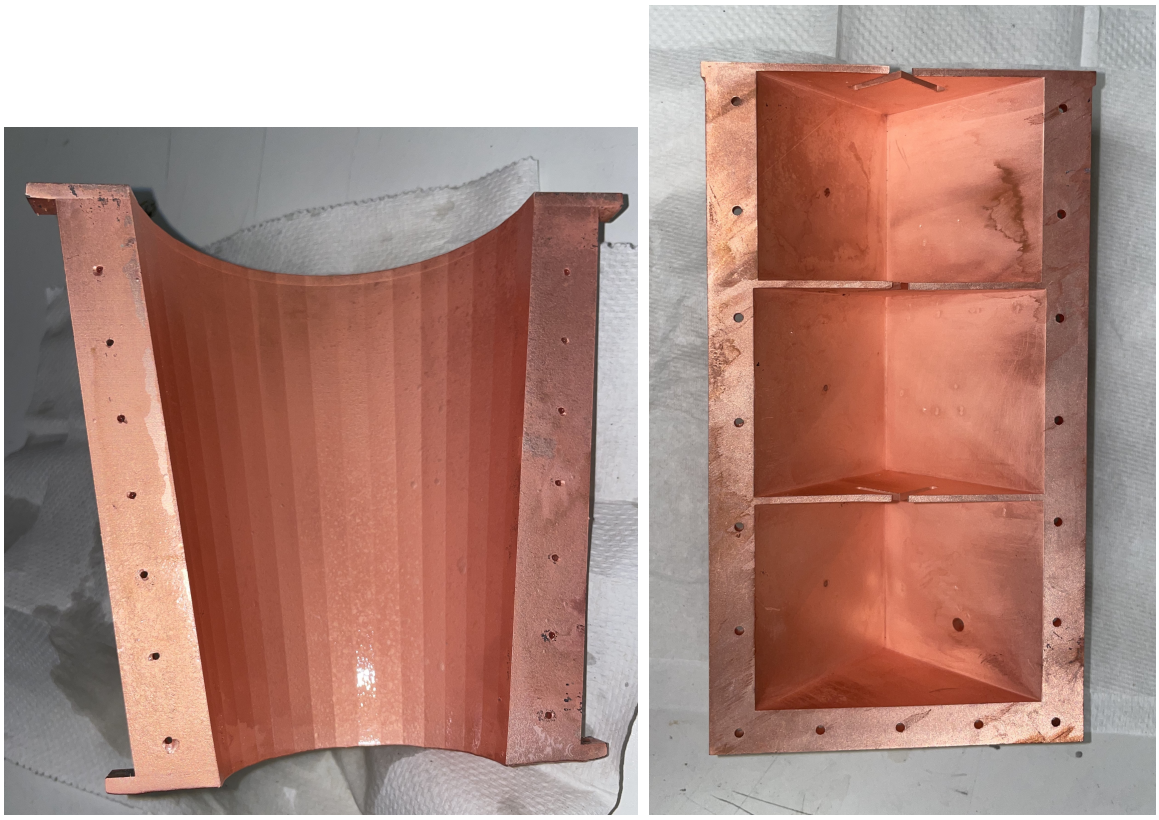

(a) **(b)**

Figure 6.16: Example images of the even copper plating after the final plating stage on (a) a quarter of the conical horn, and (b) half of the filter

brushstrokes remain in the final piece, but the paint dries fairly smooth. While the exact surface roughness could not be calculated for the final plated structure, the HFSS analysis indicated that the piece is not significantly affected by surface roughness at these frequencies. If the design operates at higher frequencies, it may become necessary to improve the paint application process. It was also tested whether the paint is better applied immediately following the electroless or after an initial electroplate. Applying the paint after an initial electroplating stage was found to yield the best results because it makes it much clearer which spots did not receive sufficient coverage. After the electroless plating process, it can be heard to determine exactly where coverage is lacking, as seen in Fig. 6.11. When the paint was applied between electroless plating and initial electroplating, gaps remained after electroplating, so more silver paint had to be applied, and the piece had to be electroplated again anyway.

6.5 Finishing Structure

The coaxial probes were attached after the electroplating process, while the piece was still open, as shown in Fig. 6.17, allowing the probes to be tested for connectivity and adjusted as needed to match the simulation as closely as possible. A thin layer of the silver conductive epoxy was then applied around the edge of each flange, shown in Fig. 6.18, and along the areas where the irises meet. This was done to attempt to fill the gaps due to the flange. This is an imperfect process, as care has to be taken to apply the epoxy carefully along the irises, such that enough is deposited to fill the gaps, but not so much that it fills the iris. There is no sufficient way to clean or adjust this epoxy in the interior irises after these two pieces are pressed together. At the CBRS band, better performance is seen by risking a slight overflow of the epoxy onto the walls of the iris (as long as it is not within the iris) than by not completely filling the gaps in the iris walls. After applying the epoxy, the two sides of

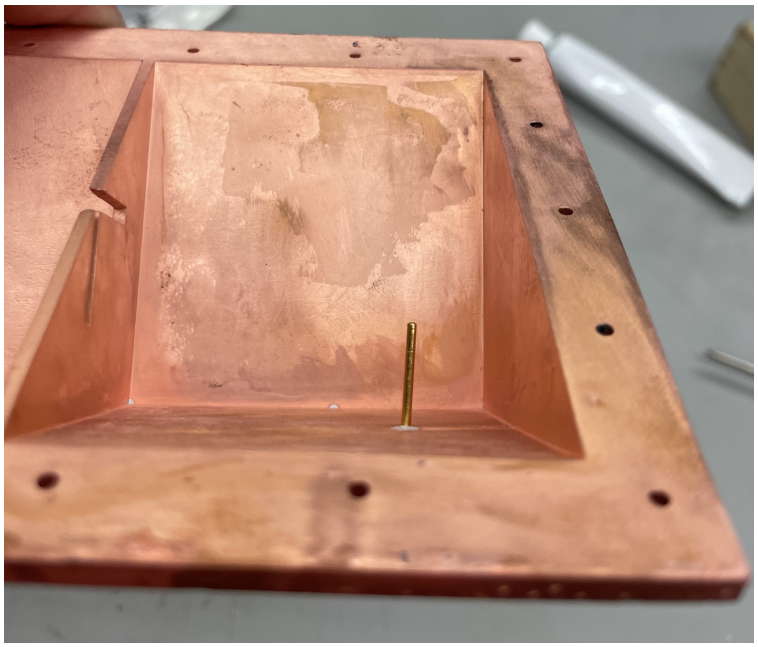

Figure 6.17: An image of the coaxial probe inserted into half of the cavity structure

the filter are bolted together at the flanges using M2 Phillips pan-head bolts with washers and nuts on the other side. This can be seen in Fig. 6.19. This process needs to be completed quickly to avoid disrupting the epoxy as it begins to dry. Once the two pieces of the filter are connected, the filter is then connected to the horn as shown in Fig. 6.20.

6.6 Measurements

Measurements of the filter/horn were taken in a far-field anechoic chamber capable of measuring from 300 MHz to 18 GHz. The horn under test (HUT) was connected to the bulkhead of the chamber, and the bulkhead was connected to a Field Fox N9917B Microwave Analyzer to take scattering parameter measurements and was switched to the Agilent Technologies N5222A PNA Network Analyzer to take radiation pattern measurements. The HUT was set as a receive (RX) horn, and a dual-ridge horn was used as the transmit (TX) horn. Both antennas were raised on pedestals above the chamber's noise floor (about 14 feet in the air).

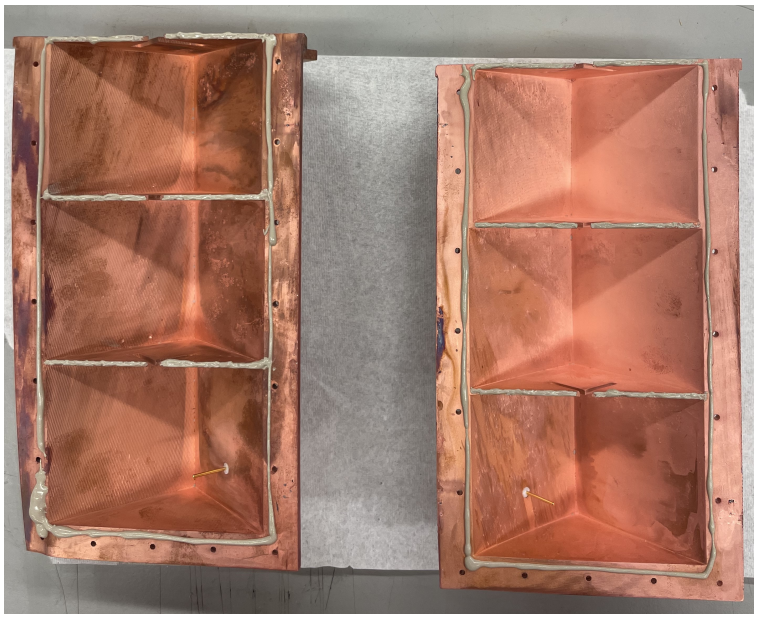

Figure 6.18: An image of the application of conductive epoxy around the flange

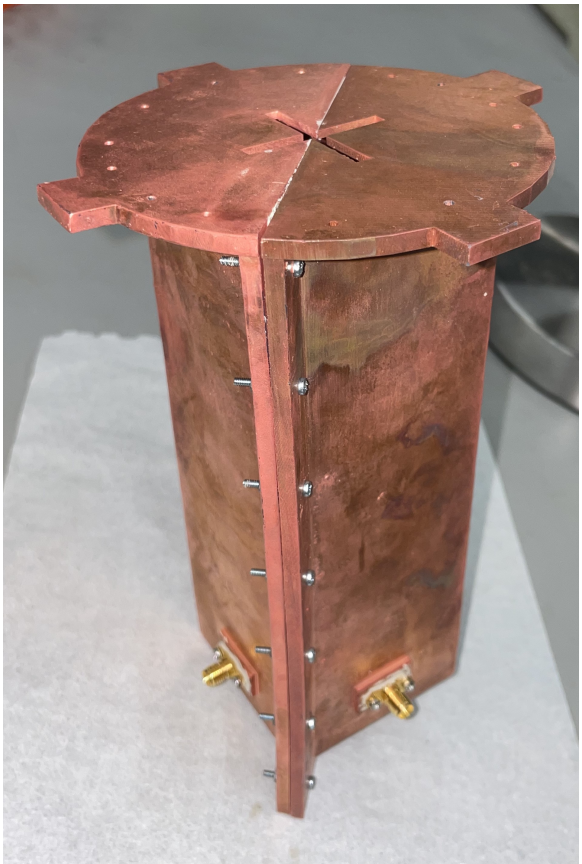

Figure 6.19: An image of the two halves of the filter Prototype II bolted together using M2 pan head bolts, washers, and nuts



Figure 6.20: An image of the filter bolted to the conical horn

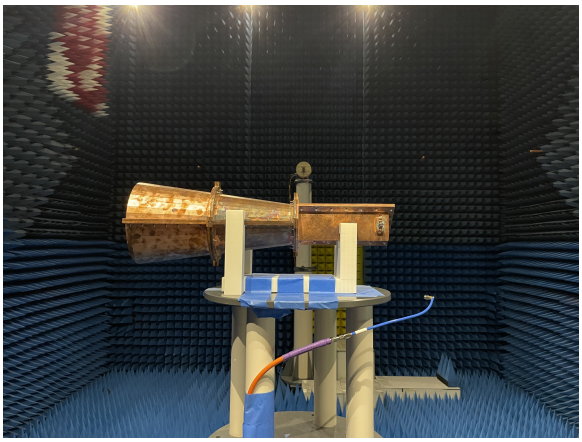

Figure 6.21: An image of the HUT mounted on the anechoic chamber pedestal

A mount for the filter/horn was additive manufactured for measurements using a Bambu Labs X1 Pro Carbon. This custom structure allowed the horn under test (HUT) to be securely attached to the anechoic chamber pedestal at a fixed location and to remain level. It needed to be sufficient to remain stable as the horn was rotated for full radiation pattern measurement. The horn was then mounted on the pedestal in the anechoic chamber as seen in Fig. 6.21.

6.7 Prototypes

It took four full filter iterations to achieve an acceptable filtering response. The horn antenna is a fairly basic structure and was successfully achieved with a single prototype. The four iterations of the filter will be explained in this section. There is a discussion of the issues with each and what was adjusted before the next prototype.

6.7.1 Prototype I

The first filter prototype is shown in Fig. 6.22. This prototype had just a hole in which the coaxial probe feed was inserted. The two halves of the filter structure were joined with conductive epoxy in the flange before the coaxial probes were inserted. This left no room

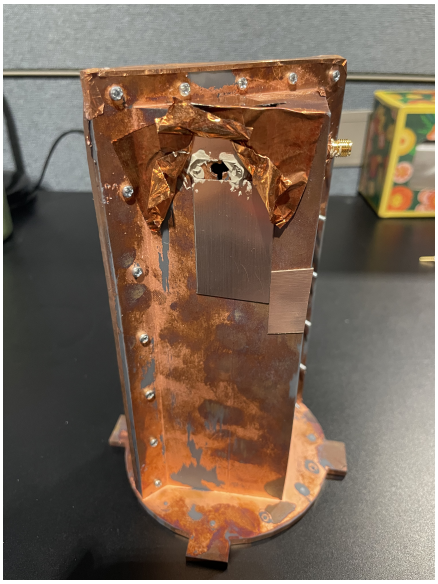

Figure 6.22: An image of the first filter prototype with the copper tape covered crack visible

to adjust how the probe was inserted, and upon attempting to insert it, one side of the filter cracked significantly. This crack was covered with copper tape, but it ran directly through the hole where the probe needed to be inserted. The two feed probes were then attached with silver conductive epoxy to secure the connector wings to the outside of the filter. This prototype also had a significant warp in both halves of the filter, preventing them from fitting together tightly. This is particularly problematic in the flange gaps on the iris walls of the filter. This essentially caused a third diagonal slot in the iris. The feed failures were catastrophic for the operation of this prototype, so the only measurements possible were the return loss of the filter's polarization in the semi-successful feed. This filter performance can be seen in Fig. 6.23. All three poles of the filter are demonstrated, but they are very weakly coupled, and there is 5 dB of return loss even outside of the passband. There is also a pretty significant resonance seen at a higher frequency. Later, it was found that the thickness of the wall at the feed was incorrectly calculated and that the feed insertion into the cavity was at least 0.5 mm shorter than simulated. The significant impact of a shortened probe compared to the tuned length probe can be seen in Fig. 6.24.

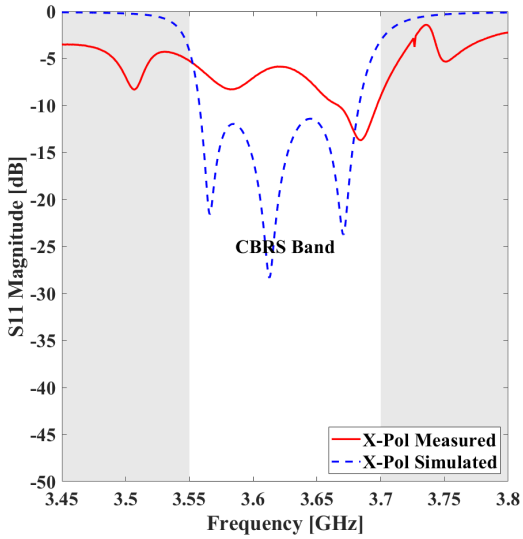

Figure 6.23: Filter response of Prototype I

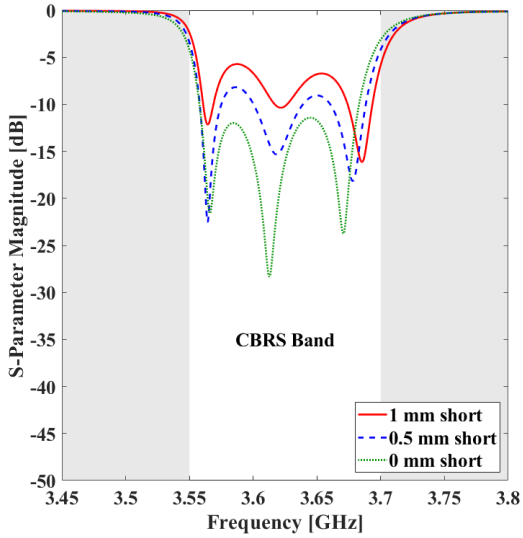

Figure 6.24: Simulated filter response with probe length shortened from tuned filter probe length

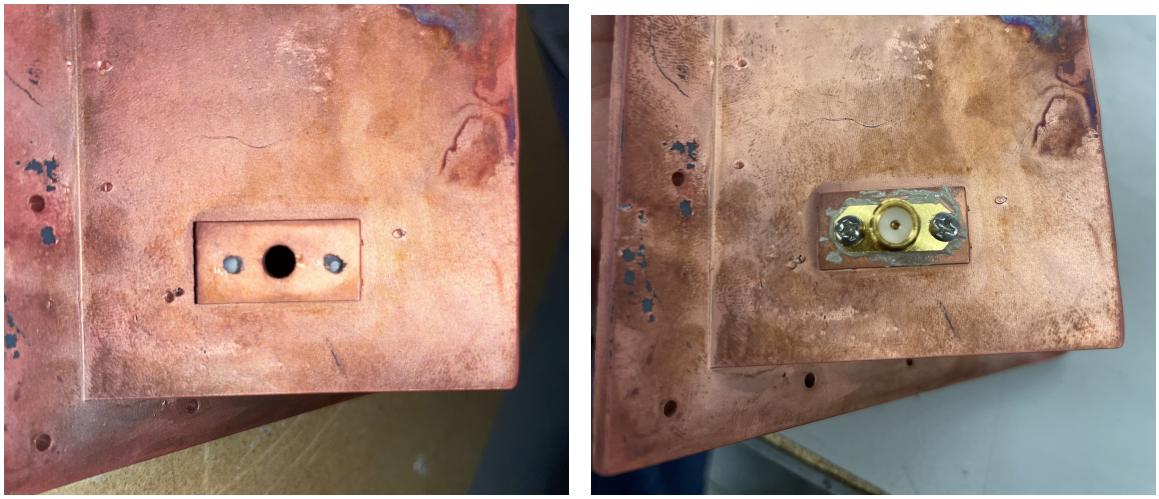

(a) **(b)**

Figure 6.25: Image of the feed of the second prototype with (a) holes drilled for the bolts, and (b) the connector attached

6.7.2 Prototype II

A few things needed to be addressed in the second prototype. The most important of which was the attachment of the coaxial probe feed. A pad, seen in Fig. 6.25a, was added to the outside of the filter to adequately thicken the wall of the filter to allow short M2 Phillips pan head bolts to be inserted to hold the coaxial feed in place. These bolts had to be screwed into the filter walls without penetrating. The coaxial feed was then screwed into the pad with conductive epoxy between the wings of the outside of the connector and the pad it was being screwed into. This feed structure can be seen in Fig. 6.25b. This was done while the two halves of the filter were separate, allowing for the coaxial probe insertion to be checked on the inside.

The warp in the SLA print was reduced by using a different print orientation. Multiple attempts were made, and the warp was reduced but not completely eliminated in Prototype II. The warp was largely in one corner of the flange, so the gap was filled with epoxy as seen in Fig. 6.26. A thin line of conductive epoxy was applied around the entire filter, and on the edges where the iris walls will meet. A thicker layer was applied where the warp

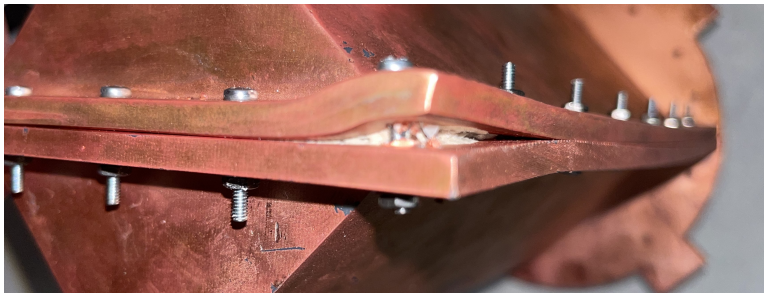

Figure 6.26: An image of the gap in the flange due to print warping that has been filled with conductive epoxy

was present in the flange to fill the gap with a conductive material and reduce its impact on performance. The flanges were then bolted together. Looking into the top slot of the filter, it was found that the corners of the flange gaps in the iris walls were filled, but not enough epoxy was applied to fully fill the gaps. The flange gaps in the exterior cavity walls were completely filled, though.

The filter/horn was measured, and the frequency response of the filter/horn for the two horn polarizations, compared with the simulation, is shown in Fig. 6.27. The anechoic chamber facilities used for measurement did not support true dual-polarized measurements, so for each polarization feed (x-polarized and y-polarized), the copol and crosspol patterns were measured and compared to the simulated. These can be seen in Fig. 6.28a and 6.28b. The filter response for the x-polarized case is much worse than for the y-polarized case, and the loss is higher outside the passband because the connector was loose and did not make good connection. Later, it was also found that the wall thickness had been miscalculated, so the probe was one millimeter shorter than simulated. Another prototype was fabricated to improve epoxy coverage of the flange gaps, match the coaxial probe to the simulation as closely as possible, and ensure a sufficiently strong attachment of the coaxial probes to withstand the mechanical stresses of attaching cords for measurements.

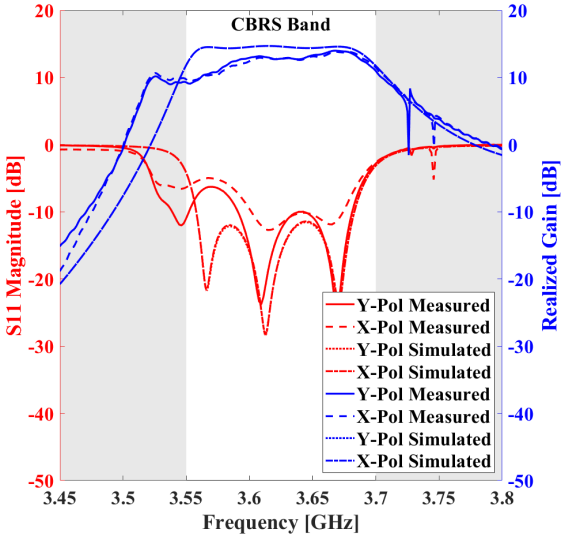

Figure 6.27: Measured frequency filter response for Prototype II compared to simulated

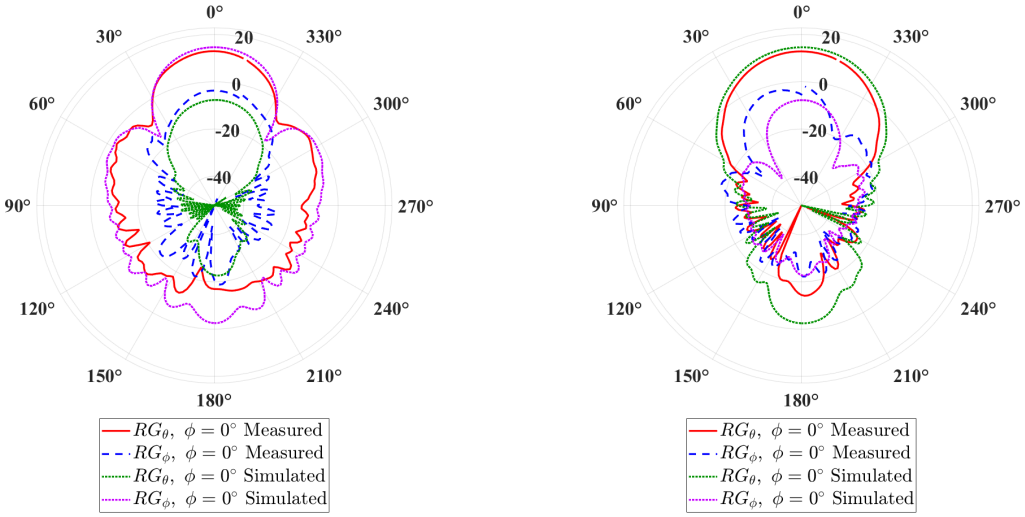

(a) **(b)**

Figure 6.28: Measured radiation patterns for Prototype II compared to simulated at 3.625 GHz for the (a) x-polarized, and (b) y-polarized feed

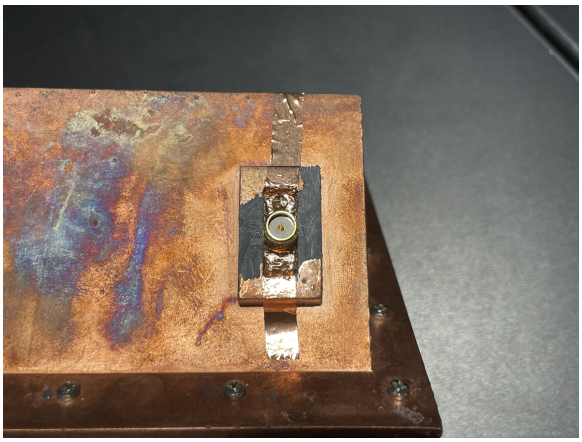

Figure 6.29: An image of the feed for Prototype III

6.7.3 Prototype III

To improve the coaxial probe feed strength, the filter was printed with an inset section that completely surrounds the wings of the coaxial connector, providing a pressure fit that keeps the coaxial probe inserted tightly and reduces movement during measurements. The coaxial probe inside the filter cavity was also carefully measured using calipers to ensure it was exactly the length simulated. The wings of the coaxial probe connector were then super-glued to the filter inside of the fitting, and copper tape was used to ensure a good electrical connection between the outside of the filter and the outside of the coaxial connector, as shown in Fig. 6.29. Conductive epoxy was applied to the two sides of the filter flange and in the gaps in the iris walls before it was bolted together.

The filter in this prototype was printed in an entirely different orientation than the previous filters. It was oriented so that the long sides were more vertical than horizontal when printing. This reduced the load on the supports and resolved the warping issue observed in earlier prototypes. The flanges achieved a close fit through the entire filter.

Prototype II indicated possible detuning in the resonant frequencies of the cavities, so Prototype III was designed so that tuning screws could be inserted into the cavities for frequency tuning as needed using the method discussed in [61] [60]. Holes were drilled

before the filter halves were attached, and the halves were covered with copper tape for the initial measurements to observe the filter response without screws inserted, with the option to insert them later. They could not be drilled once the halves were attached because the conductive shavings would be trapped in the cavities, and drilling from the outside in could cause a blowout of the surface inside the cavity. Threads for M2 bolts were attempted. However, the polymer structure was too soft to support threading. The holes remained tight enough that screw insertion could be adjusted with caution.

The filter response of the x- and y-polarized feeds was measured and plotted in Fig. 6.30. The filter couplings are improved by using the proper feed probe length. The entire filter response is shifted down in frequency by about how much did it shift GHz. However, the couplings all seem well-tuned, and the filter's bandwidth is correct. There is a lower-than-expected return-loss ripple of about 6 dB, and around 4 dB of loss across the entire measured frequency range. This indicated a loss in the feed, likely due to the coaxial probe being super-glued to non-conductive plastic on the outside of the filter, reducing the shielding at the feed insertion. The ground connection to the filter was made through copper tape, which is also lossy. It can also be seen in Fig. 6.31 that the sidelobe levels, the number of sidelobes, and the backlobe levels increased. This is due to improper shielding around the coaxial feed, allowing currents to travel along the outside of the horn and radiate.

6.7.4 Prototype IV

The fourth prototype was fabricated in much the same way as Prototype III, except it was printed using Formlabs' High Temp resin and the probe feed connector was soldered directly to the metallicized outside of the filter structure, shown in Fig. 6.32, in an attempt to reduce losses at the feed. The tuning screws were also removed because, without the ability to create threads in the plastic, they could not be kept at consistent lengths inside the filter. Prototype

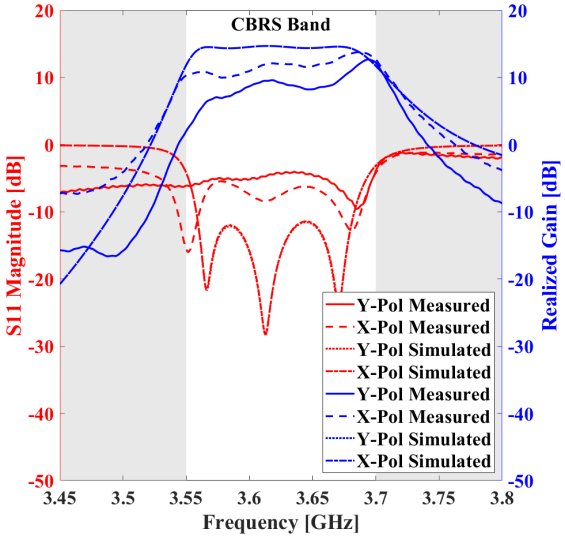

Figure 6.30: Measured frequency filter response for Prototype III compared to simulated

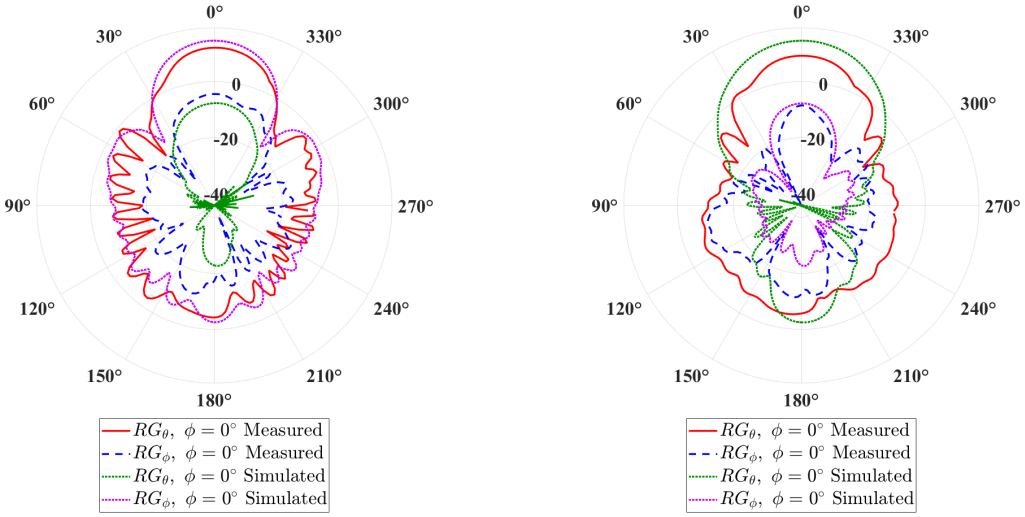

(a) **(b)**

Figure 6.31: Measured radiation patterns for Prototype III compared to simulated at 3.625 GHz for the (a) x-polarized, and (b) y-polarized feed

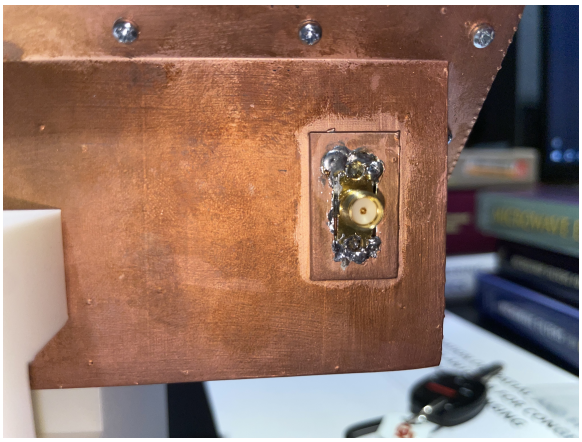

Figure 6.32: An image of the feed for Prototype IV

III also indicated that the frequency tuning is close to simulation, with the coupling issues addressed. Electroless plating was unsuccessful on the Formlabs High Temp V2 resin. This is likely due to material breakdown. The manufacturer recommends limiting isopropyl exposure to less than 6 minutes due to surface breakdown. The catalyst bath is acidic, which likely broke down the resin surface and prevented successful adhesion.

Prototype IV was first measured without conductive epoxy between the gaps in the filter flanges. Analyzing the filter response in Fig. 6.33, it can be seen that the coupling was significantly degraded. The horn radiation patterns plotted at 3.625 GHz in Fig. 6.35 also have very little separation between the co- and cross-polarized gain. Looking at the time-domain plots in Fig. 6.34, it was difficult to determine exactly what coupling was incorrect, as the humps indicating Q_{ext1} and $k_{1,2}$ were so far off they could not be distinguished. However, when the radiation patterns were analyzed, it became clear that the diagonal gaps across the iris, due to the way the filter was split, introduced mixed electric-magnetic coupling and coupled the two polarizations. This is indicated by the low separation between co- and cross-polarizations.

The conductive epoxy was then applied between the flanges and the gaps in the iris walls. The filter response, shown in Fig. 6.36, was significantly improved. The x-polarized filter

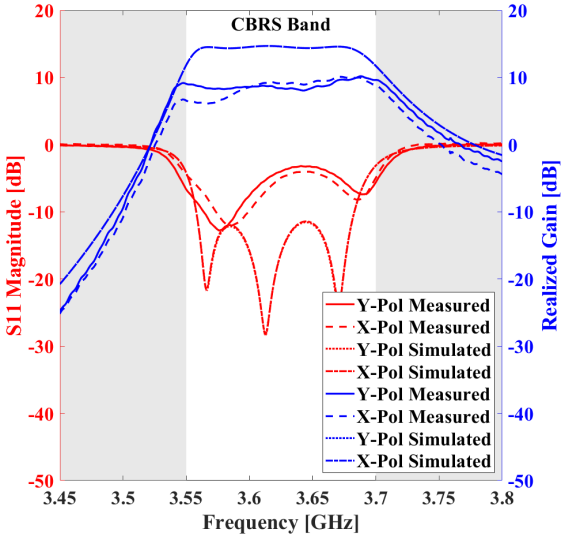

Figure 6.33: Measured frequency filter response for Prototype IV without conductive epoxy compared to simulated

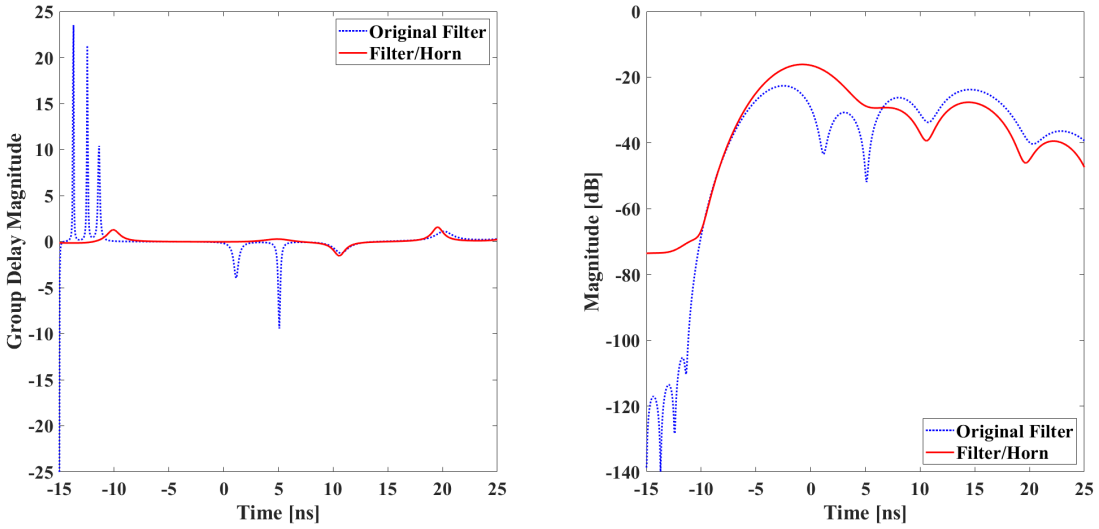

(a) **(b)**

Figure 6.34: The (a) group delay, and (b) magnitude of the time-domain response for Prototype IV without conductive epoxy compared to simulated

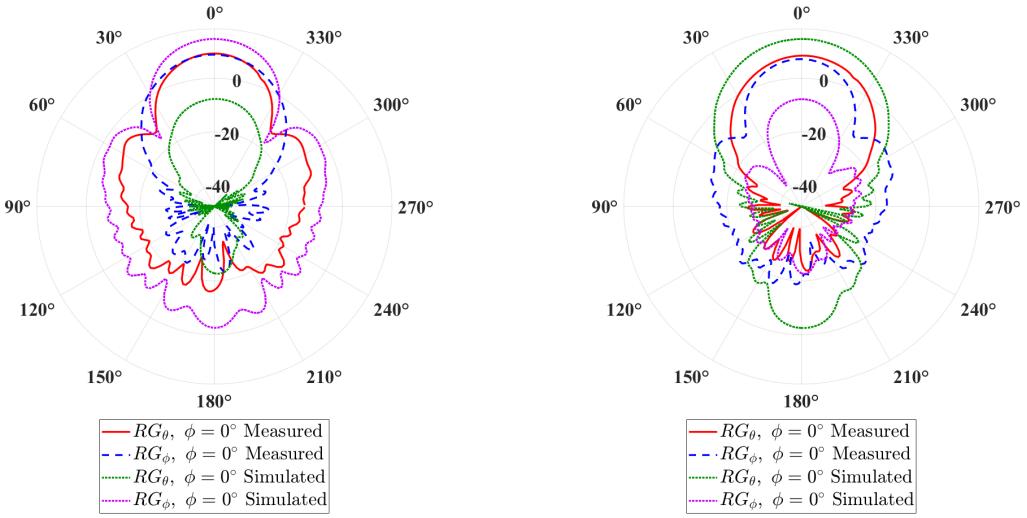

(a) **(b)**

Figure 6.35: Measured radiation patterns for Prototype IV without conductive epoxy compared to simulated at 3.625 for the (a) x-polarized, and (b) y-polarized feed

response matches the simulated response, except that the nulls are not quite as deep. The y-polarized filter response is close to simulated, but the bandwidth is slightly wider. Also, the filter coupling is not quite right, as indicated by the wider frequency-domain humps. It appears that the y-polarized response is closer to that of the filter without epoxy, suggesting a gap that may not be completely filled with epoxy. However, even the highest return-loss ripple is still lower than the 8.89 dB ripple corresponding to the 0.6 dB insertion-loss ripple for which the filter was designed. Therefore, the fabricated filter response meets specifications, except for a slightly wider bandwidth in the y-polarization. The radiation patterns for the conical horn compared to simulated are plotted at 3.625 GHz in Fig. 6.37. The main-beam gain of the fabricated filtering horn is less than 0.9 dB below the simulated case for both x- and y-polarization and both orientations, at 13.6 dB. There are some differences in the side and backlobes between the simulated and fabricated filtering horns. This is due to the way the flanges on the outside of the conical horn re-radiate the currents that travel down the outside of the horn from the aperture.

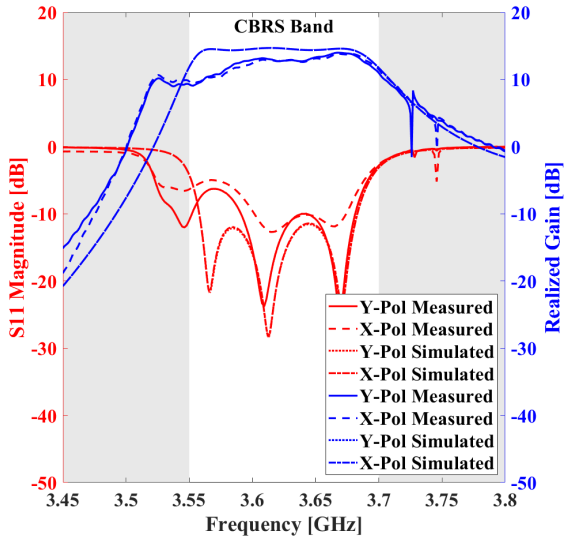

Figure 6.36: Measured frequency filter response for Prototype IV with conductive epoxy compared to simulated

The radiation patterns were also analyzed at the edges of the passband to ensure adequate radiation performance throughout the band. Analyzing the filter response in Fig. 6.36, it can be seen that the gain of the horn is lower than the simulated horn by approximately 2 dB at the bottom of the passband. Looking at the radiation patterns plotted at 3.56 GHz in Fig. 6.38, it can be seen that the radiation patterns also show a 2.67 dB reduction relative to the simulated gain, with a peak gain of 11.93 dB. It can also be seen that the cross-polarized gain is much higher than the simulated and demonstrated values at the center frequency. This mirrors the behavior of Prototype IV without epoxy in the flange gap, plotted in Fig. 6.35. It is likely, based on the higher cross-polarization, that the loss at the bottom of the band in the filter response is due to power being coupled to the cross-polarization appearing as loss in the co-polarized gain plotted for the filter response. This could be caused by a few factors, such as gaps in the conductive epoxy application around the flange/irises or shape deviations in the slot that affect polarization separation. Due to slight warping during SLA printing, the long edges of the magnetic coupling slots exhibited bowing in the middle, which could facilitate mixed coupling.

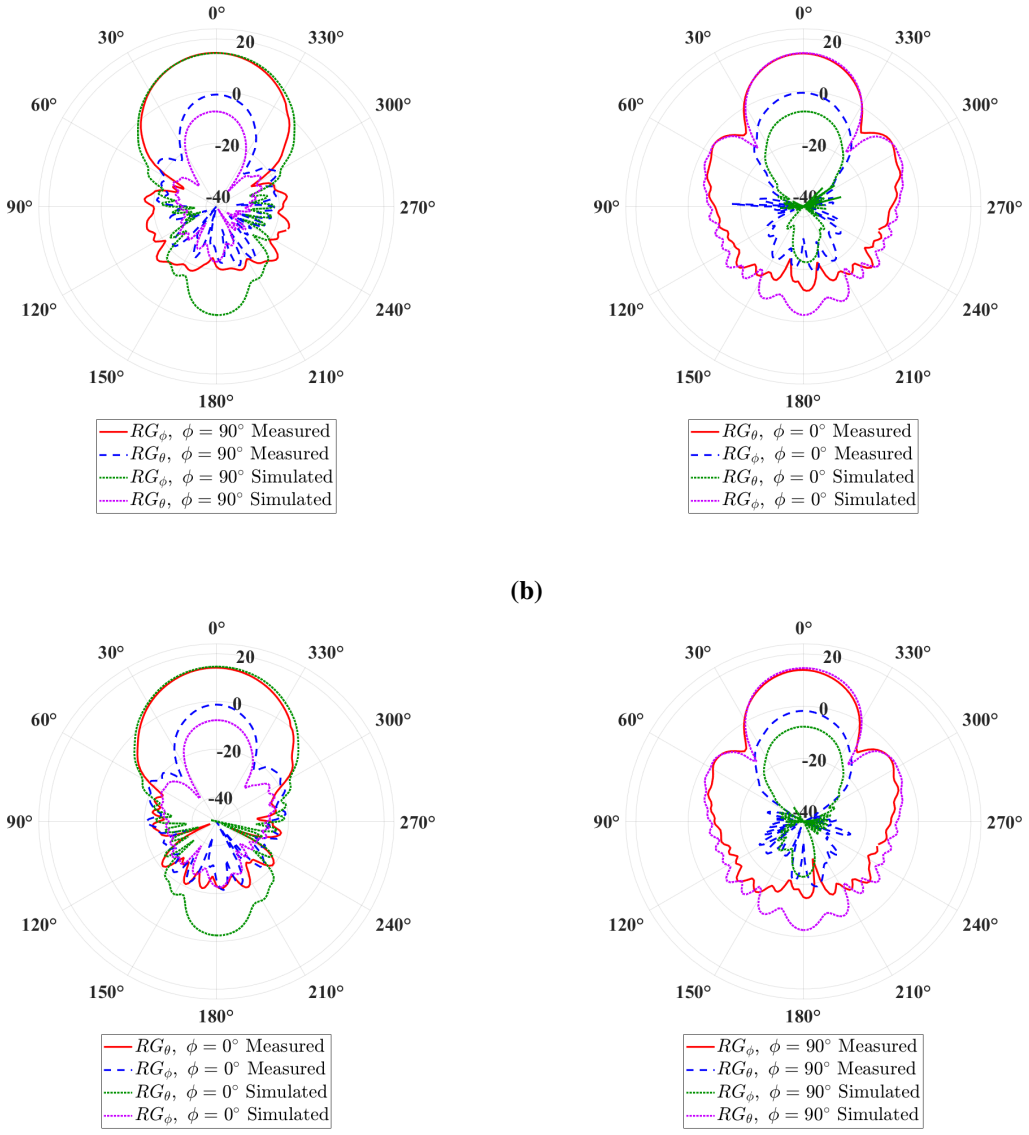

Figure 6.37: Measured radiation patterns for Prototype IV with conductive epoxy compared to simulated at 3.625 GHz for the (a) x-polarized vertically oriented, (b) x-polarized horizontally oriented, (c) y-polarized vertically oriented, and (d) y-polarized horizontally oriented

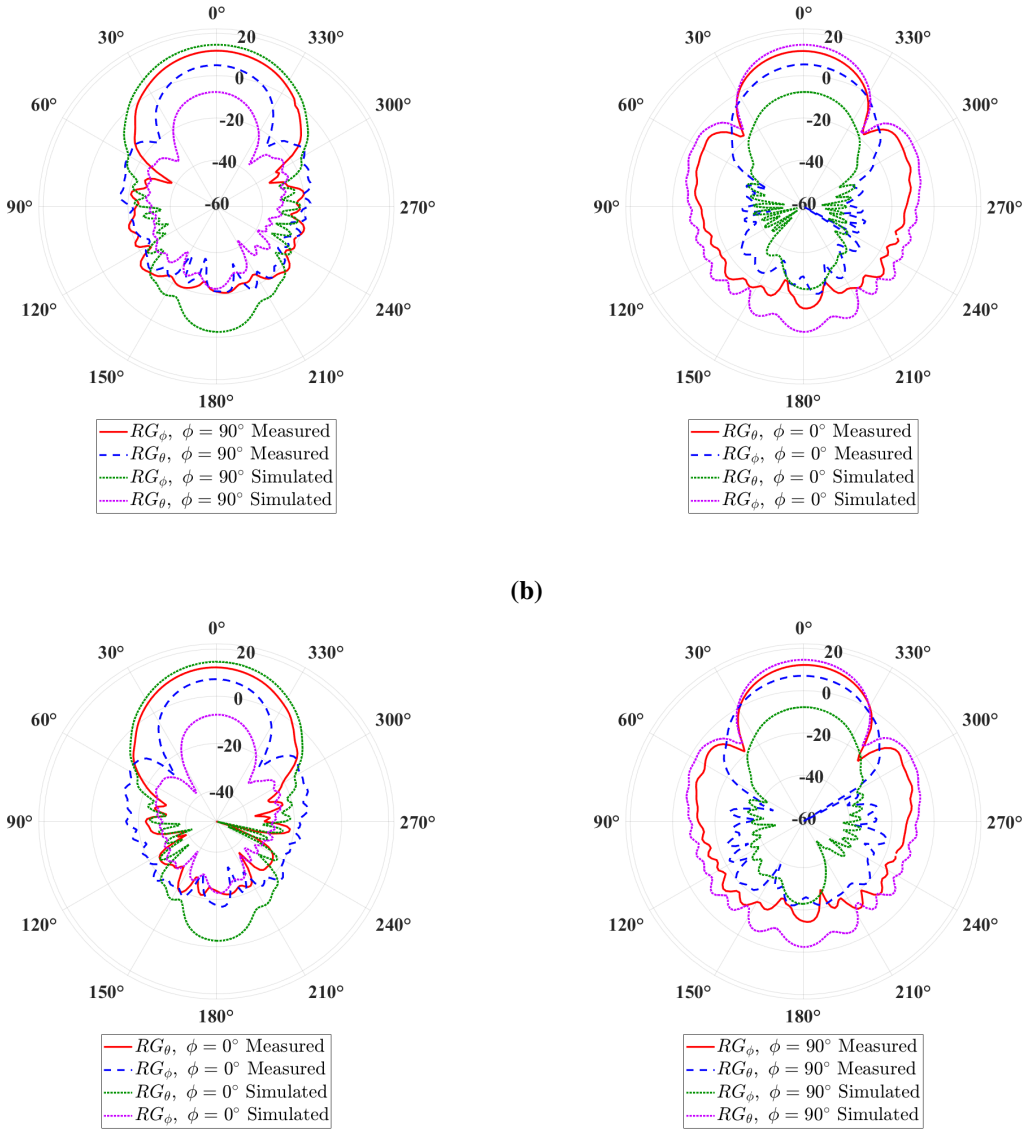

Figure 6.38: Measured radiation patterns for Prototype IV with conductive epoxy compared to simulated at 3.56 GHz with the (a) x-polarized vertically oriented, (b) x-polarized horizontally oriented, (c) y-polarized vertically oriented, and (d) y-polarized horizontally oriented

The radiation patterns of the filtering horn were also plotted at the upper end of the band at 3.68 GHz in Fig. 6.39. The gain is 0.46 dB below that of the simulated filtering horn, which has a peak gain of 14.13 dB, as expected from the filtering response. The cross-polarization gain is also lower than that observed at the lower or middle of the band, about half a dB below the simulation, indicating that little power was coupled between polarizations at 3.68 GHz.

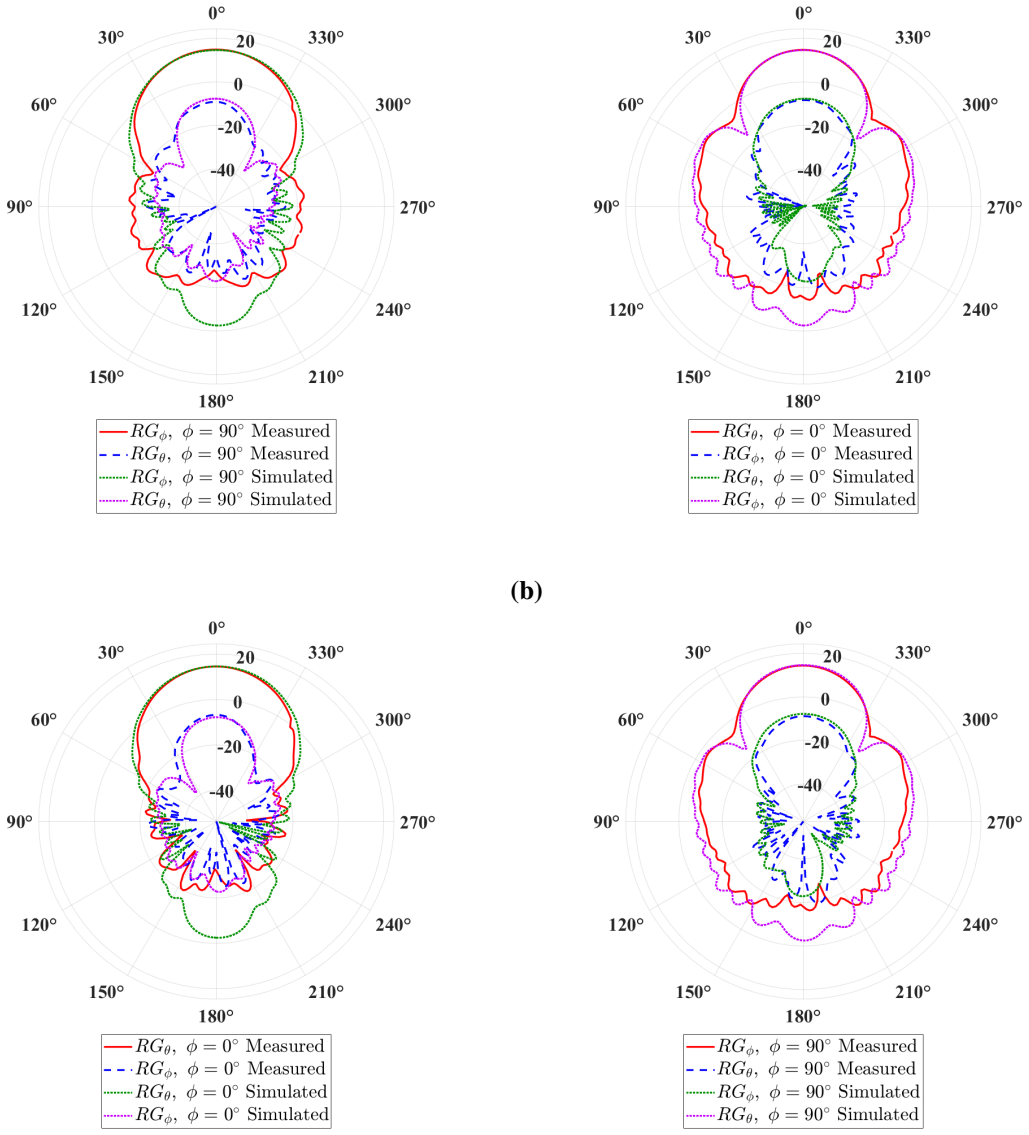

(a) **(b)**

(c) **(d)**

Figure 6.39: Measured radiation patterns for Prototype IV with conductive epoxy compared to simulated at 3.68 GHz with the (a) x-polarized vertically oriented, (b) x-polarized horizontally oriented, (c) y-polarized vertically oriented, and (d) y-polarized horizontally oriented

6.8 Conclusion

In this chapter, additive manufacturing and copper plating of a cavity filter and a horn antenna were thoroughly investigated. Four prototypes were fabricated and measured. A final successful filter prototype was fabricated and measured in-house. There is some reduction in gain at the lower end of the filtering band due to cross-polarization coupling from fabrication limitations. However, the prototype's filtering horn performance largely meets the specifications set during filter design, and the horn radiation pattern matches that of the simulated conical filtering horn antenna at the center frequency.

Chapter 7

Conclusions and Future Work

7.1 Conclusion

The goal of this thesis was to design a filtering horn antenna with increased sensitivity through the implementation of a direct cascaded filtering horn architecture with spatial and frequency filtering. Two bandpass cavity resonator filters, a third-order and a fifth-order, were synthesized using traditional cavity resonator design theory [36]. A conical horn, a corrugated conical horn, and a pyramidal horn were then designed. The goal was to create a horn that implements a method to reduce sidelobe levels, thereby creating a spatial filter by reducing power transmitted outside the main beam. This was accomplished by applying circumferential corrugations to a conical horn antenna. A conical horn antenna was designed to provide a direct comparison with the corrugated horn antenna. Then, a pyramidal horn was designed to provide a dual-polarized antenna to further validate the proposed design method. A design method was proposed to define and extract the Q_{ext} of a dual-polarized 3D horn antenna using group delay for improved matching to the filter, reducing the tuning necessary after the cascade. The design method was applied to match the conical, corrugated, and pyramidal horn antennas to the third-order filter, validating the matching method using horn antennas with different complex load impedances acting on the filter. To validate the design method using different cavity resonator filters, the matching method was applied to

match the conical horn to the fifth-order filter. The conical horn structure cascaded with the third-order cavity resonator filter was fabricated and measured in-house. The results of these measurements are consistent with the simulated results.

7.2 Scientific Contributions

A novel design method is introduced for matching dual-polarized 3D horn antennas to cavity resonator filters. By defining a method for extracting the Q_{ext} of a horn antenna, the horn antenna can be matched to the Q_{ext} needed for the filter. This significantly reduces the tuning necessary when directly cascading horn antennas with cavity resonator filters.

7.3 Future Work

The matching method proposed could be improved by deriving a better method for de-embedding the effects of the coaxial probe feed from the Q_{ext} extraction of the iris-fed horn. There has been some work done for extracting this value for weakly coupled feed structures [51]. However, the work that has been done for de-embedding this value for strongly coupled structures circumvents the calculation of Q_{ext} completely [52]. If a method for de-embedding the Q_{ext} of a strongly coupled coaxial probe is created, the extracted Q_{ext} of the horn will be more accurate, and the coaxial probe excitation will not need to be designed as carefully. The matching method could also be improved, especially for higher-order cavity filters, by defining a method to extract the loaded Q_{ext} from the filter to then match the horn. Another way to improve the matching method would be to account for the frequency loading of the iris-coupled horn antenna. The authors of [33] demonstrated this concept by representing the slot antenna as a K-inverter with a transmission line on either side, allowing for the length of cavity compensation for the final cavity to be calculated. Adapting this process to calculate the cavity-size compensation needed due to the iris-coupled horn

antenna would reduce some of the mismatch between the horn and the filter caused by the horn loading the filter.

References

[1] "3.5 GHz Band Overview." Federal Communications Commission, 16 Dec. 2015, www.fcc.gov/wireless/bureau-divisions/mobility-division/35-ghz-band/35-ghz-band-overview.

[2] W. I. Forum, "Requirements for commercial operation in the u.s. 3550-3700 mhz citizens broadband radio service band," Tech. Rep., 2024.

[3] K. Chowdhury, R. Debrashi, and J. Ruyle, "Collaborative research: swift: medusa: mid-band environmental sensing capability for detecting incumbents during spectrum sharing," proposal submitted to National Science Foundation (NSF).

[4] M. I. Skolnik, *Introduction to Radar Systems*. McGraw Hill Education (India), 2001.

[5] Y. Yusuf and X. Gong, "Integrated filter/antennas with high efficiency and increased bandwidth," in *WAMICON 2011 Conference Proceedings*. IEEE, 2011, pp. 1–4.

[6] J. Li, S. Wu, Y. Li, X. Chen, S. Yan, and X. Y. Zhang, "SLA printed dual-band conical-beam filtering antenna," *IEEE Antennas and Wireless Propagation Letters*, vol. 22, no. 10, pp. 2462–2466, 2023.

[7] B. Froppier, Y. Mahe, E. M. Cruz, and S. Toutain, "Integration of a filtering function in an electromagnetic horn," in *2003 33rd European Microwave Conference*. IEEE, 2003, pp. 939–942.

[8] S. C. Mejillones, M. Oldoni, S. Moscato, M. D'Amico, and G. G. Gentili, "Circularly polarized coaxial horn filtenna for electromagnetic interference mitigation," *IEEE Transactions on Antennas and Propagation*, vol. 71, no. 12, pp. 9487–9496, 2023.

[9] A. Alves, L. da Silva, E. Boas, D. Spadoti, and A. Cerquira S., "Mechanically tunable horn filtenna for mm-waves," in *2019 13th European Conference on Antennas and Propagation (EuCAP)*. IEEE, 2019, pp. 1–4.

[10] K. Mohan Patnaik, G. Basavarajappa, and H. Sigmarsson, "An innovative design methodology of a novel multifunctional all-pole filtering horn antenna," *IEEE Microwave and Wireless Technology Letters*, vol. 35, no. 1, pp. 35–38, 2025.

[11] M. Kumar and G. Basavarajappa, "A multi-functional circularly polarized all pole filtering conical horn antenna," in *2025 IEEE/MTT-S International Microwave Symposium - IMS 2025*. IEEE, 2025, pp. 525–527.

[12] I. Suryarajitha, R. Jawale, G. Basavarajappa, H. H. Sigmarsson, R. K. Panigrahi, and M. Kartikeyan, "An innovative H-plane filtering horn antenna in substrate-integrated waveguide technology," *IEEE Transactions on Components, Packaging and Manufacturing Technology*, vol. 15, no. 5, pp. 1072–1080, 2025.

[13] J. Bandler, R. Biernacki, S. H. Chen, P. Grobelny, and R. Hemmers, "Space mapping technique for electromagnetic optimization," *IEEE Transactions on Microwave Theory and Techniques*, vol. 42, no. 12, pp. 2536–2544, 1994.

[14] F. Bilotti, L. Di Palma, D. Ramaccia, and A. Toscano, "Self-filtering low-noise horn antenna for satellite applications," *IEEE Antennas and Wireless Propagation Letters*, vol. 11, pp. 354–357, 2012.

[15] M. Barbuto, F. Trotta, F. Bilotti, and A. Toscano, "Horn antennas with integrated notch filters," *IEEE Transactions on Antennas and Propagation*, vol. 63, no. 2, pp. 781–785, 2015.

[16] J. W. Shehan and R. S. Adams, "X-band horn antenna with integrated tunable notch filter," in *2015 IEEE International Symposium on Antennas and Propagation USNC/URSI National Radio Science Meeting*. IEEE, 2015, pp. 2213–2214.

[17] M. Barbuto, F. Trotta, F. Bilotti, and A. Toscano, "A combined bandpass filter and polarization transformer for horn antennas," *IEEE Antennas and Wireless Propagation Letters*, vol. 12, pp. 1065–1068, 2013.

[18] G. Q. Luo, W. Hong, Z.-C. Hao, B. Liu, and W. D. Li, "Theory and experiment of novel frequency selective surface based on substrate integrated waveguide technology," *IEEE Transactions on Antennas and Propagation*, vol. 53, no. 12, pp. 4035–4043, 2005.

[19] Z. Sharipov, F. Gunes, A. S. Turk, M. A. Belen, P. Mahouti, and S. Demirel, "Microstrip frequency selective surface for use in horn filtenna," in *2016 IEEE Radar Methods and Systems Workshop (RMSW)*. IEEE, 2016, pp. 107–109.

[20] L. Zhou, H. Jin, W. Wang, Y. Qian, Z. Liao, and G. Luo, "An integrated millimeter wave filtering horn antenna," in *2021 International Conference on Microwave and Millimeter Wave Technology (ICMMT)*. IEEE, 2021, pp. 1–3.

[21] H. Oraizi, M. Hamedani, D. Zarifi, and A. Amini, "Design of filter-horn antenna based on groove gap waveguide technology for V-band application," in *12th European Conference on Antennas and Propagation (EuCAP 2018)*. IET, 2018, pp. 1–4.

[22] M. Hamedani, H. Oraizi, A. Amini, D. Zarifi, and A. U. Zaman, "Planar H-plane horn antenna based on groove gap waveguide technology," *IEEE Antennas and Wireless Propagation Letters*, vol. 19, no. 2, pp. 302–306, 2019.

[23] T. Xiu, Y. Yao, Z. Liu, B. Wang, and J. Yu, "A V-band miniaturized circularly polarized filtering feed horn for reflector antenna," in *2022 Cross Strait Radio Science & Wireless Technology Conference (CSRSWTC)*. IEEE, 2022, pp. 1–3.

[24] Ji-Qi and Y.-D. Kong, "A low sidelobes miniaturized SIW filtering horn antenna loaded with slow-wave metal posts," in *2023 IEEE 11th Asia-Pacific Conference on Antennas and Propagation (APCAP)*. IEEE, 2023, pp. 1–2.

[25] D. Zhao, F. Lin, Z. Zhai, H. Sun, and X. Y. Zhang, "Design of nonreciprocal filtering antenna using spatio-temporal modulated SIW resonators," *IEEE Transactions on Microwave Theory and Techniques*, vol. 71, no. 10, pp. 4505–4518, 2023.

[26] H. Zhang, W. Wang, H. Jin, and G. Q. Luo, "High-gain horn antenna with bandpass filter-like response based on filtering RGW-to-SIW transition," in *2024 IEEE 12th Asia-Pacific Conference on Antennas and Propagation (APCAP)*. IEEE, 2024, pp. 1–2.

[27] W.-G. Yeo, T.-Y. Seo, J. W. Lee, and C. S. Cho, "H-plane sectoral filtering horn antenna in PCB substrates using via fences at millimetre-wave," in *2007 European Microwave Conference*. IEEE, 2007, pp. 818–821.

[28] L. Liu, T.-L. Bai, J.-Y. Deng, D. Sun, Y. Zhang, T. Yong, S.-G. Zhou, and L.-X. Guo, "Substrate integrated waveguide filtering horn antenna facilitated by embedded

via-hole arrays," *IEEE Antennas and Wireless Propagation Letters*, vol. 19, no. 7, pp. 1187–1191, 2020.

[29] M.-M. Yang, L. Zhang, Y. Zhang, H.-W. Yu, and Y.-C. Jiao, "Filtering antenna with quasi-elliptic response based on SIW H-plane horn," *IEEE Antennas and Wireless Propagation Letters*, vol. 20, no. 7, pp. 1302–1306, 2021.

[30] J. Liu, L. Sun, X. Huang, and H. Guo, "Design of K-band SIW H-plane horn antenna with filtering response," in *2022 Cross Strait Radio Science & Wireless Technology Conference (CSRSWTC)*. IEEE, 2022, pp. 1–3.

[31] A. D. Yaghjian and S. R. Best, "Impedance, bandwidth, and Q of antennas," *IEEE Transactions on Antennas and Propagation*, vol. 53, no. 4, pp. 1298–1324, 2005.

[32] A. Bauer, "External quality factor of antennas and their use in filtenna design," Master's thesis, University of Oklahoma, 2022.

[33] Y. Yusuf and X. Gong, "Compact low-loss integration of high-Q 3-D filters with highly efficient antennas," *IEEE transactions on microwave theory and techniques*, vol. 59, no. 4, pp. 857–865, 2011.

[34] R. Agasti, A. Bauer, J. E. Ruyle, and H. H. Sigmarsson, "Frequency-agile SIW-based filtenna using evanescent-mode cavity resonators," *IEEE Antennas and Wireless Propagation Letters*, vol. 22, no. 10, pp. 2600–2604, 2023.

[35] X. He and J. Xu, "A filtering antenna with 3rd-order chebyshev response," in *2016 IEEE MTT-S International Microwave Workshop Series on Advanced Materials and Processes for RF and THz Applications (IMWS-AMP)*. IEEE, 2016, pp. 1–4.

[36] R. J. Cameron, C. M. Kudsia, and R. R. Mansour, *Microwave filters for communication systems: fundamentals, design, and applications*. John Wiley & Sons, 2018.

[37] R. Agasti, "Frequency-agile filtering antennas for S-band and X-band applications," Master's thesis, University of Oklahoma, 2023.

[38] M. Dishal, "Alignment and adjustment of synchronously tuned multiple-resonant-circuit filters," *Proceedings of the IRE*, vol. 39, no. 11, pp. 1448–1455, 1951.

[39] M. Thibodeau, "Theory, design, and fabrication of frequency agile filtennas," Master's thesis, University of Oklahoma, 2020.

[40] S. Saeedi, "Frequency-agile microwave filters for radars with simultaneous transmission and reception," Ph.D. dissertation, University of Oklahoma, 2015.

[41] J.-S. G. Hong and M. J. Lancaster, *Microstrip filters for RF/microwave applications*. John Wiley & Sons, 2004.

[42] J. P. Dunsmore, "The time-domain response of coupled-resonator filters with applications to tuning," Ph.D. dissertation, University of Leeds, 2004.

[43] C. A. Balanis, *Antenna theory: analysis and design*. John wiley & sons, 2016.

[44] R. P. Jadhav, V. J. Dongre, and A. Heddallikar, "Design of X-band conical horn antenna using coaxial feed and improved design technique for bandwidth enhancement," in *2017 International Conference on Computing, Communication, Control and Automation (ICCUBEA)*. IEEE, 2017, pp. 1–6.

[45] A. Heddallikar, V. Ghanvat, K. Sakpal, and R. Pinto, "Optimization of X-band conical horn antenna for level sensing application," in *2019 International Conference on Innovative Trends and Advances in Engineering and Technology (ICITAET)*. IEEE, 2019, pp. 67–72.

[46] B. Thomas, "Design of corrugated conical horns," *IEEE Transactions on Antennas and Propagation*, vol. 26, no. 2, pp. 367–372, 2003.

[47] N. Tevar, P. Mehta, and K. Bhatt, "A review paper on conical corrugated horn antenna," in *2016 International Conference on Wireless Communications, Signal Processing and Networking (WiSPNET)*. IEEE, 2016, pp. 889–892.

[48] R. Lawrie and L. Peters, "Modification of horn antennas for low sidelobe levels," in *1965 Antennas and Propagation Society International Symposium*, vol. 3, 1965, pp. 289–293.

[49] W. L. Stutzman and G. A. Thiele, *Antenna theory and design*. John Wiley & Sons, 2012.

[50] J. E. Ruyle, "Small, dual band, placement insensitive antennas," Ph.D. dissertation, University of Illinois at Urbana-Champaign, 2011.

[51] D. Kajfez and E. J. Hwan, "Q-factor measurement with network analyzer," *IEEE transactions on microwave theory and techniques*, vol. 32, no. 7, pp. 666–670, 2003.

[52] R. Peter and G. Fischerauer, "De-embedding method for strongly coupled cavities," *IEEE Transactions on Microwave Theory and Techniques*, vol. 66, no. 4, pp. 2025–2033, 2018.

[53] H. Lin, Z. Song, X. Wang, and H. Gao, "An improved antenna group delay measurement method using a three-antenna extrapolation technique," *Radioengineering*, vol. 26, no. 3, pp. 675–681, 2017.

[54] A. Newell, S. Gregson, P. Pelland, and D. J. Van Rensburg, "Group delay measurement for satellite payload testing," in *AMTA 39th Annual Meeting & Symposium*, 2017.

[55] X. Wang, X. Huang, and X. Jin, "Novel square/rectangle waveguide septum polarizer," in *2016 IEEE International Conference on Ubiquitous Wireless Broadband (ICUWB)*. IEEE, 2016, pp. 1–4.

[56] A. Bulashenko, S. Piltyay, and I. Demchenko, "Analytical technique for iris polarizers development," in *2020 IEEE International Conference on Problems of Infocommunications. Science and Technology (PIC S&T)*. IEEE, 2020, pp. 593–598.

[57] A. Tribak, A. Mediavilla, J. L. Cano, M. Boussouis, and K. Cepero, "Ultra-broadband low axial ratio corrugated quad-ridge polarizer," in *2009 European Microwave Conference (EuMC)*. IEEE, 2009, pp. 073–076.

[58] L. A. Rud and K. Shpachenko, "Polarizers on sections of square waveguides with inner corner ridges," in *2011 VIII International Conference on Antenna Theory and Techniques*. IEEE, 2011, pp. 338–340.

[59] B. Subbarao and V. Fusco, "Differential phase polarizer used for RCS control," in *IEEE Antennas and Propagation Society Symposium, 2004.*, vol. 4. IEEE, 2004, pp. 4256–4259.

[60] G. L. Ragan, "Microwave transmission circuits," 1948.

[61] V. E. Boria and B. Gimeno, "Waveguide filters for satellites," *IEEE Microwave Magazine*, vol. 8, no. 5, pp. 60–70, 2007.

[62] K. Zhao and D. Psychogiou, "A monolithic vertical integration concept for compact coaxial-resonator-based bandpass filters using additive manufacturing," *IEEE Microwave and Wireless Components Letters*, vol. 31, no. 6, pp. 689–692, 2021.

[63] B. Liu, X. Gong, and W. Chappell, "Layer-by-layer polymer stereolithography fabrication for three-dimensional RF components," in *2004 IEEE MTT-S International Microwave Symposium Digest*, vol. 2, 2004, pp. 481–484 Vol.2.

[64] T. Gerges, A. Marie, T. Wickramasinghe, P. Lombard, M. Levêque, S. Lips, V. Sartre, B. Allard, and M. Cabrera, "Investigation of 3D printed polymer-based heat dissipator for GaN transistors," in *2021 23rd European Conference on Power Electronics and Applications (EPE'21 ECCE Europe)*. IEEE, 2021, pp. P–1.

[65] Y. Zhang, J. Xu, F. Zhang, X. He, X. Li, Y. Sun, and S. Xu, "A 3-D printed Ka-band twisted waveguide filter with filtering and polarization rotation," in *2019 IEEE International Symposium on Antennas and Propagation and USNC-URSI Radio Science Meeting*, 2019, pp. 1701–1702.

[66] D. M. Pozar, *Microwave engineering*. John wiley & sons, 2011.

[67] Anne Marie Helmenstine , "Table of Electrical Resistivity and Conductivity,"thoughtco.com. https://www.thoughtco.com/table-of-electrical-resistivity-conductivity-608499 (accessed Mar. 12, 2026).